A SPECTROSCOPIC SURVEY OF THE SUPERCLUSTER RCS2319+00

Ashley J. Faloon

Master of Science

Department of Physics

McGill University

Montréal, Québec

October 2008

A thesis submitted to McGill University in partial fulfillment of the requirements of the degree Master of Science

Your file Votre référence
ISBN: 978-0-494-66869-6
Our file Notre référence
ISBN: 978-0-494-66869-6

Acknowledgements

First and foremost I must thank my supervisor, Tracy Webb, whose knowledge and patience combine to offer generous support, encouragement, and invaluable advice to her students.

Many thanks are due to Erica Ellingson for her wealth of information on all things concerning galaxy spectra and her willingness and enthusiasm in sharing it. I am very grateful to David Gilbank for allowing me to use his data and for answering my endless questions. Thanks are due to Sebastien Guillot for graciously translating the abstract of this thesis.

To my friends, both in the physics department and beyond, I offer many thanks for their friendship and support and the ability to make me laugh when I need it most; especially Allison Noble, my desk buddy and anchor in an office full of men.

Finally, I would like to thank my family, for their endless love, support and encouragement in all facets of my life. I owe them more than I can ever repay.

Abstract

This thesis presents the results of a spectroscopic survey of the RCS2319+00 supercluster field using the VIMOS instrument on the 8-meter Very Large Telescope. This system is a rare and massive high-redshift structure, comprising at least three galaxy clusters at $z = 0.9$, separated by less than 3 Mpc, and is one of the few examples of the progenitors of present-day massive galaxy clusters.

We measure 638 new redshifts from a sample of 1134 target sources, 49 of which are consistent with the supercluster redshift. Redshifts are also obtained for 24 radio galaxies within the field, with 6 of these identified as cluster members. We combine the VIMOS redshift catalogue with the data analyzed by Gilbank et al. (2008) from the IMACS spectrograph on the 6-meter Magellan telescope for a total of 1051 redshifts over an area of $\sim 30 \times 30$ square arcminutes, with 94 spectroscopically confirmed supercluster members. From this combined data set the mean spectroscopic redshifts of the three galaxy clusters were refined and found to be $z_{spec} = 0.9056$, 0.9041, and 0.9047 for clusters A, B, and C respectively. A new velocity dispersion of $\sigma_\nu = (1300 \pm 410)$ km s^{-1} was calculated for the largest component cluster, A, and was used to estimate a new cluster membership redshift range of $0.8857 \leq z \leq 0.9239$.

These data will facilitate further scientific study of RCS2319+00 and will shed light on the evolution of massive clusters, hierarchical structure formation, and galaxy evolution. In combination with other spectroscopy this data will allow: the full extent of the supercluster and its substructure in redshift space to be traced; a determination of the dynamical masses of the individual sub-clusters; and a study of the galaxy population within the structure, in particular the star-forming galaxies and active galactic nuclei as traced by radio and infrared emission.

Abrégé

Ce mémoire présente les résultats dune étude spectroscopique du super-amas RCS2319, faîte en utilisant linstrument VIMOS au télescope de 8 mètres du VLT. Ce système très rare est une structure massive à large décalage vers le rouge (redshift z). Il comprends au moins trois amas de galaxie à $z = 0.9$, séparé par moins de 3 Mpc. Finalement, il est lun des rares exemples danctre dactuel amas de galaxie massifs.

Nous avons mesuré 638 nouvelles valeurs de redshift dans un échantillon de 1134 sources ciblées, dont 49 se sont révéles être compatible avec le redshift du super-amas. Nous avons également obtenus les redshifts de 24 galaxies radio dans le champ et 6 ont été identifiées comme appartenant au super-amas. Nous avons combiné le catalogue des redshift de VIMOS avec les données analysées par Gilbank et al. (2009) à partir du spectrographe IMACS sur le télescope Magellan de 6 mètres. Un total de 1051 sources sur une aire de $\sim 30 \times 30$ minutes darc sont concernées, et 94 dentre elles ont été confirmées par spectroscopie comme étant membres du super-amas. De cette combinaison de lensemble des données, nous en déduisons le redshift spectroscopique moyen des trois amas de galaxie: $z_{spec} = 0.9056$, 0.9041, et 0.9047 pour les amas A, B, et C, respectivement. De plus, une nouvelle valeur de dispersion de vitesse, $\sigma_{nu} = 1300 \pm 410$ km s^{-1} a été calculépour lamas le plus large des trois, amas A, et cette valeur a par ailleurs été utilisée pour estimer le redshift dun nouveau membre du cluster, avec z dans lintervalle $0.8857 < z < 0.9239$.

Ces données vont faciliter létude scientifique approfondie de RCS2319+00 et vont également permettre déclaircir les connaissances sur lévolution des amas massifs, sur la formation hiérarchique des structures, et sur lévolution des galaxies. La spectroscopie va permettre de tracer lintégralité des redshifts du super-amas et de sa

sous-structure. La mesure de la masse dynamique des sous-amas et une étude de la population des galaxies dans la super-structure, en particulier les galaxies formatrices détoiles et les noyaux actifs de galaxie tel que vue dans linfrarouge ou les ondes radio, vont également étre permises par la spectroscopie.

Contents

List of Figures

List of Tables

Chapter 1

Introduction

Exploring the high redshift universe has become an increasingly attainable venture over the last several years as technology on both ground and space based telescopes has advanced to allow us to probe deeper into the early universe. This ability to look far back into the formation era of the Universe has not come without its problems. One main issue is the redshift identification of large samples of galaxies. Spectroscopy of individual sources remains the optimum strategy for determining the distance at which these objects lie in the Universe, which is necessary for the study of the properties of high redshift populations.

The topic of this thesis centers on a spectroscopic survey of the supercluster structure, RCS2319+00, discovered in the first Red-sequence Cluster Survey (Gladders and Yee, 2005). This rare, massive supercluster, which lies in the high redshift universe at $z \sim 0.9$, presents a unique opportunity to study the growth and evolution of superclusters in the context of hierarchical structure formation models, and the evolution of the galaxies with which they are populated. However, this can not be done without adequate spectroscopic coverage of the supercluster field to confirm galaxies within the structure. Here we present new data from the wide–field Visible Multi–Object Spectrograph (VIMOS) on the 8 meter Very Large Telescope (VLT), which has been analyzed and combined with previous spectroscopic data on this field from Gilbank et al. (2008).

The introduction of this thesis provides a brief overview of the theory behind hierarchical structure formation, clusters and superclusters in the universe. Also contained is an outline of the cluster survey method used to find the RCS2319+00

superstructure and a look at the importance of studying systems at $z \sim 1$ and obtaining spectroscopy for their members. Chapter 2 delves into the known details of the RCS2319+00 supercluster and two of its member populations: radio and submillimeter galaxies. The data set and reduction methods used are explained in Chapter 3 while the analysis and results are described in Chapter 4 and summarized in the final chapter.

All values adopted in regards to the RCS2319+00 superstructure assume a cosmology of $\Omega_m = 0.3$, $\Omega_\Lambda = 0.7$, and $H_o = 70$ km s^{-1}Mpc^{-1}.

1.1 Hierarchical Structure Formation in the Universe

Observations, such as those from the Sloan Digital Sky Survey (SDSS), show that on scales of ~ 100 Mpc and less the Universe is an inhomogeneous entity populated by large superstructures separated by vast voids (Stoughton et al., 2002). These immense superstructures contain clusters of galaxies gravitationally bound together. The galaxy clusters themselves are bound systems containing individual galaxies. The order in which these structures formed is a question of cosmology and the nature of the dark matter in the universe. If the majority of the dark matter is hot than one would expect to find top-down structure formation wherein the largest structures would form first and fragment into the smaller clusters and individual galaxies. However, in a universe dominated by cold dark matter, one would instead expect a hierarchical structure formation scheme, with small galaxies forming first, followed by clusters and superclusters. Observational data suggests that superclusters are only just collapsing at present while individual galaxies are seen out to redshifts of $z \sim 6$, supporting a cold dark matter model of cosmological formation (Ryden, 2003).

Hierarchical structure formation begins when small density perturbations in the early universe, known to exist at the surface of last scattering through observation of

the cosmic microwave background (CMB), become sufficiently dense to gravitationally collapse, forming dark matter haloes (Ryden, 2003). If these dark matter haloes are dense enough, gas can cool and condense to form galaxies and stars (Kauffmann et al., 1999). The amplitude of these small density fluctuations increases through gravity, merging into first groups, then clusters of galaxies. The dense clusters continue to accrete matter from underdense regions along overdense filaments, eventually becoming virialized systems. Observations have shown that many clusters are still in the formation stage with significant substructure present (Jones et al., 2008). These galaxy clusters are themselves gravitationally bound in supercluster structures, the largest observed gravitationally bound structures in the universe.

From both observations (e.g. Jones et al., 2007) and theoretical modeling (e.g. Wray et al., 2006) of superclusters, it is apparent that these structures are still undergoing gravitational collapse. Wray et al. (2006) used the parallel dark matter simulation code of Bode and Ostriker (2003) to study the morphology and evolution of superclusters with time. They concluded that the density of superclusters in the universe decreases with redshift, with few rich superclusters found at high redshift. This result is a logical consequence of hierarchical structure formation since at lower redshift more galaxy clusters have had time to form and evolve, increasing the density of clusters and therefore the prevalence of superclusters.

1.2 Galaxy Clusters and Superclusters

Galaxy clusters were first observed as far back as 1781 by Charles Messier, who saw an accumulation of 'nebulae' near Virgo. In the 1920s Edwin Hubble used Cepheid variables to prove that these 'spiral nebula' were not contained within our galaxy and noted that they were not distributed randomly but seemed to be grouped together (Peacock, 1999). Dark matter was first postulated in 1933 by Fritz Zwicky when he

used the virial theorem to show that the the luminous mass of the Coma cluster was not sufficient to explain the velocities of the galaxies in the cluster (Zwicky, 1933).

In the 1950s, Fritz Zwicky and George Abell each embarked on separate surveys of galaxy clusters using the Palomar Sky Survey photographic plates (Zwicky et al., 1961-1968; Abell, 1958). Though they both used overdensities of galaxies to identify clusters, their methods were quite different. In the end, though Zwicky's catalogue was the larger of the two with 9700 identified galaxy clusters, Abell's catalogue of the 2712 richest clusters proved more significant and was later increased to include clusters seen from the Southern Hemisphere for a total of 4073 rich clusters (Abell et al., 1989; Bahcall, 1988; Peacock, 1999).

Abell defined a cluster as having $\gtrsim 50$ members, above background counts, within a radius of 1.5 h^{-1} Mpc of the cluster center and having magnitudes ranging from the third brightest galaxy, m_3, to $m_3 + 2$. The richness of each cluster was defined by the number of galaxies contained within the Abell radius. Using the apparent magnitude of the tenth brightest galaxy in the cluster, Abell estimated the redshift and distance to the clusters. His catalogue of rich clusters is, for the most part, complete to $z \sim 0.1$ and contains clusters out to $z \sim 0.2$ (Abell, 1958; Bahcall, 1988; Peacock, 1999).

Current and recent surveys looking for galaxy clusters have included: optical and IR surveys which search for overdensities in galaxy populations, radio surveys that look for diffuse groups of radio sources, X-ray surveys searching for emission from the hot gas of the intracluster medium (ICM) and bright active galactic nuclei sources (AGN), and microwave surveys looking for the Sunyaev-Zeldovich, effect wherein galaxy cluster electrons cause inverse Compton scattering of CMB photons and appears as a distortion of the CMB spectrum (Voit, 2005).

It is now known that galaxy clusters comprise $\sim$ 5% of their mass in galaxies, $\sim$ 10% in the hot gas of the ICM, and $\sim$ 85% in dark matter. The typical radius

of a galaxy cluster is $\sim 3-4\ h^{-1}$ Mpc with core radii of $\sim 250\ h^{-1}$ kpc however clusters on scales of $\sim 50\ h^{-1}$ Mpc have been found. The average mass of galaxy clusters has been shown to be between $10^{14}-10^{15}\ h^{-1}\ M_{\odot}$ with velocity distributions of $\sim 800-1000$ km s^{-1} . It is also known that there exists a morphological segregation in galaxy clusters, with early-type elliptical galaxies occupying the core of clusters while spiral galaxies are found farther out towards the edges of clusters (Binney and Tremaine, 1994).

Galaxy clusters are excellent laboratories in which to study the effects of the environment on galaxy evolution. Clusters are dynamically younger than the galaxies which occupy them and many are still in the process of collapsing (Binney and Tremaine, 1994). Many mechanisms exist within galaxy clusters that could either enhance or turn off star formation and AGN activity in cluster galaxies. Interactions between infalling galaxies that give rise to galaxy mergers (e.g., Dubinski 1998) and tidal effects (e.g., Bekki & Couch 2003) that can cause star formation or AGN activity. On the other hand, once within the sphere of influence of the cluster there are many mechanisms, such as ram pressure stripping and halo starvation, which may be responsible for turning off star formation and AGN fueling. These mechanisms are not yet well understood.

Clusters of galaxy clusters, or supercluster structures, are the largest gravitationally bound structures in the universe. Their size can range greatly from a few times the size of a typical galaxy cluster to $\sim 100\ h^{-1}$ Mpc scales. Their enormous size has made finding these superclusters problematic since typical survey sizes are not large enough to recognize these immense and rare structures. At low redshift, the abundance of known clusters from catalogues have been used to identify superclusters. At higher redshifts, such catalogues are not complete, making the identification of superclusters much more difficult (Wray et al., 2006).

1.3 The Red-sequence Cluster Survey

The Red-sequence Cluster Survey (RCS1) is an optically selected galaxy cluster survey which catalogued $\sim$ 1000 galaxy clusters over a redshift range of $0.35 < z < 0.95$ covering an area of $\sim$ 92 degrees^2 on the sky (Gladders and Yee, 2005). The RCS cluster finding method, developed by Gladders and Yee (2000), uses R_c and z' band optical and near-infrared imaging data from the MOSAIC–II camera on the CTIO (Cerro Tololo Inter–American Observatory) 4 meter telescope and the 12 K camera on the CFHT (Canada France Hawaii Telescope) to search for galaxy clusters.

The cluster finding algorithm was developed based on observational evidence that all rich clusters contain early-type galaxies which show a defined colour-magnitude relation, dubbed the red-sequence (Gladders and Yee, 2000). Sandage, Bingelli and Tamman (1985) found that the cluster luminosity function is dominated at the bright end by elliptical galaxies. In their study of this colour-magnitude relation in the Coma and Virgo clusters, Bower, Lucey and Ellis (1992) found that the rms scatter on this relation is decidedly small, having a value of 0.05 mag with observational errors making up $\sim$ 0.03 mag of this scatter.

Figure 1.1 shows an example of the red-sequence relation for the Abell 2390 cluster at $z = 0.231$ found using Hubble Space Telescope data in only two filters. This data was used by Gladders and Yee (2000) to demonstrate the effectiveness of the red-sequence cluster finding method. At any given redshift only two well chosen filters are needed to identify cluster ellipticals, which appear redder than normal galaxies at low redshift. The method uses slices in the colour-magnitude plane to search for spatial over-densities of red-sequence galaxies indicative of galaxy clusters by simultaneously looking for colour, magnitude and projected angular position overdensities (Gladders and Yee, 2000).

The R_c and z' band optical and near-infrared filters used for the survey were

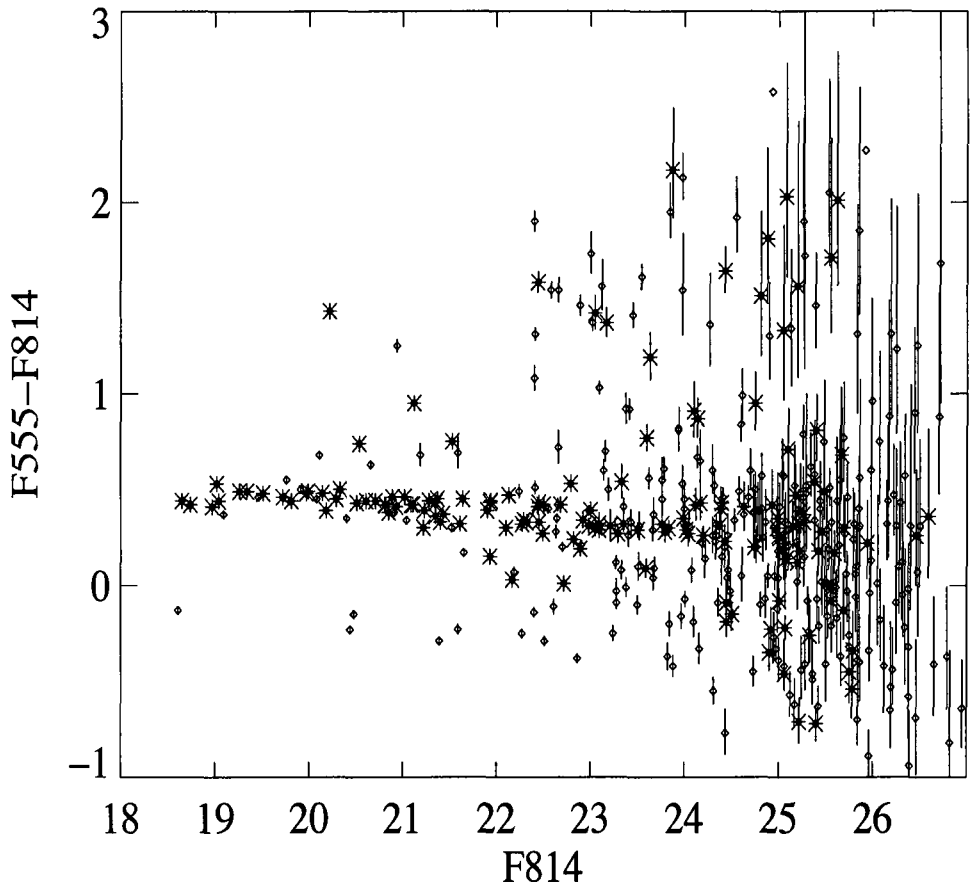

Figure 1.1: Example of the red-sequence galaxy colour-magnitude relation for Abell 2390 at $z = 0.23$ from two filter HST imaging. The asterisks indicate early type galaxies based on morphological selection. The presence of an excess of red-sequence galaxies, seen as the line of early-type galaxies, indicates the presence of a galaxy cluster. Taken from Gladders and Yee (2000).

chosen to ensure that they encompass the 4000 Å Balmer break for the desired survey redshift range of $0.35 < z < 0.95$ (Gladders and Yee, 2000). The 4000 Å break is an indicator of the age of galaxies, with old, metal rich galaxies showing a more pronounced Balmer break than young galaxies which contain hot stars (Kauffmann et al., 2003). The break is defined as the ratio of the average flux density in the 4050–4250 Å wavelength range to that in the 3750–3950 Å range (Poggianti and Barbaro, 1997).

Using the red-sequence of early-type elliptical galaxies is justified further by the

likelihood that the stellar populations of these elliptical cluster galaxies are the oldest and most homogenous in the universe and as such will appear as red or redder on the colour-magnitude diagram than other galaxies at the given redshift due to the pronounced Balmer break (Gladders and Yee, 2000). In this way, the RCS survey uses a simple colour-cut in two filters to search for galaxy clusters with little to no contamination from foreground sources.

Compared to most other galaxy cluster surveys, which require complicated algorithms with numerous parameters including specific survey flux limits and cluster redshifts, the RCS cluster finding method is a reliable method for finding clusters at a comparatively low overhead in telescope time and algorithm integration. By using consecutive cuts in the colour-magnitude plane to search for clusters, the most common selection effect of other optical cluster surveys, that of projection contamination, is greatly reduced (Yee et al., 2007).

Using the red-sequence method not only identifies galaxy clusters, but the slope of red-sequence line gives an estimate of the cluster redshift accurate to $\sim 10\%$ using only the survey data (Gladders and Yee, 2000). This is done using the known spectral energy distribution for elliptical galaxies, which show a very strong 4000 Å Balmer break. The high accuracy of the cluster redshift estimation is due to the fact that it is based on all galaxies found to occupy the given red-sequence simultaneously (Gladders and Yee, 2000). Figure 1.2 is an example of a simulated colour-magnitude diagram for various redshifts and galaxy types, showing that at a given redshift, the elliptical galaxies are consistently redder than all other galaxy types, as discussed above.

From the number of galaxies identified in the red-sequence of a cluster, a cluster richness parameter, B_{gcR}, is computed and used as a representative for the mass of the cluster. This richness is calculated from the count of excess red-sequence galaxies

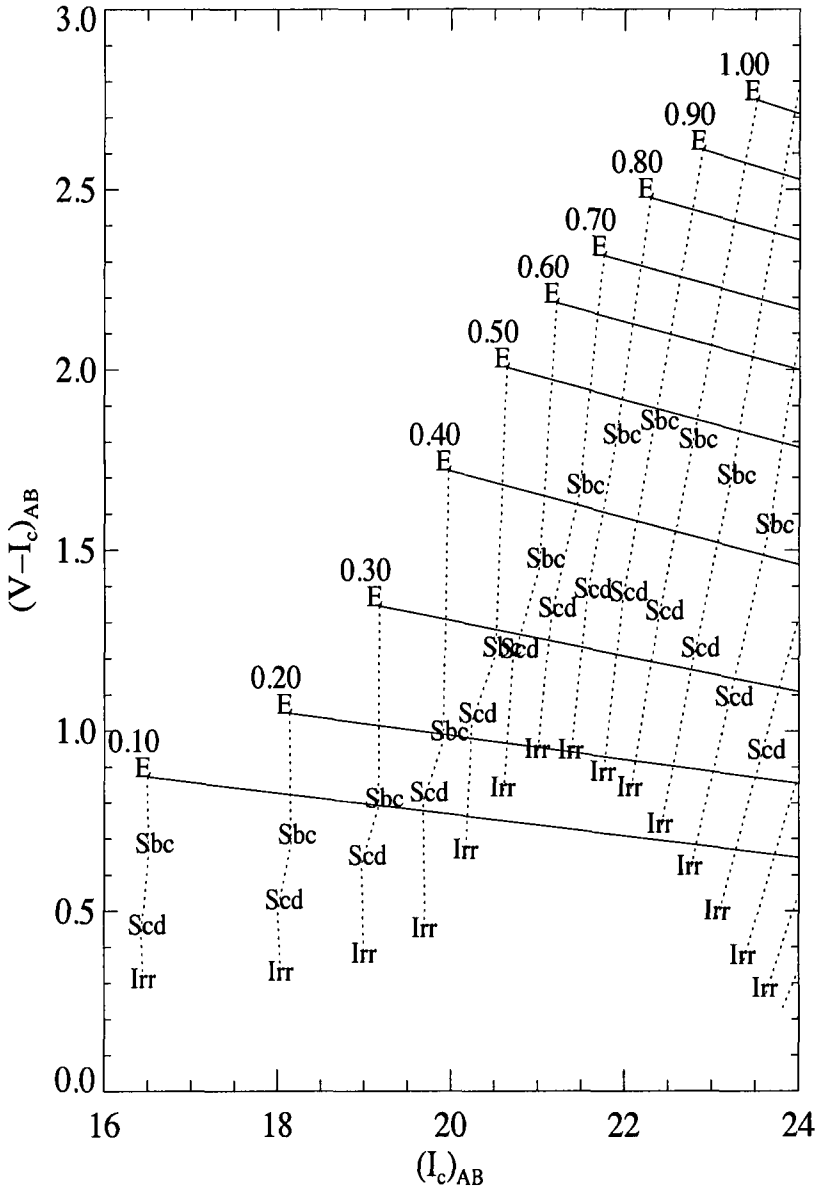

Figure 1.2: Simulation of the slope of the red-sequence relation for different redshifts by Gladders and Yee (2000). The dotted lines link different galaxy types with each of the simulated red-sequence slopes.

in an area $0.5h_{50}^{-1}$ Mpc around the cluster center. The use of only red galaxies for the measurement is done to increase the reliability of the richness estimate at high redshifts ($z > 0.5$). The evolution of blue galaxies in clusters is not well known and including them in the richness measurement would reduce the dependability of the

calculation (Gladders and Yee, 2005).

The importance of the RCS survey can be seen in its ability to constrain cosmological parameters. It represents the first large, homogenous galaxy cluster sample with broad redshift and mass range used to measure the cosmological parameters Ω_M and σ_8 directly and simultaneously (Gladders et al., 2007). Using the cluster abundance at different redshifts ($dN/dz(z)$) and fitting it to an expected mass limit ($M_{lim}(z)$), Yee et al. (2007) were able to estimate the matter density of the universe and the normalized power spectrum to be $\Omega_M = 0.31^{+0.11}_{-0.10}$ and $\sigma_8 = 0.67^{+0.18}_{-0.13}$, consistent with the WMAP 3 year data (Spergel et al., 2007). A follow-up survey covering an area of $\sim$ 1000 deg.^{2}, named RCS2, is currently underway. The expectation is that several $\times$ 10^4 galaxy clusters will be found, allowing for improvement on the current estimates for Ω_M and σ_8 and enabling constraints to be placed on the dark energy equation of state (see Section 1.4) (Yee et al., 2007).

The capacity for ancillary science on the RCS survey sample is vast due to the large, consistent selection of galaxy clusters over a broad redshift range ($0.35 < z < 0.95$) based on a well understood and systematic cluster finding technique. Many studies are underway on the RCS cluster catalogue as a whole, on subsets of the cluster sample, and on individual, interesting objects, such as the RCS2319+00 supercluster field. As mentioned above, Gladders et al. (2007) have used the RCS cluster database to constrain cosmological parameters. Hicks et al. (2008) used a subset of thirteen RCS clusters to study the X-ray properties of galaxy clusters in a redshift range of $0.6 < z < 1.1$. A study of the characteristics and prevalence of strong lensing clusters found in the RCS sample was completed by Gladders er al. (2003). Spectroscopic surveys (e.g. Gilbank et al., 2007) of RCS galaxy clusters are underway to help constrain cluster membership for studies of cluster populations and evolution as well as to test the reliability of the red-sequence identified cluster redshift.

A spectroscopic survey of the RCS identified supercluster structure RCS2319+00 at $z = 0.9$ is the motivation for this thesis. Section 2.1 describes the importance of this unique structure and why it has been chosen for extensive study.

1.4 The Importance of $z \sim 1$

When studying cluster evolution, it is important to push observations to higher redshift in an effort to approach the epoch of cluster formation, thought to occur at $z \sim 2 - 5$ (Yee et al., 2007). At $z \sim 1$, we are nearing this important cluster evolutionary stage. A large number of clusters at $z \sim 1$ would also allow for the measurement of a reliable cluster mass function at this redshift and enable constraints to be placed on the important cosmological parameter ω, the equation of state (Yee et al., 2007).

Observations of galaxy clusters at $z > 0.8$ are still relatively small in number as their discovery is hindered by selection effects. In X-ray surveys, instruments can not probe deep enough over a sufficiently large area of the sky. As mentioned in Section 1.3, most optical cluster surveys suffer from projection contamination from foreground objects, which increases at high redshift (Yee, 2004). The RCS and subsequent RCS2 surveys all but eliminate this projection contamination and have added a considerable number of clusters at $z \sim 1$ to the known sample (Yee et al., 2007).

One major constraint on studying $z \sim 1$ galaxy clusters is that it is very difficult to obtain detailed spectroscopic observations at high redshifts (see Section 1.5). As such, most studies have had to rely on less accurate photometric techniques to delineate between background and foreground objects and cluster galaxies (Yee, 2004).

1.5 The Importance of Spectroscopic Redshift Catalogues

Spectroscopic analysis of galaxy cluster candidates is very important for two main reasons: to obtain accurate redshift values and to study the spectral features of cluster members. Accurate redshift values constrain cluster membership and can be used to obtain velocity dispersions in order to perform dynamical analysis on galaxy clusters to calculate virial masses. If spectral features are strong enough, they can be used to disentangle information on the stellar populations of the cluster galaxies.

The strength of the Balmer break, for instance, can be used to estimate the age of stellar populations in galaxies with old populations displaying a higher Balmer break than young, star forming galaxies. The physical and evolutionary states of the sources can be studied through the strength of the [OII] 3727 Å emission line, which is an indicator of current star formation, and the H_δ 4101 Å absorption line, indicative of recent star formation (Poggianti et al., 1999; Smail et al., 1999). The strength of the [OII] emission is influenced by the abundance and state of the ionized gas and starburst galaxies, with their diffuse regions of ionized gas, have particularly strong [OII] emission lines(Kennicutt, 1998). The strength of the H_δ absorption line, which indicates star formation activity in the last $\sim$ 2 Gyrs, depends on the type of stars formed in the galaxy, with stronger absorption lines when A stars are dominant (Le Borgne et al., 2006).

Most $z \sim 1$ galaxy clusters only have on the order of 10 or so spectroscopically confirmed members (Yee, 2004). Spectroscopic redshifts of high redshift galaxy clusters are difficult to obtain due in part to observational constraints. Longer integration times are needed to acquire the same S/N as lower redshift sources. Also, many prominent emission features such as [H_β] 4861 Å, the oxygen doublet [OIII] at 4959 Å and 5007 Å, and [H_α] 6563 Å are either shifted past the wavelength range of optical spectroscopy or are hard to distinguish from fringe lines present at the red

end of the CCD in many MOS instruments.

To further complicate matters, the frequency of emission–line galaxies in clusters is much lower than in field galaxies (Dressler et al., 1985). This effect was first noticed by Osterbrock (1960) and later confirmed by Gisler (1978). These emission–line galaxies show weak H_β emission compared to the [OII] 3727 Å emission and may not exhibit any [OIII] 4959 Å and 5007 Å emission. Dressler, Thompson and Shectman (1985) found that only 7% of identified cluster galaxies are emission–line galaxies. This may be due to the fact that emission lines are more prevalent in spiral galaxies compared to the early–type galaxies and as such can be used to test theories concerning the morphology of clusters (Balogh et al., 1997). With a high-redshift cluster such as RCS2319+00, this effect coupled with the selection effects mentioned above, namely the difficulty in obtaining adequate S/N, make the task of identifying spectroscopic redshifts an arduous one.

It is important to compile valid catalogues of cluster members in order to better map out the structures in redshift space and within the physical distribution of the cluster, constrain the spectroscopic redshift of galaxy clusters, and estimate the virial mass of clusters from the velocity dispersion. The survey contained in this thesis will add to the existing spectroscopic redshifts which have been determined for a number of optical and X-ray selected candidates in the RCS2319+00 superstructure (see Section 2.1). In particular it adds spectroscopically confirmed cluster members belonging to the important radio population (see Section 2.2). It will aid collaborators in various follow up science investigations being undertaken on this superstructure that are aimed at studying the evolution of star formation and AGN fraction in clusters and understanding the effect of environment on galaxy evolution.

Chapter 2

A Unique Cluster Specimen And Its Constituents

2.1 The RCS2319+00 Superstructure

The research contained herein centers around a follow up spectroscopic study of a very unique superstructure found by the RCS. The RCS2319+00 field is very intriguing in that it contains a supercluster structure of at least three optically selected rich galaxy clusters in close proximity at a redshift of z = 0.90, equivalent to about six billion years after the Big Bang. The spatial separation of each of the component clusters to their nearest neighbour is < 3 Mpc in the plane of the sky. Along the line of sight, the clusters are estimated to have a separation of < 10 Mpc (Gilbank et al., 2008).

All three of the component galaxy clusters, RCS231953+0038.0 (hereafter referred to as cluster A), RCS232002+0033.4 (cluster B), and RCS231948+0030.1 (cluster C) are spectroscopically confirmed to reside at a redshift of $z = 0.9$ (Gilbank et al., 2008). The spectroscopic redshifts were found using data from the IMACS Wide-field multi-object spectrograph on the Baade 6.5 m telescope operating over a wavelength range of 6050 – 8580 Å. The data cover an area with a diameter of 27 arcminutes. 725 slits were placed on a single IMACS mask for a total integration time of 7200 seconds and yielded 302 redshifts and 54 confirmed cluster members. For each cluster center, spectroscopically confirmed galaxies within a 1.5 Mpc radius were used to constrain the spectroscopic redshifts of the cluster. For cluster A, nine higher confidence cluster members were used to measure a velocity distribution of $\sigma = (790 \pm 200)$ km s^{-1}, which corresponds to a virial mass of $3.1^{+3.0}_{-1.8} \times 10^{14}$ M$_\odot$ (Gilbank et al., 2008). Clusters B and C did not have sufficient spectroscopic cluster members to calculate reliable velocity

dispersions and virial masses. With the addition of the work contained herein and current and future spectroscopic surveys of this supercluster field, we hope to better constrain the velocity dispersions and dynamical masses of all three clusters.

The component clusters have also all been shown to display extended X-ray emission as detected by the Chandra Advanced CCD Imaging Spectrometer (ACIS). Figure 2.1 shows the smoothed 0.3–0.7 keV X-ray flux image of the RCS2319+00 supercluster field. Cluster A is at the top of the Figure 2.1, cluster B is in the middle on the left and cluster C is at the bottom on the right.

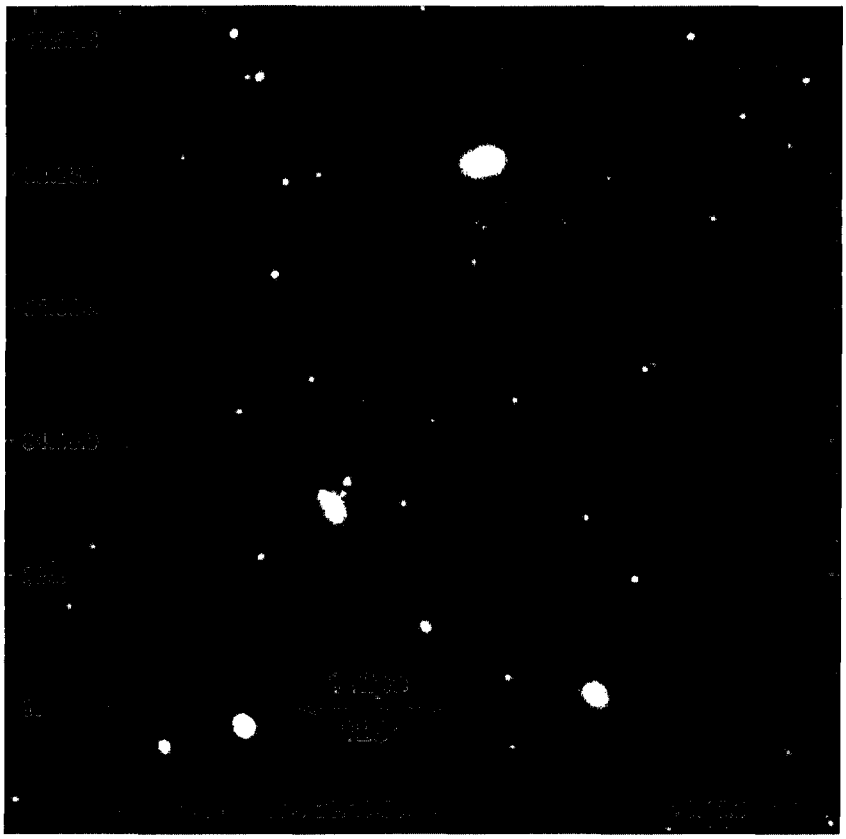

Figure 2.1: Smoothed X-ray flux image of the RCS2319+00 supercluster from Hicks et al. (2008) in the 0.3–7.0 keV band.

Table 2.1 contains the known properties of the three RCS2319+00 component clusters as summarized by Gilbank et al. (2008). The spectroscopic redshift of each component cluster, z_{spec}, is taken from Gilbank et al. (2008) and represents the mean

redshift within a 1.5 Mpc radius of the cluster centers. The optical richness values (B_{gcR}) are taken from the RCS catalogue by Gladders and Yee (2005). From the X-ray observations, X-ray temperatures and bolometric luminosities were measured for a radius wherein the mean X-ray density is 2500 times the critical density, r_{2500}, and X-ray masses were interpolated for the virial radius, r_{200} (Hicks et al., 2008).

Table 2.1: Summary of the RCS2319+00 component clusters from Gilbank et al. (2008).

Cluster	RA	DEC	z_{spec}	B_{gcR} $(h_{50}^{-1}\mathrm{Mpc})^{1.77}$	M_{Xtot} $(10^{14}\ \mathrm{M}_{\odot})$	L_X $(10^{44}\ \mathrm{erg\ s^{-1}})$	T_X (keV)
A	23:19:53	+00:38:00	0.8972	1515 ± 280	$6.4^{+1.0}_{-0.9}$	$7.6^{+0.6}_{-0.4}$	$6.2^{+0.9}_{-0.8}$
B	23:20:02	+00:33:24	0.9024	1150 ± 320	$5.1^{+0.8}_{-0.8}$	$3.6^{+0.6}_{-0.4}$	6.5^{+1}_{-1}
C	23:19:48	+00:30:06	0.9045	580 ± 200	$4.7^{+0.9}_{-1.4}$	$4.2^{+0.5}_{-0.3}$	5.9^{+2}_{-1}

In addition to the spectroscopic confirmation that clusters A, B, and C lie at the same redshift, when the red-sequence significance contours, found by Gladders & Yee (2005), are plotted over the cluster centers, they show that the major axes of each cluster points to its nearest neighbour. This gives further evidence of a gravitational association between the three clusters (Binggeli, 1982).

Cluster A is also known to be a spectacular example of a high redshift gravitational strong lensing cluster. I-band imaging taken with the Baade 6.5 m telescope shows the presence of two gravitational arcs. Bluer imaging of the same region indicates that cluster A is a three arc system (Gladders et al., 2003). Figure 2.2 shows the amazing gravitational arcs around cluster A, the first discovered cluster in the RCS2319+00 field.

There are also five other outlying clusters at the same photometric redshift within the larger RCS2319+00 field that may be gravitationally bound to the superstructure. These clusters have yet to be spectroscopically confirmed as being part of the RCS2319+00 superstructure of coincident clusters in the same region of the sky. The area covered by the spectroscopic data in this thesis does not cover the regions which include these outlying clusters.

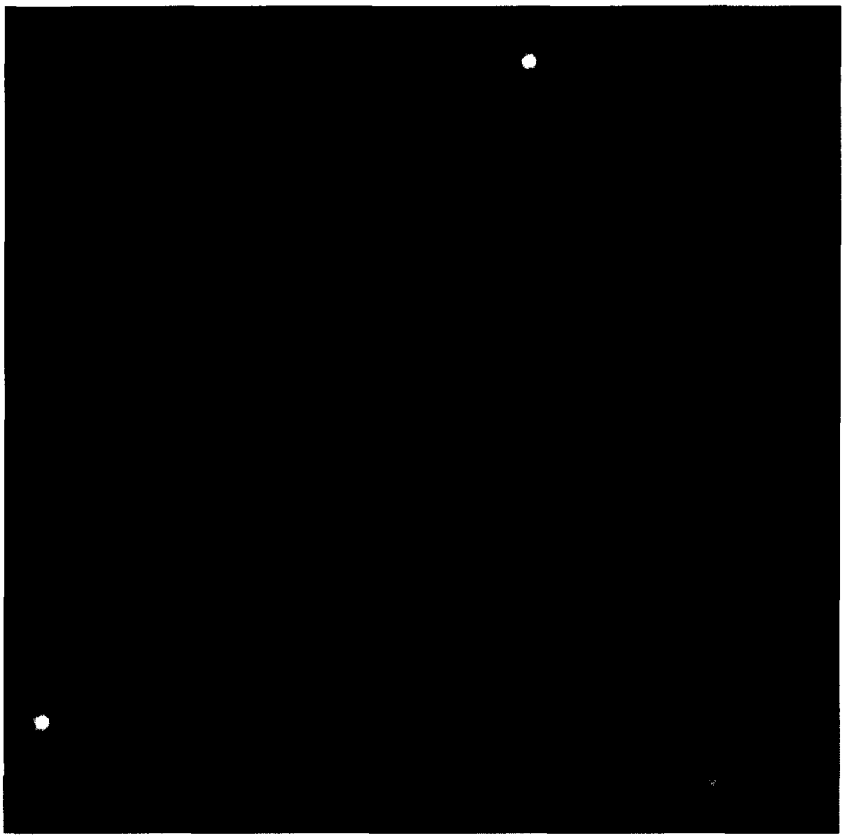

Figure 2.2: Image by Gladders et al. (2003) of the strong gravitational arcs found in the region surrounding cluster A in the RCS2319+00 supercluster field.

To determine the probability of finding such an interesting superstructure in the relatively small survey area of the RCS (~ 92 deg^2), Gilbank et al. (2008) calculated the expected surface density per square degree using the Hubble Volume simulations (Evrard et al., 2002). The Hubble Volume simulations were performed using a value of $\sigma_8 = 0.9$ which has since been updated to $\sigma_8 = 0.76^{+0.049}_{-0.048}$ by the WMAP 3 year data. A reduced σ_8 value reduces the amount of large scale structure in the universe and makes the probability of finding superclusters less probable. For the area enclosed by a one eighth arc of the sky and with the constraint that the separation between the three clusters be > 3 Mpc, the calculated surface density (with $\sigma_8 = 0.9$) is 1.9×10^{-4} RCS2319–like systems per square degree. This translates to $< 2\%$ probability of finding a structure like RCS2319+00. Even when the separation distance is changed

to be the estimated upper limit line of sight distance between the clusters of $\sim$ 10 Mpc, the probability of finding such a structure in a RCS size survey is $< 9\%$, and would be less with the updated value of σ_8 (Gilbank et al., 2008).

In the hierarchical model of the universe (Section 1.1) large structures are formed through the merging of smaller structures due to gravitational effects. It is therefore thought that the three massive component clusters observed in RCS2319+00 are in the process of merging into a larger structure. Gilbank et al. (2008) calculated that by $z \sim 0.5$ the clusters will merge into a system with $M \gtrsim 10^{15}$ $M_{\odot}$, comparable to the most massive known galaxy clusters. The calculation involved the assumptions that the relative velocity of each component cluster is similar to the rest frame line of sight velocity, or $\sim$ 1200 km/s, and that the clusters are not moving apart due to Hubble flow (Gilbank et al., 2008).

This structure represents a unique opportunity to study the possible precursors to the massive galaxy clusters seen in the universe at lower redshifts and later evolutionary periods. Although other superclusters have been found at similar redshifts by Lubin et al. (2000) and Swinbank et al. (2007a), they have lower mass component clusters spread further apart. The Lubin et al. (2000) supercluster contains two members at $z = 0.897$ and $z = 0.924$ separated by $\sim$ 7 Mpc on the sky while the the Swinbank et al. (2007a) superstructure contains five clusters spread over 30 Mpc on the sky at $z = 0.89 \pm 0.01$. It is therefore unlikely that those systems will merge into large clusters at lower redshift (Gilbank et al., 2008).

For this reason a number of follow-up studies are being carried out to better understand the science behind RCS2319+00. An intense spectroscopic follow up, of which this research is an important constituent, is underway to isolate cluster member galaxies and refine the velocity dispersion estimates and dynamical mass computations. X-ray data from the Chandra X-ray telescope, radio data from the Very Large

Array interferometer, submillimeter data from SCUBA (Submillimeter Common User Bolometer Array) on the JCMT, and mid-infrared data from the MIPS (Multiband Photometer for Spitzer) and IRAC (IR Array Camera) on the Spitzer Space Telescope have been or are in the process of being observed on this superstructure.

2.2 The Radio Population

One key goal of this project is to identify cluster radio galaxies in the RCS2319+00 supercluster. A radio luminosity of $\sim 10^{23}\ W\ Hz^{-1}$ acts as a rough dividing feature between the two categories of radio galaxies, with star-forming galaxies on the low luminosity end and AGN occupying the higher luminosity region (Condon, 1992). The radio population represents a form of active galaxy that exhibit large star formation rates and/or contain AGN (actively accreting supermassive black holes). The radio emission in star forming galaxies is due to a combination of thermal bremsstrahlung radiation from electrons accelerated in ionized HII regions and non-thermal synchrotron radiation from relativistic cosmic ray electrons emitted from supernovae remnants (Condon, 1992; Miller and Owen, 2001). This activity may be triggered by interactions with the cluster environment as a group and as individual galaxies fall into the cluster potential during hierarchical structure formation.

In a survey of $z \leq 0.2$ galaxy clusters, Lin and Mohr (2007) found that the fraction of radio galaxies in clusters is 5–10% higher than in the field galaxy population, with most classified as AGN. The fraction of AGN and star forming galaxies in the cluster population as a function of redshift has become an important quest in recent years in order to explore the history of the evolution of these galaxies and the effect of the environment on their life cycle as well as their effect on the cluster environment.

One reason to study the radio population in galaxy clusters is to investigate their importance in solving the cooling flow problem. Observations of the ICM show that it

does not cool sufficiently in the central regions compared to the predicted theoretical cooling flows. Lin and Mohr (2007) estimated that the radio galaxy population may contribute large amounts of energy to the ICM in the central regions of clusters, at a level of ~ 0.13 keV per particle. Powerful AGN also appear to be more concentrated in clusters than other galaxy types and could contribute to feedback heating of the central ICM (Ledlow and Owen, 1995; Lin and Mohr, 2007).

The radio source lists used in this research were compiled from a $\sim 30 \times 30$ arcminute, 1.4 GHz Very Large Array radio map with a 5σ depth of ~ 75 μJy. This depth corresponds to a star formation rate of ~ 50 $M_\odot$ yr^{-1} at $z = 0.9$.

2.3 The Submillimeter Population

A large amount of the activity in clusters is inaccessible by optical observations as it is obscured by hot dust (Poggianti et al., 1999). Observations at infrared and submillimeter wavelengths sample this hot dust directly. The submillimeter luminous galaxies (SMGs) represent a population of young, massive systems in the process of merging and/or interacting, causing very intense starburst and AGN activity (Swinbank et al., 2004; Webb et al., 2005).

A tentative excess of SMGs compared to the field population was detected in $z \sim 1$ cluster fields by Best (2002). He argued that they were more likely cluster members than back ground galaxies. The dust obscured starburst activity in SMGs exhibit star formation rates of ~ 100 $M_\odot$ yr^{-1} which, if these SMGs are truly cluster galaxies, would mean that they are the most intense systems yet seen in clusters (Webb et al., 2005). Based on the bolometric luminosities of $> 10^{12}$ $L_\odot$ from submm flux measurements of a sample of SMGs, they can be classified as ultra-luminous infrared galaxies (ULIRGs) (Swinbank et al., 2004).

These extreme properties make the SMG population an important one to study

for galaxy formation and evolution models and to better understand their role in the cluster environment. Four SMGs were found in the RCS2319+00 cluster field around cluster A at 850 μm using the SCUBA camera on the JCMT (James Clerk Maxwell Telescope). Two of these sources have very bright submm fluxes of $S_{850\mu m} \sim$ 8 mJy and have photometric redshifts consistent with the supercluster. These were also observed in the radio at 1.4 GHz by the VLA and the optical counterparts to the radio detections were included in the spectroscopic survey herein in the hopes of verifying cluster membership for these important sources (see Section 4.6).

Chapter 3

Data Acquisition and Reduction

3.1 The VLT-VIMOS Instrument

Deep optical spectroscopy was obtained for candidate cluster galaxies in the RCS2319+00 cluster field using the European Southern Observatory's (ESO) Very Large Telescope (VLT) Visible Multi-Object Sectrograph (VIMOS). The VLT, located on Cerro Paranal in the Atacama desert in Chile, consists of four 8.2 meter telescopes. The VIMOS instrument is located on the Nasmyth focus B of VLT's Unit Telescope 3 (UT3). It can be operated as a visible wide field imager and a multi-object spectrograph (MOS) in a wavelength range of 360–1000nm (European Southern Observatory, 2008).

VIMOS consists of four 2048×4096 pixels EEV CCD detectors with a field of view of 7 arcminutes by 8 arcminutes for each detector and a gap of $\sim$2 arcseconds between the quadrants. Figure 3.1 shows the layout of the quadrants for a single pointing. Each detector is equipped with grisms and order separating filters (European Southern Observatory, 2008; Le Fèvre, O. and the VIRMOS consortium, 2004).

Grisms are transmission gratings which act as a combination between a diffraction grating and a prism and are designed to preserve an undeviated central wavelength. In addition to the first order grism diffraction used for science, 0^{th}, -1^{st}, and 2^{nd} order diffractions can appear on the detector and contaminate the first order diffractions. The order separating filters are used to remove the overlap of spectra between the first order science spectra and the second order spectra which appears on the detector. The presence of contaminating diffractions is dependent on the slit placement on a mask.

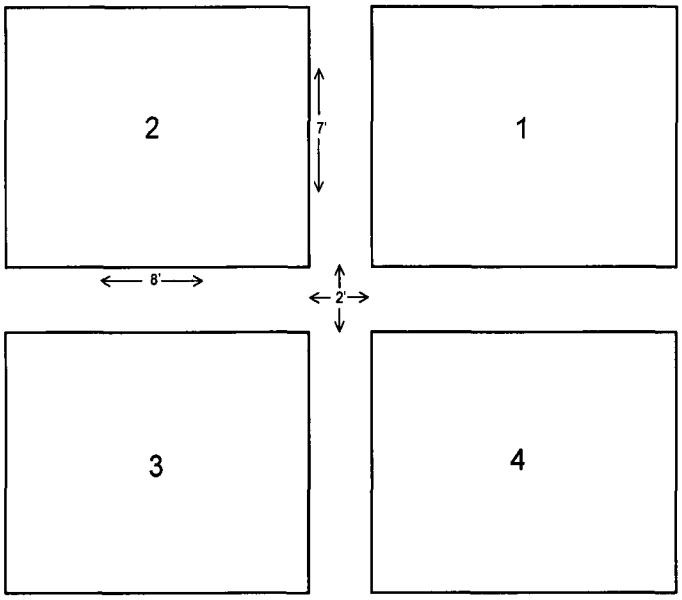

Figure 3.1: Layout of the 4 CCD detectors on the VLT-VIMOS spectrograph. The wavelength dispersion is along the horizontal direction.

Those in the lower (bluer) regions will have 2^{nd} order diffractions at twice the spectral resolution of the 1^{st} order and will contaminate the spectra in the higher (redder) regions of the mask. Conversely, slits in the higher regions of the mask will have -1^{st} order diffraction that contaminate spectra in the lower regions. Contamination from 0^{th} order diffraction occurs on spectra lower in the dispersion direction than a 1^{st} order science spectra. Figure 3.2 shows contamination by 0^{th} and -1^{st} order diffraction when multiplexing spectra along the dispersion direction (Le Fèvre, O. and the VIRMOS consortium, 2004; ESO VIMOS Pipeline Team, 2008).

When multiplexing slits along the dispersion direction, it is important that the slits have the same cross-dispersion position and the same dimensions in order for the sky subtraction procedure to remove the contaminating orders during the pipeline reduction. A mask is designed and laser cut for each quadrant based on pre-imaging done with the wide field imager (Le Fèvre, O. and the VIRMOS consortium, 2004; Giuffrida and Marconi, 2007; ESO VIMOS Pipeline Team, 2008). Figure 3.3 shows

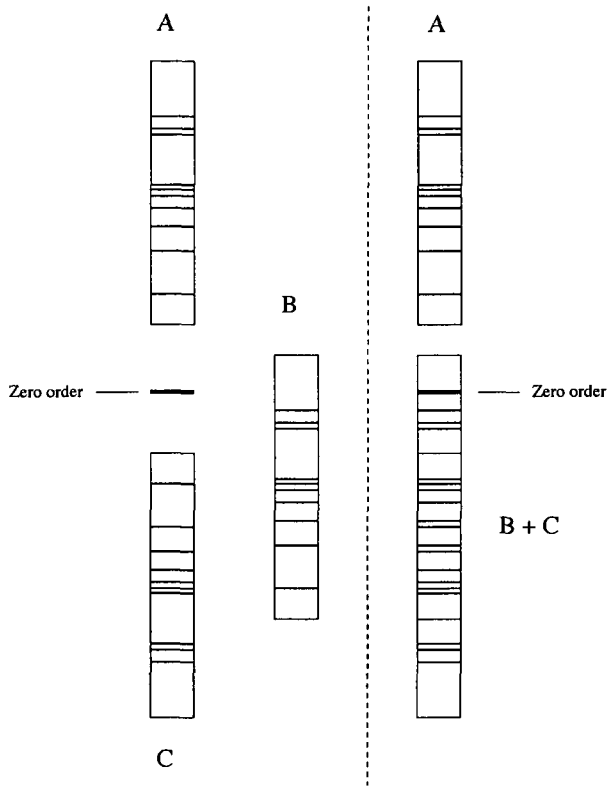

Figure 3.2: Contamination of 0^{th} and -1^{st} order spectra when multiplexing spectra. The left hand side of the figure shows the 0^{th} and -1^{st} (C) orders of spectrum A with a neighboring B spectrum. The right hand side shows the result of multiplexing the two spectra, A and B, along the dispersion direction, with the 0^{th} and -1^{st} orders of spectrum A contaminating spectrum B. From the VIMOS Pipeline Users Manual (ESO VIMOS Pipeline Team, 2008).

mask slits overlaid on a pre-image of a single quadrant in the RCS2319+00 supercluster field.

Fringing effects of the CCD detector are another form of interference not easily removed from the spectroscopic images. These effects happen between the thin silicon layers in CCD detectors. They are a result of the interference between the light incident on the detectors and the internally reflected light. The amount of internally reflected light in a CCD detector depends on the wavelength of the light hitting the detector and the properties of its layers; the number, material and thickness.

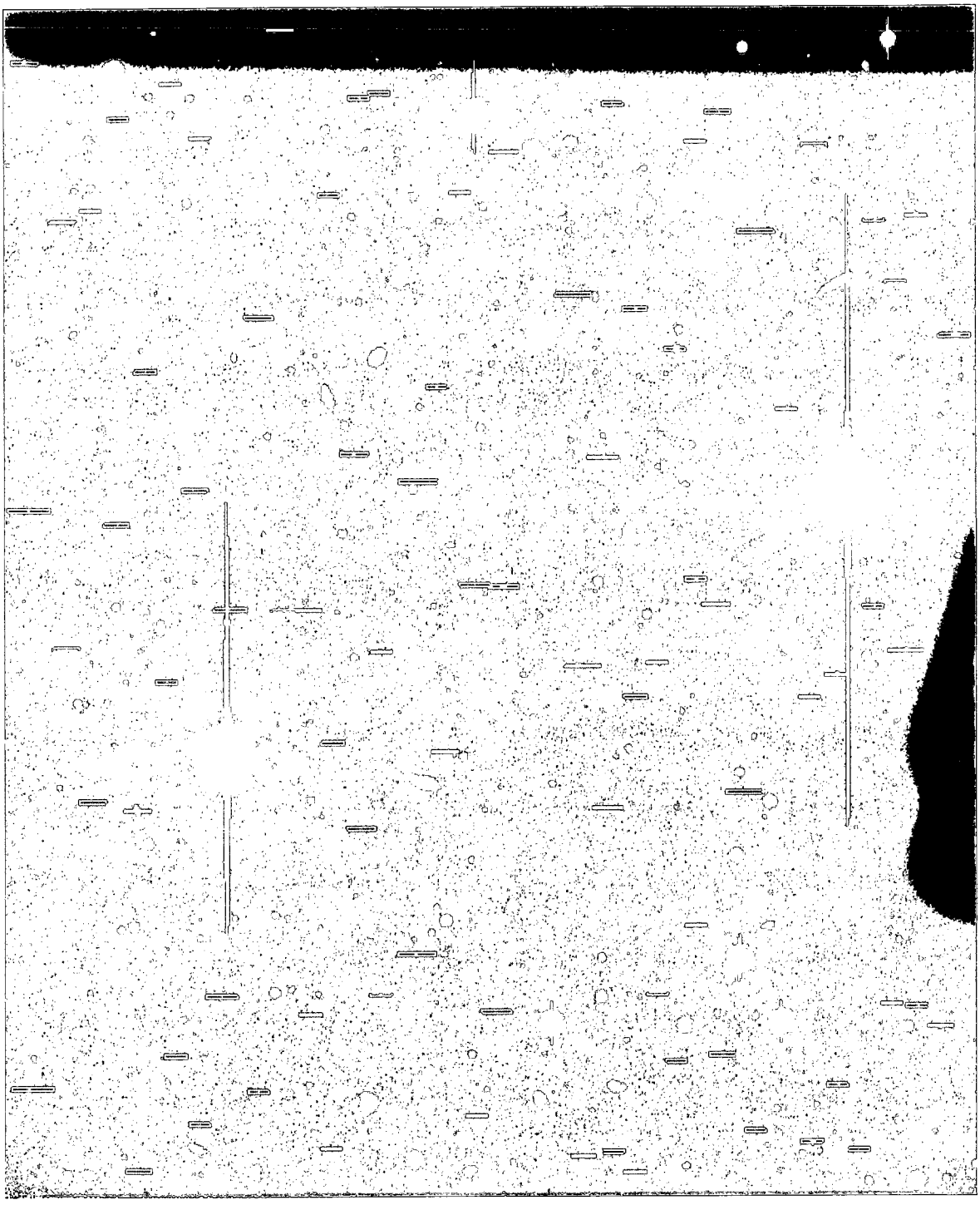

Figure 3.3: Example of a pre-image from one VIMOS quadrant on the RCS2319+00 supercluster field with spectroscopy mask slits overlaid.

Figure 3.4 shows that the fringing effects in optical spectroscopy are more pronounced in the red end of the spectrum. This is due to the fact that more light is internally reflected in the red, where the silicon layers transmit more light (Walsh et al., 2002).

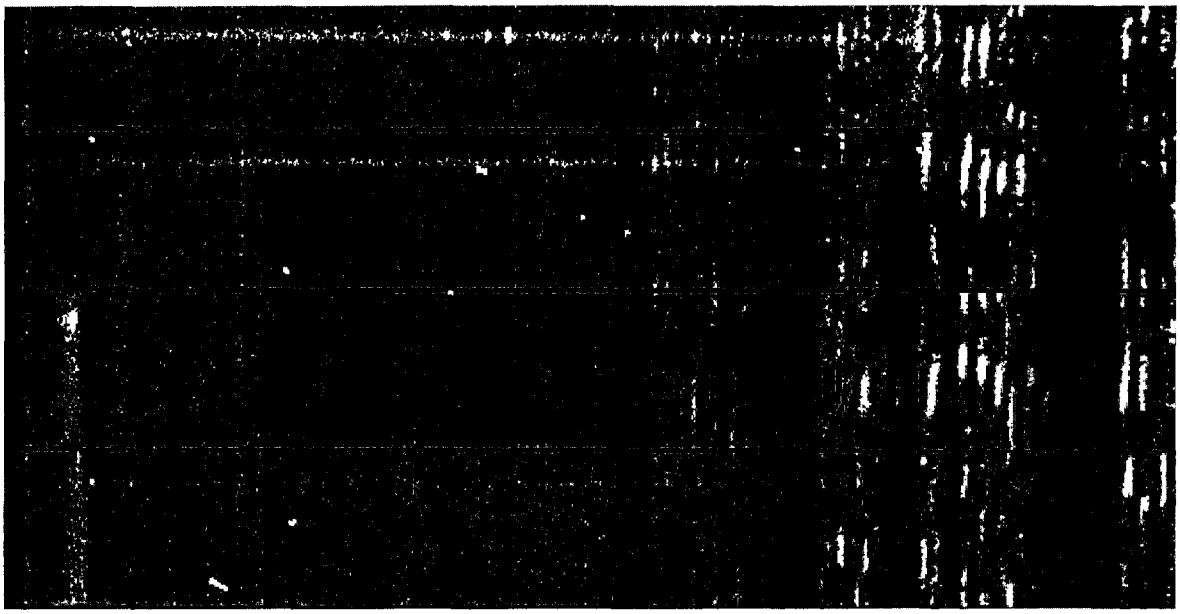

Figure 3.4: Example of CCD fringing effects on 2D reduced optical spectroscopy. Fringing effects are more prominent in the red end of the spectrum.

Due to the high redshift of the RCS2319 superstructure and the limiting optical magnitude of $R \sim 23.5$, the low resolution red grism (LR_red) was chosen for these observations. The VIMOS Exposure Time Calculator indicated that the LR_red grism would be sufficient to reach the continuum of the faint optical counterparts to the radio sources with a signal to noise of ~ 3 in a 1 hour integration. Its wavelength range of 5500–9500 Å easily allows for the presence of the [OII] 3727 Å emission line and the Balmer break Ca H&K absorption lines at 3934 Å and 3969 Å at the cluster redshift of $z = 0.9$. As well, the LR_red grism has a spectral resolution of 210 and has a range of 640 pixels in the dispersion direction of each quadrant, which means that up to four spectra can be stacked along the dispersion direction of the CCD, allowing a large number of slits to be placed on each mask. The dispersion for the

LR_red grism is 7.3 Å/pixel at 7000 Åwith a scale of 0.205 arcsecs/pixel (European Southern Observatory, 2008).

3.2 The RCS2319+00 Supercluster Field Data

At the time of the VIMOS spectroscopy proposal, only the central cluster of the three component clusters in the 2319 superstructure had been identified. As such, this data is centered on this cluster with central coordinates of right ascension: 23:19:53.4 and declination: 00:38:16. Four pointings were taken covering an area of $\sim$ 27 x 27 arcmin. Each pointing, numbered 1–4, have that numbered quadrant positioned on the center of the cluster. For increased confidence in the redshift results, each pointing of the instrument was observed twice (or three times) in order to increase the signal to noise ratio of the data by coadding the spectra. Table 3.1 shows a summary of the observations of the four pointings. The reduced time per observation in pointings 3 and 4 was due to technical issues resulting in telescope overhead time taking away from observation time.

Table 3.1: Summary of VLT-VIMOS observations of the RCS2319+00 supercluster field.

Pointing	Date Observed	Number of Observations	Total Integration Time (s)
P1	09-07-2005	2	2500
P2	13-08-2005	2	2500
P3	22-08-2006	2	1920
P4	16-10-2006	3	2880

Since the primary goal of this observational run was to constrain the cluster membership of the radio population, priority was given to the radio objects when designing the MOS masks. The radio sources available at the time of mask preparation were contained within a 6 x 6 arminute area near the cluster center. The optical counterparts to the radio candidates were chosen with the faintest sources having optical magnitudes of R $<$ 23.5. The radio sources include a possible head-tail, extended

source near the cluster center. This object was placed on two masks to increase the signal to noise. It will be discussed further in Section 4.5. A catalogue of radio galaxies has been assembled from a more recent, larger radio map of the 2319 cluster field. The list of new radio sources was cross referenced with the list of redshift identified sources in this research to add to the information on the radio population (see Section 4.4).

Another important population is the submillimeter galaxy population, identified by the SCUBA 850 μm camera. Two radio-identified SCUBA submillimeter galaxies reside near the center of the RCS2319+00 cluster field. Though it was expected that no continuum would be visible due to the optically faint nature of these objects the hope was that some strong emission lines would be detected. Both sources were placed on multiple masks to increase the S/N ratio (see Section 4.6).

After optimizing the slit positions on the mask to include as many radio galaxies as possible and the two important SCUBA sources, the remainder of the mask space was filled with optical sources. Each mask has between $\sim$ 72 and $\sim$ 94 slits of varying widths between $\sim$ 4.532 to $\sim$ 10.498 arcseconds. In total, the four pointings contain 1372 slits. Some objects, particularly the radio and SCUBA sources, appear on multiple masks and total of 1134 unique candidate cluster sources were observed. In addition, several slits contain two objects either by design or by coincidence and were given the designations a and b for the bottom and top object in the slit respectively. The intended target objects were distinguished from the coincident objects by examining the coordinates of the continuum in the slit from the original 2D spectroscopy files. Figure 3.5 is an example of the 2D spectroscopy data from one quadrant after reduction of all contamination but the sky lines, as discussed below.

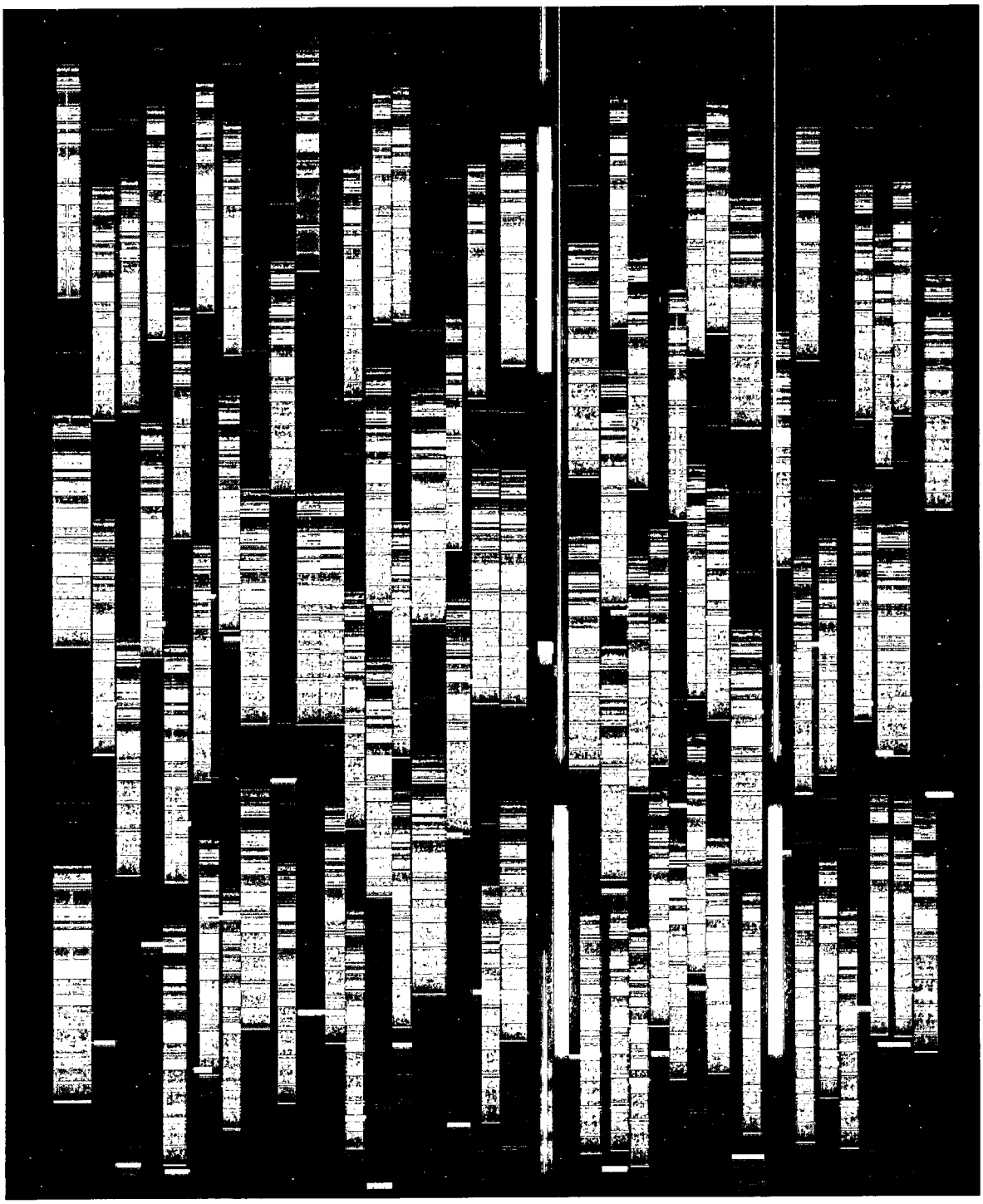

Figure 3.5: 2D multiplexed optical spectroscopy from a single VLT-VIMOS mask. $-1^{st}, 0^{th}$, and 1^{st} order contamination is still visible as shadows on the image. The solid spectra correspond to guide stars.

3.3 Spectroscopy Reduction: VIMOS Pipeline

The RCS2319+00 spectroscopy was run through the standard VIMOS data reduction pipeline of the VLT prior to delivery for analysis. The pipeline reduces the data to the form of stacked one dimensional spectra for each slit on each mask. All original observation files and any created in running the pipeline were included in the package received for data analysis. The following is a brief description of the procedures involved in reducing the data using the VIMOS pipeline.

Along with the observations of the sources in the RCS2319+00 cluster field, exposures were taken for the purpose of flat fielding and de–biasing the images, performing wavelength calibrations, and finding the spectral response curves. In addition, catalogues containing reference emission lines, atmospheric extinction, standard flux for reference stars, and the grism's spectral intervals were included for calibration purposes. All files are in the standard FITS (Flexible Image Transport System) format. The total list of files required for each mask in order to perform the data reduction are as follows:

- 1 one pre-image of the cluster field
- 1 science exposure
- 5 bias exposures
- 3 screen flat field exposures associated with the science exposure
- 1 arc lamp exposure for the science exposure (He + Ar lamp)
- 1 standard star field exposure
- 1 standard star exposure
- 3 screen flat field exposures for the standard star field exposure
- 1 arc lamp exposure for the standard star field exposure (He + Ar lamp)
- 1 LR_red grism table
- 1 line catalogue
- 1 atmospheric extinction table
- 1 standard flux for reference standard stars table

The VIMOS pipeline was developed to account for known geometrical distortions

affecting the instrument. Optical distortions including CCD to mask transformations and mask to CCD transformations have been modeled by polynomial fitting. Spectral distortions including the $0^{th}, -1^{st}$ and 2^{nd} order contamination are also taken into effect (Le Fèvre, O. and the VIRMOS consortium, 2004).

The pipeline contains five basic steps to reduce the data. First, the five bias frames are used to create an averaged master bias calibration frame. This in turn is used in combination with the three screen flat field exposures for the science data and the grism table to produce two files; the master screen flat field image and a non-normalized screen flat field. An extraction table is then produced from the arc lamp spectrum, the master bias calibration frame, the non-normalized screen flat field, the grism table and the line catalogue. This extraction table is later used to perform a wavelength calibration and spectral tracing. This step also produces the extracted arc lamp spectrum, which can be used to test the performance of the extraction table by observing the alignment of the emission lines (Le Fèvre, O. and the VIRMOS consortium, 2004; ESO VIMOS Pipeline Team, 2008).

The fourth step in the pipeline reduction is the creation of a spectrophotometric table that describes the instrument efficiency and the spectral response curve for the standard stars. It is produced from the standard star exposure, the extraction table, the grism table, the atmospheric extinction table and the standard flux table for the specified standard star. It is during this step that known bad pixels for each quadrant of the VIMOS instrument are corrected (Le Fèvre, O. and the VIRMOS consortium, 2004; ESO VIMOS Pipeline Team, 2008).

The fifth and final step is the creation of the flat fielded, de-biased, flux and wavelength calibrated, sky subtracted science exposure. The master bias calibration frame, extraction table and spectrophotometric table created for the specific data is used in combination with the grism table and the atmospheric extinction table to

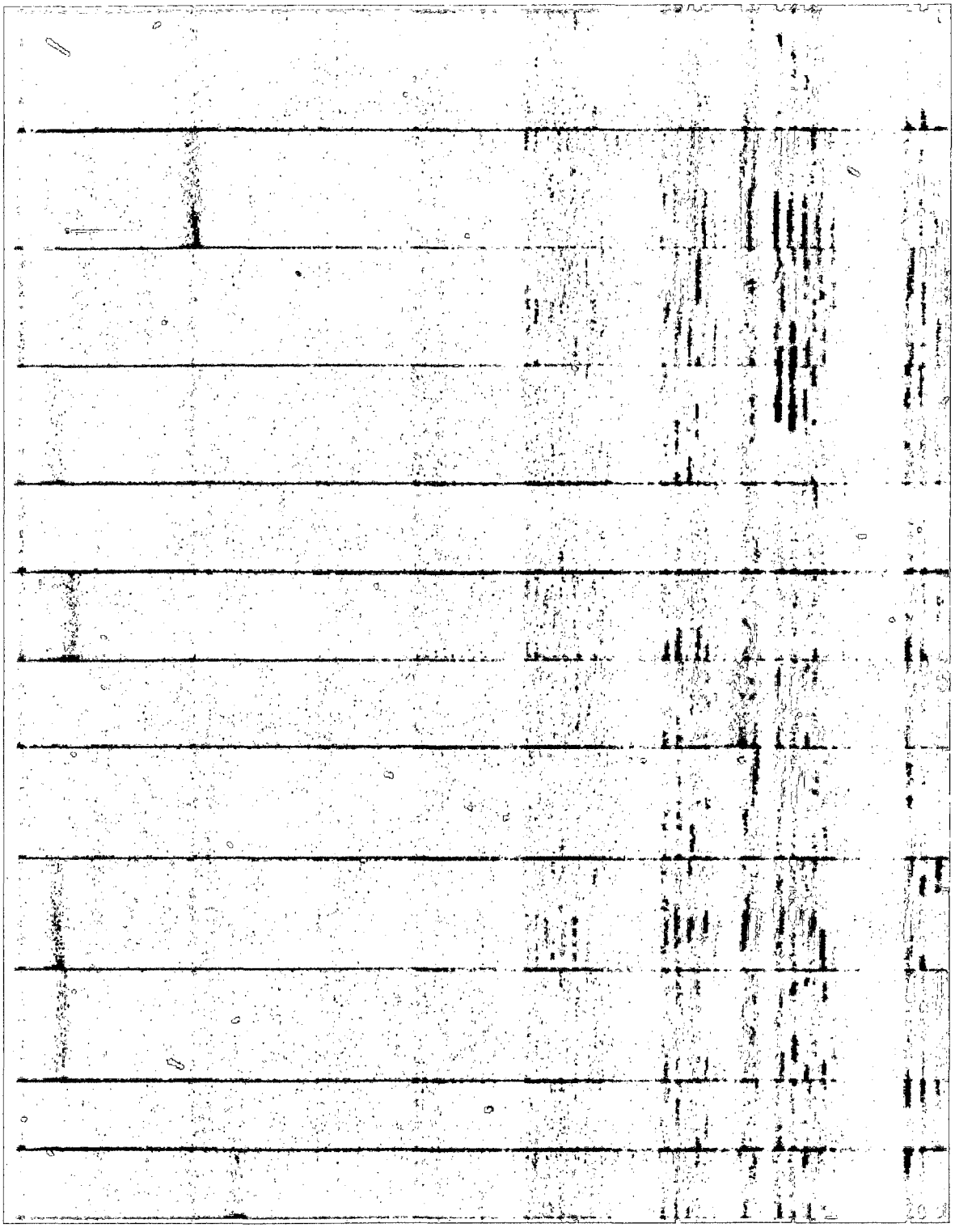

Figure 3.6: Example of a subset of stacked 2D spectroscopy as reduced by the VIMOS pipeline.

produce the final spectroscopy files. A file containing the stacked two dimensional, sky subtracted slit spectra is produced, as shown in Figure 3.6. From this 2D spectra file objects are extracted into a file containing the stacked 1D spectra for each slit, shown in Figure 3.7. In addition, the sky lines in the form of 2D slit spectra and 1D extracted spectra are created to be used for quality control (ESO VIMOS Pipeline Team, 2008; Giuffrida and Marconi, 2007).

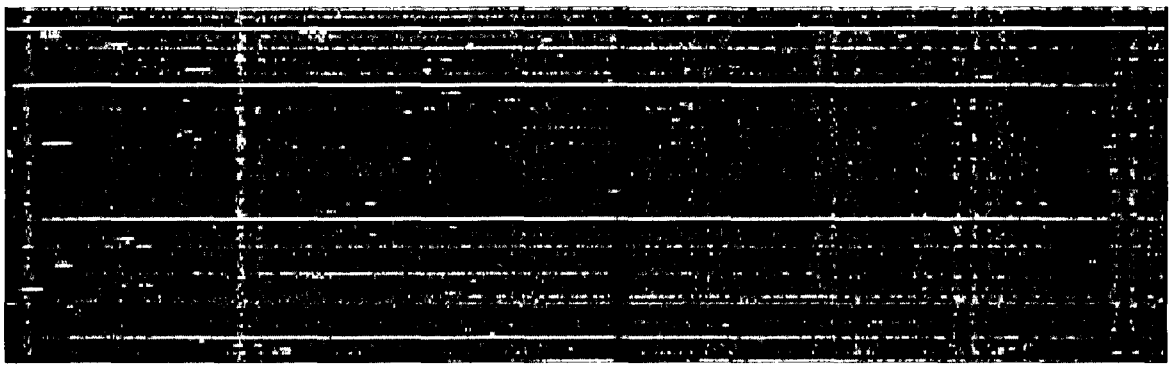

Figure 3.7: Stacked 1D spectroscopy as reduced by the VIMOS pipeline. Each horizontal line corresponds to the extracted spectra from the corresponding slit. 0^{th} order contamination is seen for many slits as very intense regions, mainly at the blue end of the spectrum.

This pipeline does not include any defringing. Removal of CCD fringing effects requires detailed knowledge of the CCD construction and materials as well as numerous flat field images and so could not be done manually.

3.4 Spectroscopy Reduction: IRAF

Once the 1D pipeline reduced spectra had been reviewed, it was decided that the pipeline reduced data would be used only up to the stage of the 2D slit spectra. This was decided for a number of reasons. Firstly, the 1D extracted spectra assume only one object per slit and so several objects were missing from the 1D spectra. The object extracted for those multiple object slits could not be verified as being

the primary or secondary object. Figure 3.8 shows an example of 2D spectroscopy with two continuum lines corresponding to the primary target object and a coincident object.

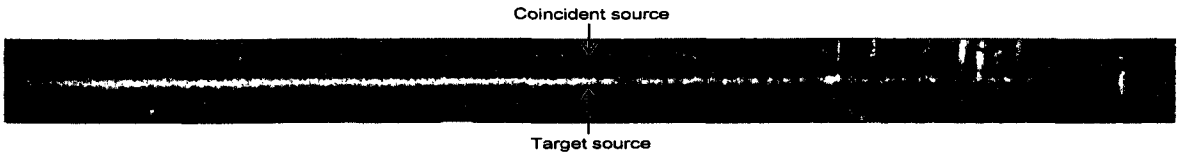

Figure 3.8: Example of a primary target galaxy with visible emission line (center/bottom continuum) and a faint coincident source (top continuum) found in a single spectroscopy slit.

Also, for those galaxy sources with very faint continuum, the 1D extraction was not trusted to have traced the actual galaxy source. For those galaxies where no continuum is present, the 1D extraction is still present and most likely tracing the highest noise line of the 2D spectra. In addition, it is much more difficult to identify spurious emission and absorption when the position of the tracing relative to the 2D slit is not known explicitly. Figure 3.9 is an example of a 2D spectrum with residual 0^{th} order and cosmic ray contamination. It was therefore decided that new 1D spectra would be reduced from the pipeline reduced 2D spectra.

Figure 3.9: Example of common contamination of a VIMOS 2D spectrum from 0^{th} order contamination, cosmic rays and CCD fringing.

3.4.1 Manual Source Finding

For each data set of reduced 2D galaxy spectra, a list of apertures was manually compiled by visually inspecting the data from each slit to search for continuum emission.

The vertical pixel position of the the continuum emission was recorded into aperture files in a format compatible with the IRAF *apall* task.

For those slits where no continuum emission could be seen, no 1D extraction was performed as we could not be sure that any trace performed would be anything more than background noise and no meaningful redshift calculation was expected for these sources. Any residual artifacts, such as cosmic rays and interference effects due to $0^{th}, -1^{st}$ and 2^{nd} order contamination from neighboring spectra not removed in the initial data reduction were noted to be removed from the final reduced 1D spectra.

3.4.2 1D Spectra Reduction with IRAF

The rest of the reduction was performed using the Image Reduction and Analysis Facility (IRAF), an interactive software system capable of reducing, manipulating, and viewing many forms of astronomical data (Tody, 1993). This research used the *apextract* package, accessed through the hierarchy of packages as follows: *noao* (National Optical Astronomy Observatories package), *onedspec*, *twodspec*. Within the *apextract* package, the *apall* task controls all the parameters needed for extraction of 1D spectra from 2D multiple spectra files. With the dispersion axis set along wavelength lines, specified in the *apextract* parameters file, the *apall* task was run. The *apall* parameters used in the reduction can be found in Appendix D.

3.4.3 Tracing the 1D Spectra

Since the centerline of the aperture positions was pre-specified through manual observations, no aperture finding, re-centering, or resizing was done. Tracing the position of the spectra along the dispersion axis, i.e. the wavelength range, was done interactively. Tracing is important since the spectra rarely follow a horizontal line across the slit. Figure 3.10 shows an example of a screen capture of a typical interactive

aperture trace with the continuum drifting horizontally within the width of the slit.

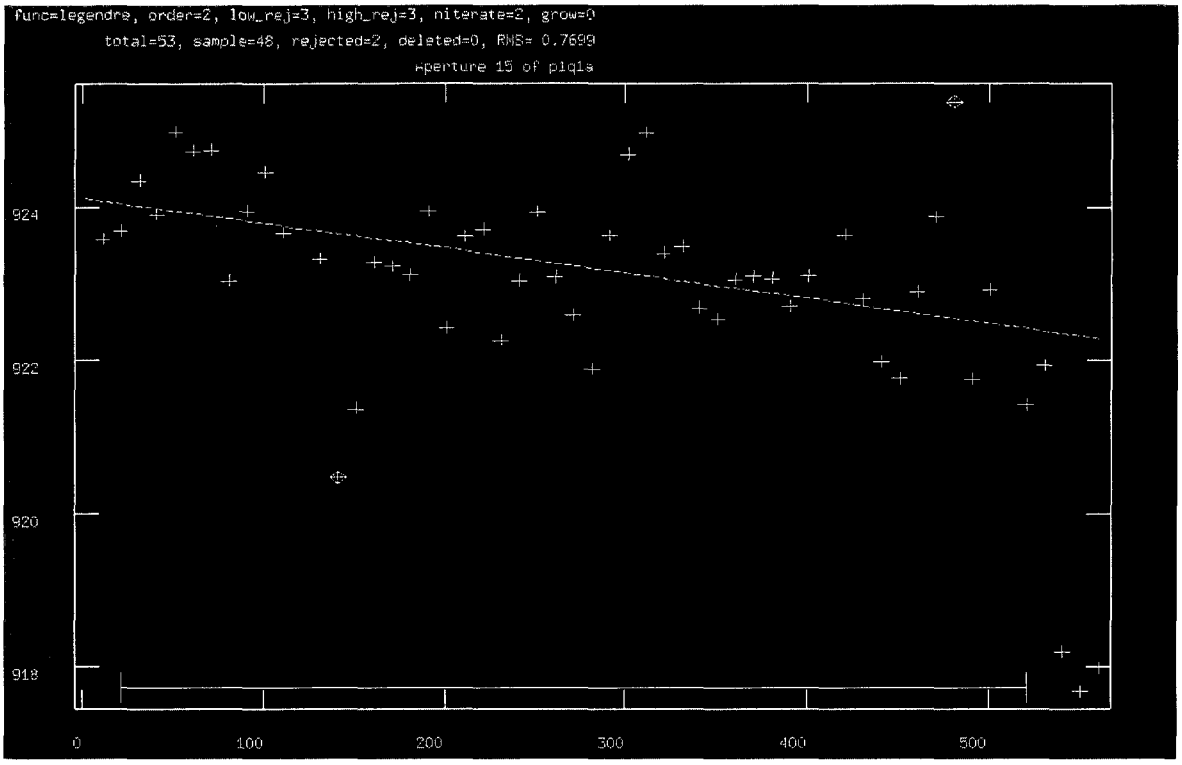

Figure 3.10: Screen capture of an interactive aperture trace showing the horizontal pixel position within the slit on the y-axis and wavelength along the x-axis of the pixel with the greatest intensity (either high or low) above the background. The region used for tracing is defined by the barred line along the bottom of the x-axis. Outlying data points are automatically discarded, as seen by the two marked out points. The aperture is traced with a second order polynomial.

The spectral profiles used for tracing the apertures are determined for each wavelength along the spectrum. They are created by averaging a specified number of image profiles which come before each consecutive wavelength using the curve specified for background subtraction (b_funct = chebyshev, b_order = 2). The program assumes that the profile of the spectrum changes slowly along the wavelength range so that averaging profile shapes near a desired wavelength will be an accurate representation of the spectral profile for that wavelength (Valdes, 1990b)

When tracing the apertures interactively, the position of the spectrum profile at wavelength positions defined by the tracing step (t_step = 10 Å) are plotted.

A second order Legendre function is fit interactively to the data by defining the optimal wavelength region over which to trace and ignoring any far outliers not already rejected by IRAF. The trace often deteriorates in the red end of the spectrum due to the CCD fringing, which is why the reddest end of the spectrum is often unreliable for an accurate trace. Really bad traces were recorded and often resulted in very offset or noisy 1D spectra for which no redshift could be determined. As each aperture is traced, the aperture file is updated to include the new information.

3.4.4 Background and Bad Pixel Subtraction

Additional background subtraction was performed in an effort to increase the S/N of the 1D spectra over the initial pipeline reduced reduction. A Poisson variance weighted sum of the pixels along the spatial axis of the apertures at each wavelength is calculated. Variance weighting was chosen as it results in the best unbiased S/N estimate for the pixel intensities. The variance uses Poisson statistics of a linear quantum detector as the basis model for the weighted fit to the background S/N:

$$f = \frac{\sum(I - B)/V}{\sum(P^2/V)}, \tag{3.1}$$

where the fit is summed over the width of the aperture. The variables are defined as follows: P is the normalized profile model, I represents the pixel intensities, B denotes background intensities, and V is the variance in pixel intensities. The P^2/V term represents the extracted weighting for the fit (Valdes, 1990b; Valdes, 1990a)

Bad pixels, such as cosmic rays, are located and replaced with model points in the average profiles. The normalized profile is scaled to the image profile using a chi–squared fit:

$$M = P \left\{ \frac{\sum((I - B)\ P/V)}{\sum(P^2/V)} \right\} \tag{3.2}$$

where the fit is summed over the width of the aperture. By default, any pixel intensities having values outside of four (lsigma & usigma = 4) times the root mean squared of the chi-squared fit are rejected and the fit is repeated with the bad pixels removed (Valdes, 1990b; Valdes, 1990a).

3.4.5 Quality Check of Spectroscopy Reduction

Once all apertures were traced for a specific mask in a specific data run, the 1D sky files corresponding to that data set were extracted. The same apertures traced in the 2D spectra files were used to run a non-interactive extraction on the 2D sky spectra, shown in Figure 3.11. The background subtraction and weighting was changed to equal 'none' and no aperture editing was done.

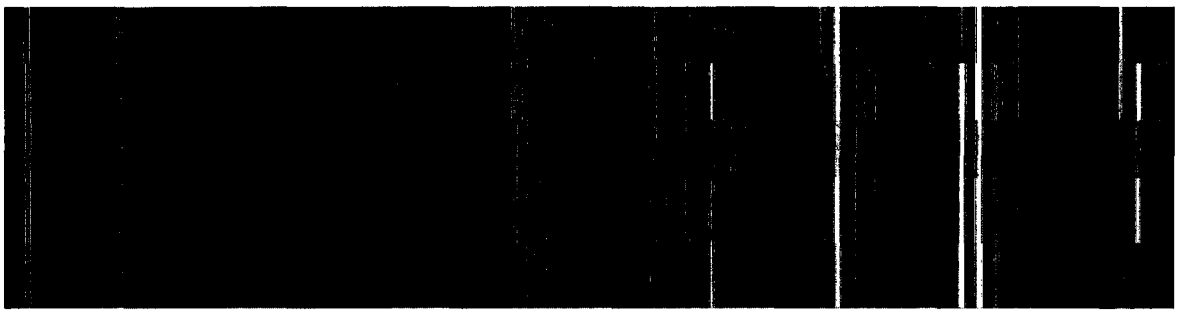

Figure 3.11: Example of 2D spectra showing sky lines. The alignment of the sky lines is used to check the wavelength calibration of the VLT-VIMOS reduction.

Next, the dispersion direction was changed to be along the wavelength columns rather than along the wavelength range (i.e. in the direction of the width of the apertures) and the number of dispersion lines along which to sum the trace and the tracing step (t_nsum & t_step) were changed to equal one. A trace was then done interactively to look at the sky lines. This effectively stacks all spectra into a 1D form with the plotted flux representing the intensity of the sky lines at different wavelengths.

The idea is that all sky lines in each slit should line up with the same sky lines in

all other slits. A few isolated sky lines were marked and traced to look for slits where the sky lines were shifted. A first order polynomial fit was used to set the fit lines equal to a flat line. Outliers were recorded for each of the sky lines that were looked at. Some scatter is expected but the hope is that the RMS of the dispersion for each of the traced sky lines is between $\sim 0.3 - 0.5$ pixels. The average RMS gives the error for the wavelength calibration using the LR_red dispersion value of 7.3 Å/pixel. For an average RMS of 0.4, the error on the wavelength calibration would be 2.9 Å. The velocity dispersion, $\Delta\nu$, for this error can be found by finding the spectral resolution, R, at a mean wavelength. The spectral resolution is defined as:

$$R = \frac{\lambda}{\Delta\lambda} \tag{3.3}$$

$$R = \frac{c}{\Delta\nu} \tag{3.4}$$

Therefore, for a mean observed wavelength of 7000 Å, the velocity dispersion would be ~125 km/s. This translates to a rest–frame velocity dispersion of $\sim$ 65 km/s for the RCS2319+00 cluster redshift of z=0.9. While not ideal, this value is adequate for redshift calculations and implies that the wavelength calibration done by the VIMOS pipeline is sufficient for our analysis. Individual spectroscopic redshift measurements usually have uncertainties of 100 km/s (Danese et al., 1980). A summary of the average RMS values and corresponding velocity dispersions at the cluster redshift is given in Table 3.2.

3.4.6 Coadding the Spectra

Once all sky checks were completed to ensure that the wavelength calibrations for each quadrant in each pointing did not vary too much between data runs, all data

Table 3.2: Summary of the approximate error in wavelength calibration for each data set.

Sky File	Average RMS (pix)	Error in Wavelength Calibration (Å)	Velocity Dispersion at z=0.9 (km/s)
P1Q1a	0.369	2.7	61
P1Q1b	0.345	2.5	56
P1Q2a	0.344	2.5	56
P1Q2b	0.345	2.5	56
P1Q3a	0.331	2.4	54
P1Q3b	0.338	2.5	56
P1Q4a	0.358	2.6	59
P1Q4b	0.377	2.8	63
P2Q1a	0.314	2.3	52
P2Q1b	0.323	2.4	54
P2Q2a	0.286	2.1	47
P2Q2b	0.290	2.1	47
P2Q3a	0.433	3.2	72
P2Q3b	0.451	3.3	74
P2Q4a	0.319	2.3	52
P2Q4b	0.300	2.2	49
P3Q1a	0.391	2.9	65
P3Q1b	0.339	2.9	65
P3Q2a	0.339	2.5	56
P3Q2b	0.335	2.4	54
P3Q3a	0.366	2.7	61
P3Q3b	0.358	2.6	59
P3Q4a	0.313	2.3	52
P3Q4b	0.385	2.8	63
P4Q1a	0.360	2.6	59
P4Q1b	0.418	3.1	70
P4Q1c	0.362	2.6	59
P4Q2a	0.415	3.0	68
P4Q2b	0.329	2.4	54
P4Q2c	0.371	2.7	61
P4Q3a	0.400	2.9	65
P4Q3b	0.385	2.8	63
P4Q3c	0.460	3.4	77
P4Q4a	0.357	2.6	59
P4Q4b	0.385	2.8	63
P4Q4c	0.362	2.6	59

sets (2 for pointings 1–3, 3 for pointing 4) for each quadrant in each pointing were coadded using the IRAF *imarith* task in the *imutil* package, accessed through the *images* package. The reason that the spectra were not coadded in their 2D form is

due to the unfortunate fact that shifts were present in the vertical pixel position of slits. This offset is often only a couple of pixels throughout all slits in a mask between data runs but sometimes the effect started with a shift of a pixel or two and grew to as many as ~20 pixels by the last mask slit. This made it too impossible to perform a reliable automated coaddition of the 2D spectra data sets.

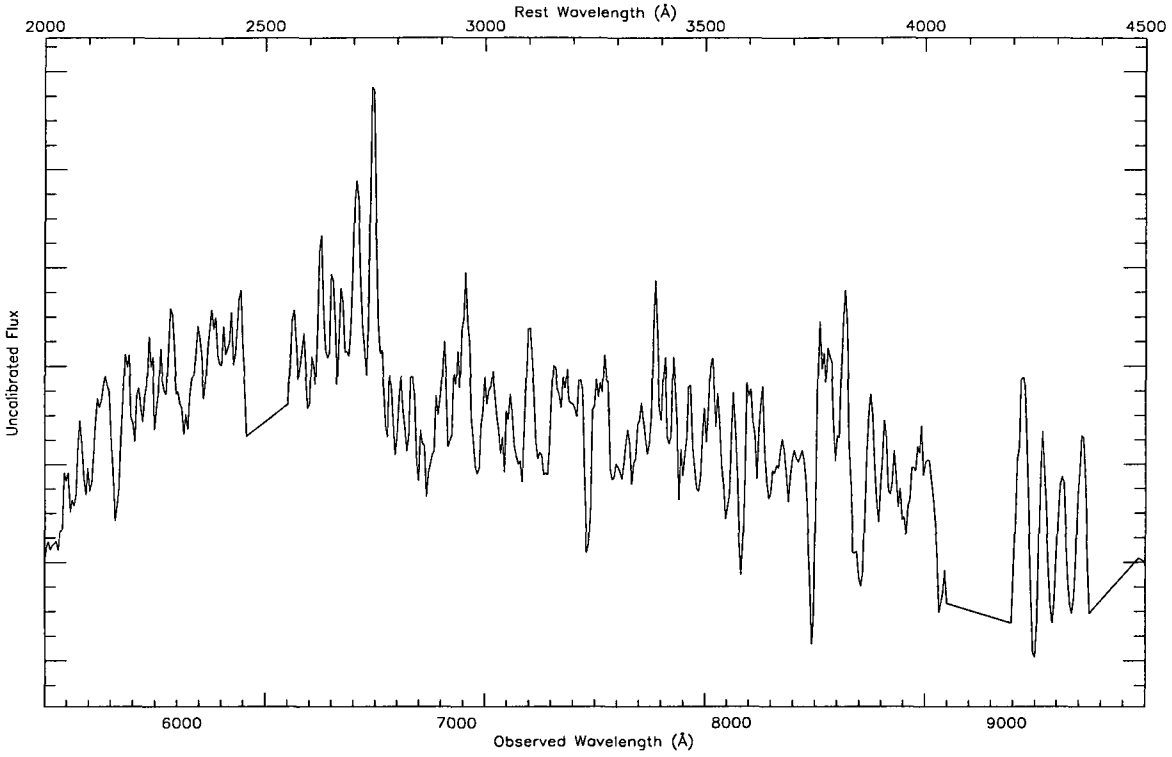

Figure 3.12: Example of 1D spectra after additional manual bad pixel reduction. The regions of straight connecting lines represent areas of the spectrum where contamination from 0^{th} order overlap, extended cosmic ray interference, and bad CCD fringing were manually removed.

The resulting 1D coadded spectra were displayed using the *splot* task in the *onedspec* package. For each aperture, any residual bad pixels caused by cosmic rays or some other pixel artifact, left over zeroth order contamination, and bad CCD fringing effects were removed from the spectrum and the file was rewritten. These corrections, if over a large enough wavelength range, can be seen as flat areas on the spectrum as close to the zero flux value as possible, as shown in Firgure 3.12. Once all bad pixels

and interference ranges were removed, the 1D spectra were ready to be analyzed to find redshifts for the candidate cluster galaxies.

Chapter 4

The RCS2319+00 Spectroscopic Redshift Catalogue

4.1 Identifying Redshifts

Spectroscopic redshifts are derived by identifying the shift in emission and absorption lines of galaxy spectra and comparing them to the corresponding rest frame emission or absorption line for the identified element, as shown in Equation 4.1.

$$z = \frac{\lambda_o - \lambda_e}{\lambda_e} \tag{4.1}$$

This can be done by visual inspection to search for strong emission and absorption lines and/or by using cross-correlation programs with template galaxy spectra to identify the most likely redshift of a given input spectra. A list of common galaxy rest frame emission and absorption lines is found in Table 4.1. The ionized gas which causes emission lines in the spectra of galaxies is produced through various means, including heating by star formation in HII regions and photoionization by AGN (Yan et al., 2006).

Due to the high redshift nature of the RCS2319+00 superstructure, the task of identifying redshifts with optical spectroscopy becomes more difficult as many of the common emission lines used for redshift identification, such as [H_β] 4861 Å, the oxygen doublet [OIII] at 4959 Å and 5007 Å, and [H_α] 6563 Å are either shifted off of the red end of the spectrum or, if present, are confused by the large amount of CCD fringing present in the VLT-VIMOS data. Also, because many of the candidate cluster galaxies studied in this research are faint in the optical, particularly the important radio and

Table 4.1: Rest frame wavelengths for emission and absorption lines commonly found in galaxy spectra.

Wavelength (Å)	Element	Wavelength (Å)	Element
3123	OIII	4304	G_{band}
3133	OIII	4341	H_γ
3303	NaI	4363	[OIII]
3312	OIII	4472	HeI
3347	[NeV]	4658	[FeIII]
3427	[NeV]	4686	HeII
3727	[OII]	4861	H_β
3760	[FeVIII]	4959	[OIII]
3868	[NeIII]	5007	[OIII]
3889	HeI	5174	MgIb
3934	CaIIK	6548	[NII]
3969	CaIIH	6563	H_α
3968	[NeIII]	6583	[NII]
4101	$[H_\delta]$	6678	HeI
4250	[FeII]	6716	[SII]
4281	[FeII]	6731	[SII]

SCUBA sources, very little continuum is present for many of the candidates, making the S/N ratio low for those sources.

For these reasons it was decided that the best way to determine accurate redshifts for the largest number of candidate cluster galaxies possible was to perform a visual inspection of all 1D spectra and 2D spectra simultaneously. The analysis contained in this thesis displays the results of this redshift identification method.

A follow-up study is currently underway by a collaborator, Erica Ellingson, to run all reduced, coadded, clean 1D spectra through a correlation program which she has written and is adjusting to handle the high redshift sources in this survey. The hope is that the correlation program will be able to identify additional redshifts from sources with no visible emission lines as well as to corroborate the redshift identifications of some of the confidence level 3 detections (a detailed explanation of the confidence levels used in this survey is found below). On a trial of the first three masks, the correlation program was able to identify a handful of new redshifts for each mask. For

this reason we expect $\sim$ 80 new redshift identifications will come out of the correlation program. In comparison, 638 redshifts were identified by the less sophisticated visual identification method (see Section 4.2).

For the visual identification, the 2D spectra were viewed with the SAOImage DS9 program while the corresponding 1D spectra were viewed with the IRAF *splot* task mentioned previously. It was during this stage that the remaining bad pixels from cosmic rays, zeroth order contamination, fringing and other effects described in Section 3.4 were removed from the 1D spectra.

To ease the distinction between real emission lines on the 2D spectra and spurious emission from fringe lines and other factors, all 2D spectra corresponding to the 1D spectra being analyzed were viewed simultaneously. SAOImage DS9 contains a function wherein separate image frames can be viewed in the same region of the screen and alternated either manually or automatically. When the continuum lines for sources were lined up between the two (or three for pointing 4) data sets and the images were alternated, true emission lines, even faint ones, were able to be discerned from the interference coincident on the continuum.

For true emission lines appearing on the 2D spectra, the corresponding emission lines were found on the 1D spectra and a gaussian curve was fit to find the peak of the emission line. In the best case scenario, two or more emission lines were present and a reliable redshift, given a confidence value of 1, could be determined for the candidate galaxy. The second best scenario is the one wherein one reliable emission line is present along with one or more reliable absorption lines. These redshift determinations were also given a confidence level 1 classification.

When looking for absorption lines in the 2D and 1D data, care had to be taken not to mistake the A-band and B-band Fraunhofer atmospheric absorption lines with spectral absorption lines. The A-band and B-band atmospheric lines lie between

7594–7621 Å and 6867–6884 Å respectively. Both bands correspond to O_2 strong atmospheric absorption (Jenkins and White, 1957). The A-band is more prevalent on the data contained herein.

For spectra where only one emission line was present, the first assumption was to label that emission line as [OII] 3727 Å, the most common and prominent emission line in galaxy spectra. The [OII] 3727 Å emission is actually a forbidden emission doublet at 3726.2 Å and 3728.9 Å, caused by the ionized oxygen in the low density outer regions of galaxies (Burbidge et al., 2004). Strong [OII] emission is often attributed to star formation in galaxies, though it has been found that other processes such as AGN heating, cooling flows, and shock waves can contribute significant [OII] emission. This emission is detected in approximately half of all early-type elliptical galaxies and in roughly 40% of all red galaxies, with strengths comparable to those found in star forming galaxies (Yan et al., 2006).

The shape of the 1D spectrum and the amount of continuum were investigated to better see if the emission line could be justified as [OII] or if it corresponded instead to [OIII] 5007 Å or H_α 6563 Å. If a source galaxy is bright in the optical and has a large amount of continuum emission, certain line identifications can be eliminated based on the likelihood of such a bright source being at high redshift. For example, if a strong emission line is present at 9100 Å in a brighter source, it is most likely not associated with [OII] 3727 Å, which would place it at $z = 1.44$, too high a redshift for a bright source.

If present, the 4000 Å break gives the best justification for labeling a single emission line based on shape. The 4000 Å break is one of the largest breaks present in the spectra of galaxies and the one which we expect to see in our optical spectroscopy at $z = 0.9$. It features increasing emission to the red side of the break and decreasing emission to the blue side of the break. It occurs when ionized metals in galaxies cause

numerous spectral lines to appear within a small wavelength region of the spectrum. As such, the 4000 Å break is more pronounced for old elliptical galaxies (red galaxies) that are metal rich than for young galaxies containing hot stars (Kauffmann et al., 2003). Using the position of the break relative to the emission line, the identification of the single emission line as [OII], [OIII], or H_α can be justified. An example of a strong 4000 Å break identification can been seen in Appendix C for the galaxy with ID 9011555 at $z = 0.6225$.

If no 4000 Å break is present the shape of the continuum can still be used to help identify single emission lines. Starburst galaxies and some types of AGN show an increase in continuum towards the blue end of the spectrum, with emission blue-ward of [OII] increasing more sharply (Kinney et al., 1996). Using this feature, spectra with a single emission line are examined. In star forming galaxies it is expected that both [OIII] and H_α would be present, and that both lines in the [OIII] doublet would also be visible. If a single line is present and cannot be justified as [OII] due to the shape (i.e. no 4000 Å break or sharp increase of blue continuum emission), then the regions where one would expect to find accompanying emission from either the [OIII] or H_α emission lines are searched for contamination from 0^{th} order spectra, cosmic rays, and CCD fringing that would account for the absence of the expected lines. These single emission line redshift determinations were given confidence values of 2 unless the amount of emission and the shape of the spectra were strong enough indicators to classify the redshift with a higher confidence 1 value.

Spectra where a possible faint emission line was visible on the 2D spectrum and was not significantly above the S/N in the corresponding 1D spectrum were given a confidence value 3, the lowest in the catalogue. These values will not be used in published catalogues of this cluster or for determination of velocity dispersions but are retained nevertheless for informational purposes. It is expected that some of these

sources can be given higher confidence ratings after the follow up correlation program has been completed.

The error on the redshift determinations is taken to be $\Delta z \sim 0.002$. This error takes into account the largest error on the wavelength calibration, shown in Table 3.2, of 77 km s^{-1} and the instrument's dispersion of 7.3 Å/pixel. Together these two factors give an error of $\Delta\nu \sim 390$ km s^{-1}.

For redshift determinations of all confidence levels, the 1D spectrum was plotted with both the observed wavelengths and rest wavelengths labeled. As well, the most common emission and absorption lines were overplotted for the determined redshift value and the main CCD fringing intervals were hatched out to avoid confusion. Each plot is labeled with the mask from which it came, its aperture number, the object ID, the calculated redshift, and the assigned confidence level. These plots were used to increase the confidence of some redshift determinations by identification of emission and absorption features not previously obvious based on the 2D data. Plots for the cluster members and radio galaxies are included in Appendices B and C.

For any object which was observed in more than one mask and for which a redshift was determined for more than one observation, the 1D spectra from the two (or three) observations were coadded to increase the S/N of the spectrum and a new redshift was calculated. For any slits having two objects the coordinates for the slit center were compared with the coordinates of the intended target object and the positions of the two sources within the slit to help distinguish the intended object from the coincident one. The secondary object was given a designation of TargetID#.1 to distinguish it from the primary target object for any future comparison with object coordinate lists.

4.2 VLT–VIMOS Redshift Catalogue

In total, 638 redshifts of all confidence levels (1-3) were determined from the 1134 sources in the VLT–VIMOS spectroscopy survey on the RCS2319+00 cluster field. Of these, 49 were identified as cluster members having redshifts in the range $0.8857 \leq z \leq 0.9239$. This cluster redshift range was determined after combining the data from this survey with the IMACS spectroscopy catalogue from Gilbank et al. (2008). The process by which this was done is explained in Section 4.3.3. The spectroscopic redshift catalogue of VLT–VIMOS sources in the RCS2319+00 supercluster field is included in Appendix A.

The redshift histograms for the VLT–VIMOS spectroscopy are shown in Figure 4.1. The filled histogram indicates confidence 1 redshift values, the hatched histogram shows all confidence 1 and 2 redshifts, and the open histogram contains redshifts from all three confidence levels. The lack of confidence 1 redshifts past $z \sim 1$ is due mainly to the bad CCD fringing effects, which begin to confuse the strongest absorption line features (i.e. Ca H&K) in addition to the prominent H_β and [OIII] emission lines.

The bin size used is $z = 0.01$ which corresponds to a relative radial velocity of $\sim$ 1600 km s^{-1} for a system at $z \sim 0.9$. Equation 4.2 gives the formula for the relative radial velocity.

$$\nu = c\frac{(z - z_c)}{(1 + z_c)} \tag{4.2}$$

The cluster redshift of $z_c = 0.90$ is used with a Δz of 0.01 to give a relative radial velocity in the rest frame of the cluster of $\Delta\nu = \pm 1578$ km s^{-1}. This bin size was chosen to be consistent with that used by Gilbank et al. (2008) for the IMACS spectroscopy of the RCS2319+00 cluster field.

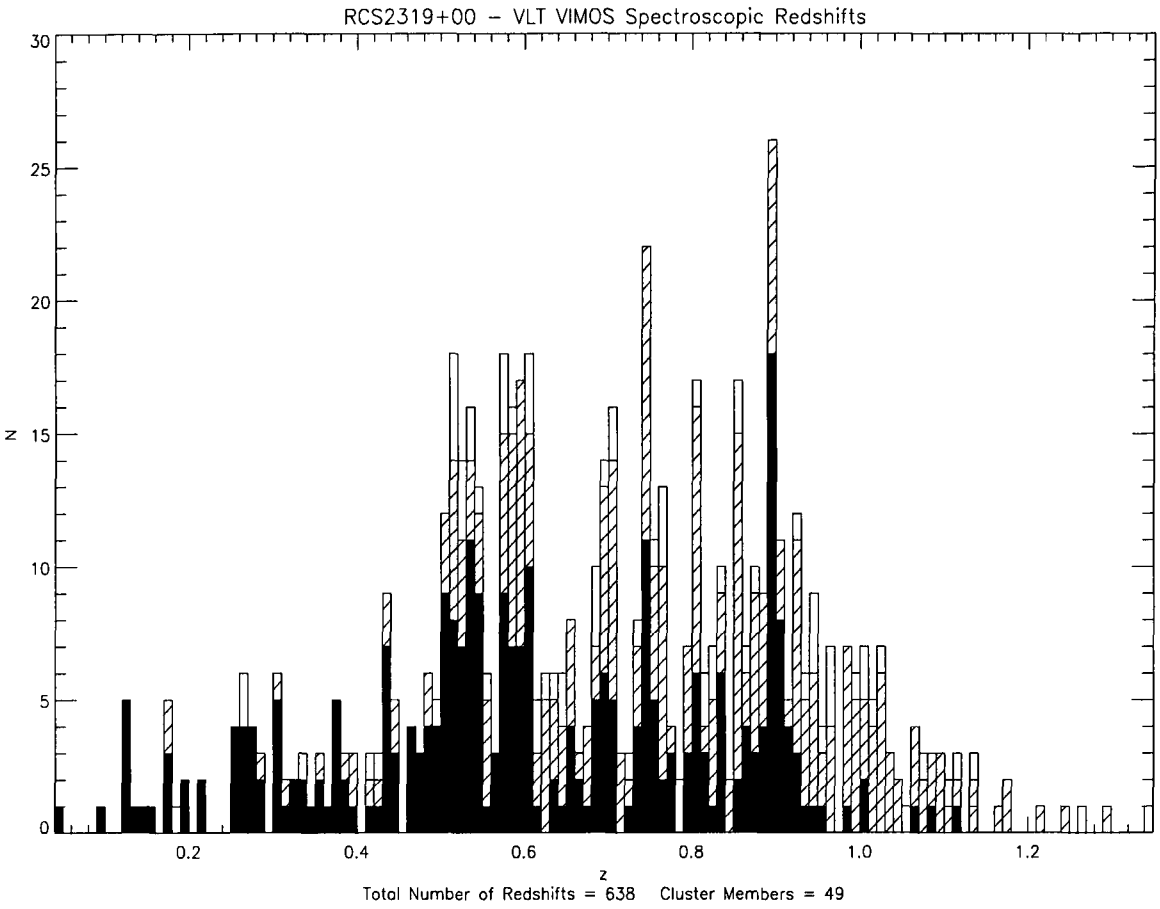

Figure 4.1: Histogram of all spectroscopically identified redshifts for VLT-VIMOS sources in the RCS2319+00 supercluster field. The filled histogram represents confidence 1 redshifts, the hatched histogram represents confidence 1 and 2 redshifts and the open histogram shows redshifts of all confidence levels. Note the spike in redshift number at the supercluster redshift of $z \sim 0.9$.

Histograms of the galaxies within a 1.2 Mpc radius of each cluster center, defined by the red-sequence significance contours, are shown in Figure 4.2 (Gladders and Yee, 2005). This radius was chosen to encompass as many galaxies as possible for each cluster center region without overlapping the regions and causing galaxies to be associated with more than one cluster center (See Section 4.3.3). As mentioned in Section 2.1, the separation of each cluster to its nearest neighbor is < 3 Mpc in the plane of the sky. The radius chosen is somewhat arbitrary and, had there not been a concern with overlapping the component clusters, could have been larger to

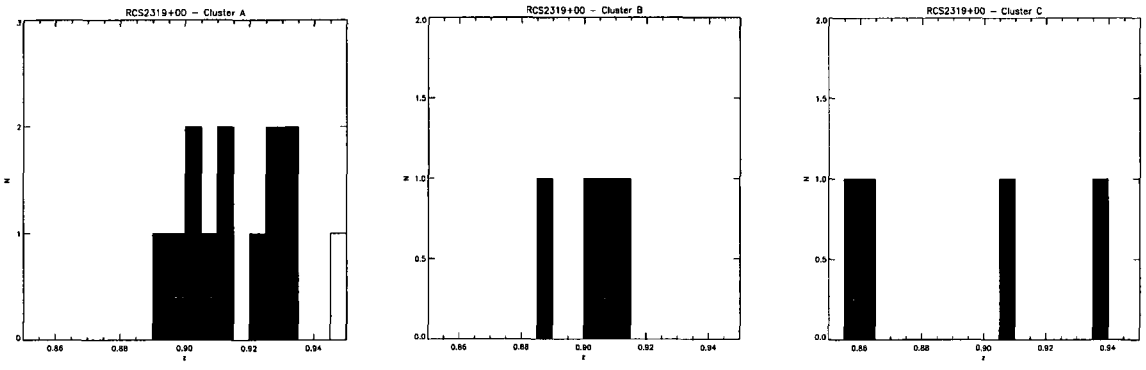

Figure 4.2: Histograms of the redshifts within 1.2 Mpc radius of each cluster center. The solid histograms represents higher confidence redshifts and the open histograms represent confidence 3 redshifts.

maximize the amount of galaxies used to calculate the mean spectroscopic redshift of each component cluster (See Section 4.3.1).

The apparent angular size for a 1.2 Mpc radius was found using the angular diameter distance to the cluster through the relation:

$$\theta = \frac{s}{d_A}. \tag{4.3}$$

In Equation 4.3, θ is the apparent angular size, s is the physical size of the source and d_A is the angular diameter distance, defined as:

$$d_A = \frac{d_L}{(1+z)^2}. \tag{4.4}$$

The luminosity distance to the cluster can be found using the following equation,

$$d_L = \frac{c}{H_o} z \left(1 - \frac{1+q_o}{2} z\right)(1+z), \tag{4.5}$$

where q_o is the deceleration parameter defined as $q_o = \Omega_R + \frac{1}{2}\Omega_M - \Omega_\Lambda$. For the adopted cosmology of a matter dominated universe with $\Omega_M = 0.3$ and $\Omega_\Lambda = 0.7$, q_o has a value of -0.55. Combining Equations 4.5 and 4.4 gives a new equation for the

apparent angular size of a source.

$$\theta = \frac{s}{z}\frac{H_o}{c}\left(1 - \frac{1+q_o}{2}z\right)^{-1}(1+z) \tag{4.6}$$

Using a Hubble constant of $H_o = 70$ km s^{-1} Mpc^{-1}, the apparent angular size of a 1.2 Mpc radius at $z = 0.9$ is 2.55 arcminutes.

4.3 The Combined VIMOS-IMACS Redshift Catalogue

In order to calculate the mean spectroscopic redshifts for each component cluster in the RCS2319+00 supercluster field and their dynamical properties, the results of the visual VIMOS spectroscopic survey were combined with the results from Gilbank et al. (2008) using the 27 arcminute diameter IMACS multi-object spectrograph, which can accommodate 700–900 slits per mask. The total catalogue contains 1051 spectroscopic redshifts of all confidence levels. Figure 4.3 shows the redshift histogram of the spectroscopic redshift identified galaxies of all confidence levels from the combined data set.

4.3.1 Calculation of Component Cluster Redshifts

To calculate the spectroscopic redshift of each of the three component clusters using the combined data from the VIMOS and IMACS spectroscopic surveys, the redshifts within a 1.2 Mpc region of each cluster center were found and those within a redshift range of $0.85 \leq z \leq 0.95$ were plotted in Figure 4.4.

The histograms were inspected to look for prominent outliers not consistent with what would be expected for a Gaussian curve. There is some concern that the smaller peak at redshift $z = 0.93$ in the histogram for cluster A is a separate velocity structure. Inclusion of the cross–correlation identified redshifts (see Section 4.1) and future

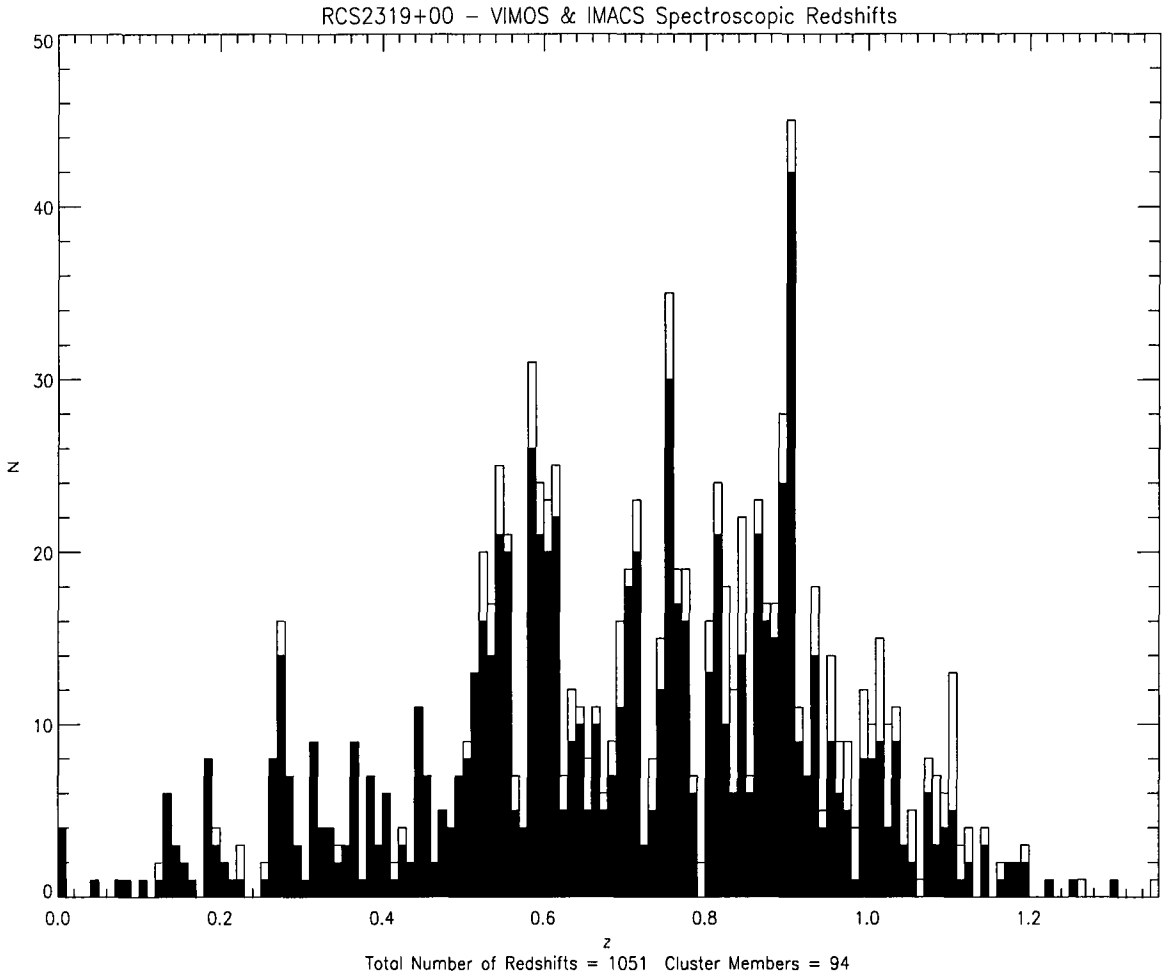

Figure 4.3: Histogram of the combined VIMOS and IMACS spectroscopy in the RCS2319+00 supercluster field. The filled histogram contains redshifts in the higher confidence levels. The open histogram includes all identified redshifts including the lowest confidence levels.

spectroscopic observations may help to bridge the gap between the two peaks. If this is not the case, simulations must be done to determine the probability of obtaining a secondary peak in a Gaussian like system given a reasonable estimate for the cluster velocity dispersion (see Section 4.3.2 for an explanation of the velocity dispersion).

For the current sample, only the two lowest redshift objects from the cluster B and the 2 lowest and the highest redshift object in the cluster C were manually removed from the cluster center regions. Using all other high confidence redshifts, a mean

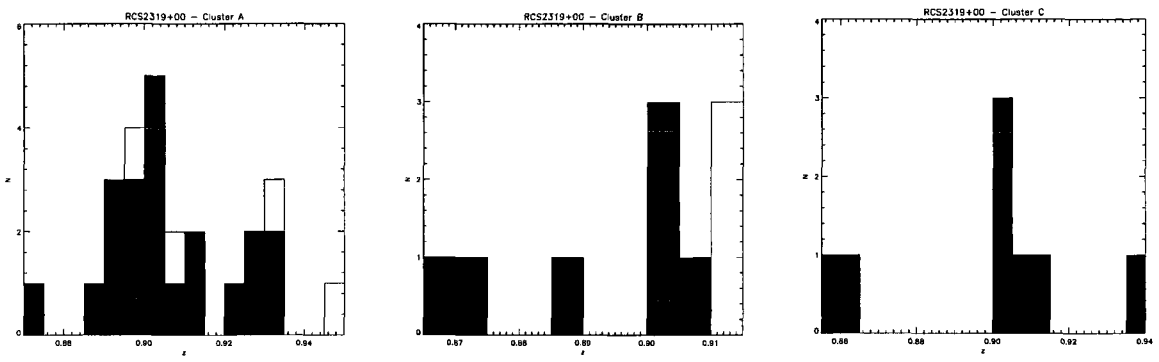

Figure 4.4: Histograms of the redshifts within 1.2 Mpc radius of each cluster center using the combined data from this survey and that done by Gilbank et al. (2008). The solid histograms represents higher confidence redshifts and the open histograms represent lower confidence redshifts.

spectroscopic redshift was determined for each component cluster using a biweight mean calculation.

A biweight mean calculation is a more robust method of calculating the mean of a distribution which may contain non-Gaussian properties. It uses order statistics to rank data sets in ascending order. Weights are then assigned to each data point, x_i, based on their position relative to the median absolute deviation (MAD) from the median of the sample; MAD = median $(x_i - M)$ where M is the median value of the sample. The biweight estimator is defined as:

$$S_{BI} = n^{1/2} \frac{[\sum_{|u_i|<1}(x_i - M)^2(1-u_i^2)^4]^{1/2}}{|\sum_{|u_i|<1}(1-u_i^2)(1-5u_i^2)|}, \tag{4.7}$$

where n is the number of data points in the sample set and $u_i = (x_i - M)/6S_{BI}$ with S_{BI} being the estimate of the mean from the previous iteration. For the first iteration, the MAD is used as the mean estimate. By assigning weights to the data points and using multiple iterations, the biweight estimate of the mean is less susceptive to outlying data points that may otherwise disproportionally shift the value of the mean (Beers et al., 1990).

The biweight spectroscopic mean redshift and deviation was calculated for each of the 1.2 Mpc radius cluster center regions. A redshift range of $\pm$ 3 σ_z was found for each cluster center and the biweight mean redshift was recalculated for redshifts within this range to further reduce the effect of random outlying data points. Table 4.2 outlines the number of VIMOS and IMACS galaxies used to determine the mean spectroscopic redshifts. The spectroscopic redshifts were found to be $z = 0.9056$, 0.9041, and 0.9047 for clusters A, B, and C respectively.

4.3.2 Dynamical Properties of the Component Clusters

With enough spectroscopic members, dynamical properties for each component cluster can be estimated. Due to the fact that galaxy clusters have no known finite boundary, calculation of properties based on an assumed boundary, such as the 1.2 Mpc radius used in this study, carry inherent uncertainties and may only be used as an approximation to the physical and dynamical properties of the galaxy clusters. That being said, the calculation of dynamical properties based on spectroscopic redshifts is an interesting and useful exercise which can help distinguish prominent features of the cluster.

The velocity dispersion can be used further to define a rough cut in redshift of cluster members versus the field population. The velocity dispersion measures the velocity scale of a cluster and can be used to find the approximate virial radius and mass of the cluster. First, the relative radial velocity of each galaxy within the central 1.2 Mpc regions having a redshift within $\pm$ 3 σ_z of the new mean cluster redshifts was calculated using Equation 4.2. Next, any galaxy with a radial velocity of $> \pm$ 3500 km s^{-1} relative to its cluster redshift was discarded. This is done to reduce the effect of outliers on the velocity dispersion calculation since galaxy cluster velocity dispersions are typically $>$ 3500 km s^{-1}, following the method of Swinbank et al. (2007b). The

biweight mean dispersion of the velocities was then calculated for each cluster.

The cluster virial radius can be approximated by calculating the radius at which the overdensity of the cluster is 200 times the critical density (Carlberg et al., 1997). This dynamical estimate for the virial radius is defined as:

$$r_{200} = \frac{\sqrt{3}}{10}\frac{\sigma_\nu}{H(z)}, \tag{4.8}$$

where, for a flat universe, the Hubble constant at the cluster redshift is defined by;

$$H^2(z) = H_o^2[\Omega_M(1+z)^3 + \Omega_\Lambda]. \tag{4.9}$$

The estimated virial radius in Equation 4.8 assumes a density profile of $\rho(r) \propto 1/r^2$ for the cluster density, which is a reasonable estimate but not ideal (Blindert, 2006).

Using the velocity dispersion and the virial radius, the dynamical estimate of the virial mass can be attainted through the relation:

$$M_{200} = \frac{3}{G}\sigma_\nu^2 r_{200}. \tag{4.10}$$

Equation 4.10 is known to overestimate the cluster mass by a factor of $< 50\%$ and should be corrected by a term representing a surface pressure to correct for the finite division delineating the mass boundary. The reason that the mass estimates herein have not been amended is that the surface pressure correction depends on the mass profile of the cluster, which is not known (Blindert, 2006).

Due to a lack of galaxy redshifts within the 1.2 Mpc region of cluster C, no dynamical properties were calculated. The calculated estimates for the σ_ν, r_{200} and M_{200} for cluster B are based on 7 spectroscopic members only and are therefore unreliable but included for comparison with cluster A. It is desirable to have > 10 member galaxies for dynamical calculations. Table 4.2 summarizes the component cluster property

estimates along with their errors. For the spectroscopic mean redshift, z_{spec}, the error is given as the standard deviation of the biweight mean estimate.

The lack of coverage on clusters B and C is due to the fact that the VIMOS masks were designed before these two component clusters had been discovered. As such, the 2 arcminute gaps between quadrants in the VIMOS pointings fall on the center of cluster B and close to the center of cluster C. The IMACS data does cover all three cluster centers, however only one mask was used which reduces the number of sources per area which can be observed due to slit placement. A more recent IMACS observation having three seperate masks has been designed to cover all three component cluster centers and is awaiting redshift analysis.

The error on the velocity dispersion was estimated using a bootstrap mean estimator. Bootstrap estimators are used to assign confidence estimates to the calculated value, in this case the velocity dispersion, σ_ν. It is an iterative function wherein the desired value is estimated numerous times by randomly eliminating data points. The standard deviation of the bootstrap mean values gives an error which is unbiased towards outlying data points since the selection of the data set used to calculate the mean in each iteration is random. The errors on the virial radius and mass were calculated based on standard propagation of errors.

Table 4.2: Summary of dynamical properties of the component clusters in the RCS2319+00 supercluster field based on the combined data from the VIMOS and IMACS spectroscopic surveys. The last two columns represent the number of galaxies in the 1.2 Mpc cluster center regions from each data set used in the calculation of z_{spec} (first number) and σ_{nu} (second number).

Cluster	z_{spec}	σ_ν (km/s)	r_{200} (Mpc)	M_{200} (10^{14} $M_\odot$)	VIMOS (z_{spec} - σ_ν)	IMACS (z_{spec} - σ_ν)
(A) 23:19:53 +00:38:00	0.9056 ± 0.0165	1300 ± 410	1.9 ± 0.6	22.7 ± 10.2	12 - 8	9 - 8
(B) 23:20:02 +00:33:24	0.9041 ± 0.0083	1310 ± 640	1.9 ± 1.0	23.4 ± 16.2	4 - 4	3 - 3
(C) 23:19:48 +00:30:06	0.9047 ± 0.0047	—	—	—	1 - 0	4 - 0

Table 4.2 also indicates the number of higher confidence galaxies from each of the VIMOS and IMACS data sets which were used in the calculations. The first value on

each column indicates the number of spectroscopic members used for the calculation of z_{spec} while the second value indicates how many of these galaxies had relative velocities $< \pm$ 3500 km s^{-1} and were used in calculating the dynamical properties. This highlights the need for more spectroscopic surveys on this supercluster field.

The velocity dispersion calculated for cluster A is consistent within 2σ errors to that found by Gilbank et al. (Gilbank et al., 2008) using the IMACS data only of $\sigma_v = (790 \pm 200)$ km s^{-1}. The mass estimates are high compared to the X-ray masses given in Table 2.1, which is not an unforeseen result do to the overestimation of Equation 4.10. The large velocity dispersion and mass estimates for cluster B may indicate that the sources along the perimeter of the 1.2 Mpc radius in the region closest to cluster A belong instead to cluster A. Disentangling the specific galaxies belonging to each component cluster may be impossible to do for this superstructure due to their proximity in both redshift space and in the plane of the sky.

Upon comparison of the distribution of cluster galaxies within the 1.2 Mpc radius of each cluster between the VIMOS data alone (Figure 4.5) with the combined data set (Figure 4.6) it can be seen that the IMACS data adds coverage of the very central region of the clusters with VIMOS data adding members from the outer perimeter of the central 1.2 Mpc regions. More spectroscopic coverage in each cluster center region results in better population of the redshift histograms, which helps in the determination of cluster redshift and membership.

4.3.3 RCS2319+00 Superstructure Members

The determination of a redshift range within which to accept cluster membership is a difficult and somewhat arbitrary task. Galaxy clusters and superclusters are complex dynamical systems which cannot be fit by simple Gaussian distributions. The effect of infalling galaxies from the field and the underlying large scale structure of the system

complicate the calculations (Carlberg et al., 1996). Even so, a rough cut in redshift range can be determined based on the velocity dispersion of the cluster. In the case of the RCS2319+00 supercluster structure, the radial velocity of cluster A, which appears to be the most massive of the three component clusters and the only one for which a reasonably reliable velocity dispersion is available, is used to determine the cluster redshift range.

Using the Gaussian curve, an estimate for the cluster membership range is found to be $\Delta\nu = \pm 3000$ km s^{-1}. This velocity range corresponds to a redshift range of $0.8857 \leq z \leq 0.9239$. The velocity range is not accepted out to the tails of the Gaussian in order to avoid accepting galaxies belonging to the average background field galaxy population.

The sky distribution of galaxies from the VIMOS survey is shown in Figure 4.5. It includes redshifts of all confidence levels. The square data points represent radio galaxies, with filled squares indicating radio galaxies which have been spectroscopically confirmed to lie within the cluster redshift range. The filled circles symbolize optical galaxies with spectroscopic redshifts consistent with the RCS2319+00 superstructure. The crosses have been identified as foreground and background optical sources. The large open circles are centered on the three component clusters and trace a 1.2 Mpc radius around each cluster center. The RCS significance map for this cluster field, measured by Gladders and Yee (2005), has been overplotted on the distribution. There is a lack of galaxies within the central regions of clusters B and C. This is due to the fact that their positions were unknown at the time of the spectroscopic mask design and in fact lie in or very near the gaps in the VIMOS instrument quadrants.

Of the 638 redshifts determined from the VLT VIMOS data on the RCS2319+00 cluster field, 49 were classified as cluster members. Appendix A contains a list of all

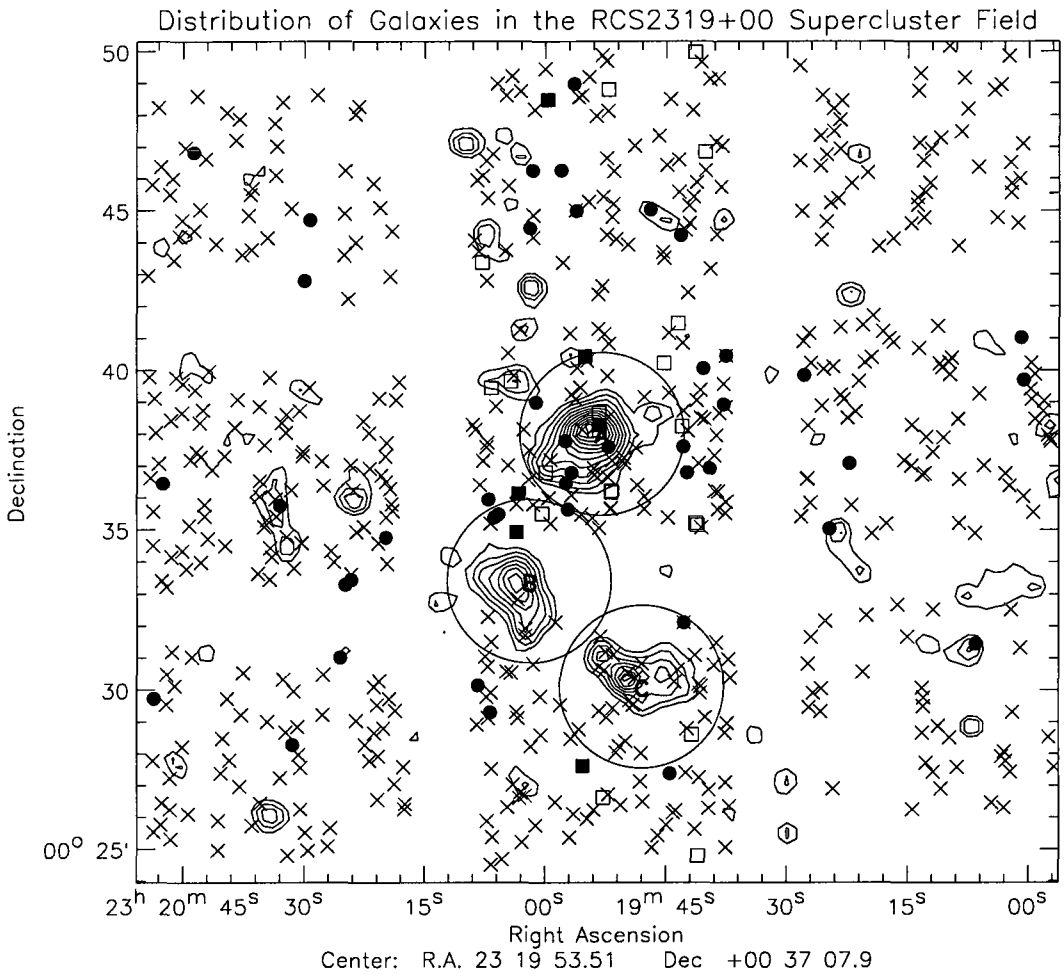

Figure 4.5: Distribution of galaxies from the VLT–VIMOS spectroscopic survey of RCS2319+00. Solid symbols indicate cluster member galaxies; squares are radio sources and circles are optical sources. The open squares represent field radio galaxies while the crosses symbolize optical field galaxies. The 1.2 Mpc regions around the three component cluster centers are shown along with the red-sequence significance contours.

galaxies identified as cluster members as well as a list of all other redshift identified galaxies in this survey.

Figure 4.6 shows the sky distribution of all spectroscopically identified galaxies in the RCS2319+00 supercluster field from the combined data of the VIMOS and IMACS surveys. The combined data set includes 1051 spectroscopic redshifts with 94 identified as belonging to the supercluster structure.

It can be seen in the sky distribution plots that we are beginning to trace out

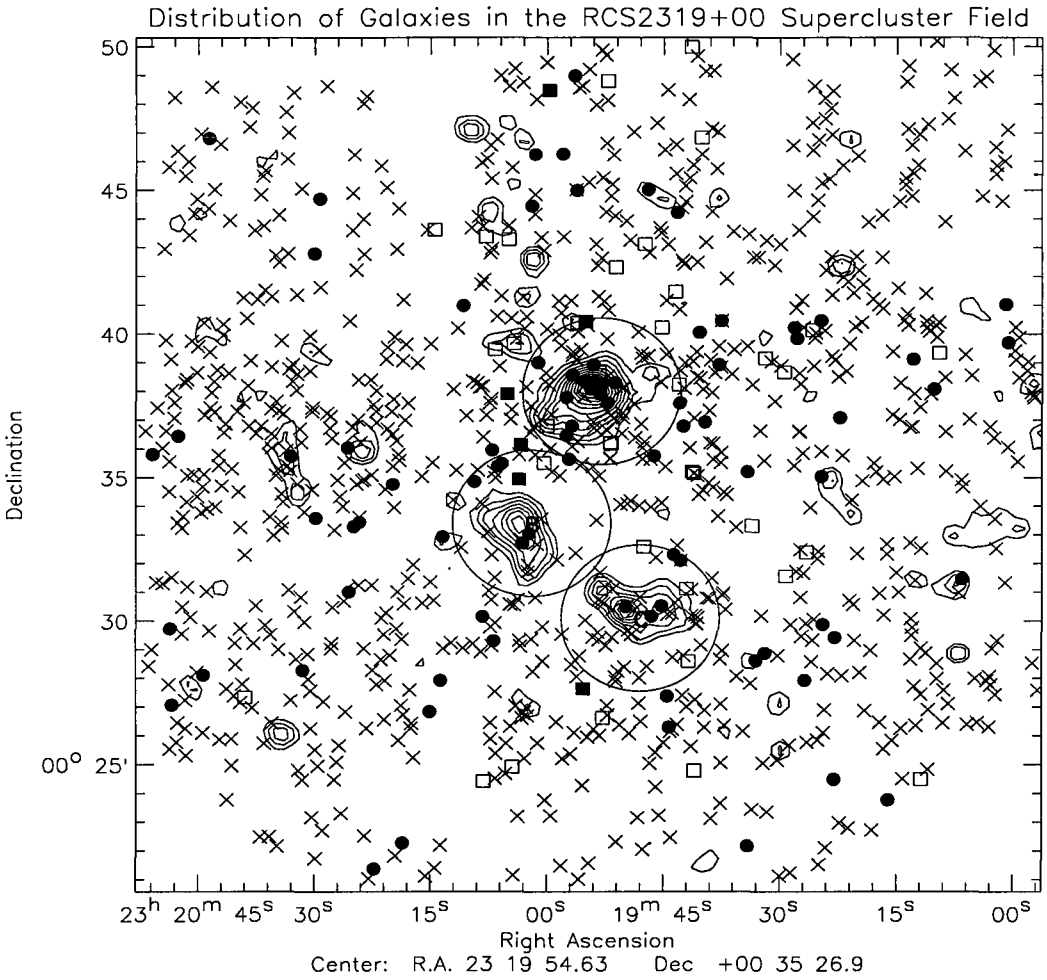

Figure 4.6: Distribution of galaxies from the VIMOS and IMACS spectroscopic survey of RCS2319+00. The symbols used are the same as those in Figure 4.5. Of the 1051 redshifts identified in the two surveys, 131 lie within the cluster redshift range.

structures in the RCS2319+00 supercluster field. Clusters A and B seem to be closely interacting, with a number of cluster members bridging the two cluster regions.

4.4 The Radio Population Spectra

Spectroscopy for the optical counterparts to the 1.4 GHz radio detections in the RCS2319+00 cluster field yielded 27 redshift identifications of all confidence levels, 23 of which have confidence levels of 1 or 2. In the original 6 × 6 arcminute area

around the central region of cluster A with known radio sources, 18 sources of the original 32 were identified, including the interesting possible head-tail source (see Section 4.5). Appendix C contains plots of the 1D spectra of all of the redshift identified radio sources.

Upon cross-comparison of the ra/dec coordinates of the redshift identified sources with a new, priliminary VLA radio source list identified after the VLT-VIMOS spectroscopy run, nine new radio galaxies were added to the list of redshift identified radio sources. The limiting distance for a positive match was set to be < 2 arcseconds. Table 4.3 summarizes the number of redshift identifications for each confidence level and includes, for each confidence level, the number of cluster radio galaxies identified. The confidence levels for the IMACS data were divided into four levels with 1 being the most confident, confidence 2 and 3 are fairly confident (equivalent to confidence level 2 for the VIMOS data) and confidence 4 is tentative (equivalent to level 3 confidence redshifts in the VIMOS spectra).

Table 4.3: Number of radio galaxy redshift identifications by confidence level. The original and new radio source counts are for the VIMOS data. The IMACS radio sources are all found in the new radio source list.

Confidence Level	1	2	3	Total
Original Radio Sources	10	5	3	18
New Radio Sources	5	3	1	9
VIMOS Cluster Members	5	1	0	6
IMACS Radio Sources	10	5	5	20
IMACS Cluster Members	0	1	0	1

Six of the redshift identified radio galaxies, all with confidence levels of 1 and 2, had extractable information in more that one mask. The radio sources identified as 126 and 644 both had usable coverage in three slits with total integration times of 7300 seconds each. The other four sources, 126, 545, 539, and 675, each had two masks with extractable amounts of continuum and integration times totaling 5000 seconds for the first two and 5300 seconds for the latter two sources. For each case of

multiple detections, all spectra for the object were coadded as explained in Section 4.1. Table 4.4 shows all radio galaxies with identified redshifts and the most prominent emission and absorption lines used for the identification. The magnitude R given corresponds to the R-band magnitude of the optical counterparts to the radio sources which were observed.

Table 4.4: Summary of the radio galaxy redshift identifications. * Signifies the extended radio source. Bold entries identify cluster members. See Section 4.5 for further details.

Object	RA	DEC	z	Confidence Level	Emission/Absorprion Lines Identified (Å)	R_{mag}
2	23:19:53.3	+00:38:05.4	0.6896	3	[OII]	24.00
19	23:19:43.5	+00:41:26.1	0.6093	1	[OII]-H&K	21.44
126	**23:19:55.0**	**+00:40:24.4**	**0.9017**	**1**	**[OII]-[NeIII]-[SII]**	**23.40**
142	23:19:45.2	+00:40:15.8	0.9973	2	[OII]	23.39
197	23:20:04.3	+00:39:39.2	0.8795	2	[OII]	282.86
214	23:20:06.6	+00:39:25.1	0.9713	3	[OII]	24.47
292	23:19:53.3	+00:38:38.0	0.7002	1	[OII]-[OIII]	23.29
325	23:19:43.0	+00:38:12.9	0.5275	1	[OII]-H&K	21.23
479	23:19:59.9	+00:36:48.0	0.5978	1	[OII]-[OIII]	21.87
539	23:19:51.8	+00:36:09.5	0.9316	1	[OII]	24.37
542	23:19:51.9	+00:36:13.4	0.9458	3	[OII]	22.43
545	**23:20:03.2**	**+00:36:08.5**	**0.9101**	**1**	**[OII]-HeII**	**22.59**
616	350.0012875	0.591747222	0.554	1	[OII]-H_β-[OIII]	171.62
644	23:19:41.3	+00:35:13.3	0.8124	1	[OII]-[OIII]	22.97
648	23:19:41.1	+00:35:11.7	0.8103	2	[OII]	22.43
675	**23:20:03.5**	**+00:34:56.4**	**0.9115**	**1**	**[OII]**	**23.66**
***600539**	**23:19:53.3**	**+00:38:16.6**	**0.9051**	**1**	**H&K**	**22.73**
603173	23:19:40.2	+00:46:50.4	0.8591	2	[OII]	23.63
603753	23:19:52.2	+00:48:47.8	0.9662	2	[OII]	22.49
604075	23:19:41.4	+00:49:56.9	0.5441	2	[OII]	23.46
701776	23:20:07.9	+00:43:22.0	0.4818	1	H_β-[OIII]	22.24
703199	**23:19:59.5**	**+00:48:28.6**	**0.9005**	**1**	**[OII]**	**22.22**
9010699	23:19:41.8	+00:28:34.9	0.5103	1	[OII]-[OIII]	22.85
9010933	**23:19:55.3**	**+00:27:37.6**	**0.9056**	**2**	**[OII]**	**23.34**
9011166	23:19:52.8	+00:26:37.2	0.6089	1	H&K-H_γ	20.38
9011555	23:19:41.1	+00:24:47.1	0.6225	2	[OII]	21.84

A cross-comparison of the source positions from new radio source list with the positions of the redshift identified optical sources from the IMACS data of Gilbank et al. (2008) added twenty new radio sources to the known spectroscopically confirmed radio population. One of these new radio sources lies within the redshift range of the supercluster at $z = 0.8961$, bringing the current known cluster radio population in

the RCS2319+00 supercluster to a total of seven.

4.5 The Extended Radio Source

The targeted sources in the RCS2319+00 supercluster field included an interesting radio source which is possibly a head tail source. Head tail sources are found mainly within galaxy clusters and consist of an AGN with radio jets whose shape is progressively bent as the galaxy moves through the ICM. It is theorized that the direction and amount of bending in the radio jets could be used to discern information regarding the motion of the galaxy within the cluster, which otherwise is unavailable with normal galaxy sources for whom no tangential velocity information is available (Bodo et al., 1981).

The headtail source detected in the RCS2319+00 superstructure is located at 23:19:53.31, +00:38:16.63 with an R-band magnitude of 22.73 mag. Figure 4.7 shows the radio image of this intriguing source. Due to the interesting nature of this extended radio source, it was observed in two masks, P1Q1 and P4Q4, for a total integration time of 5380 seconds.

No emission lines are present in either the 2D or 1D spectra so redshift identification was done through examination of the coadded 1D spectra for absorption lines. Based on the shape of the 1D spectra, the Ca H&K absorption lines were identified at $\sim$ 7497 Å and $\sim$ 7558 Å in the observed frame giving a redshift of $z = 0.9051$, which falls within the cluster. The coadded 1D spectra is shown in Figure 4.8 with the common emission and absorption lines overlaid on the plot. The Balmer break absorption is visible, with the A–band Fraunhofer line directly to the right. As well, there is possible G_{band} and H_γ absorption at $\sim$ 8176 Å and $\sim$ 8221 Å in the observed frame. A run through the correlation program confirmed that this extended radio source is in fact a cluster member allowing for an increase in the confidence level

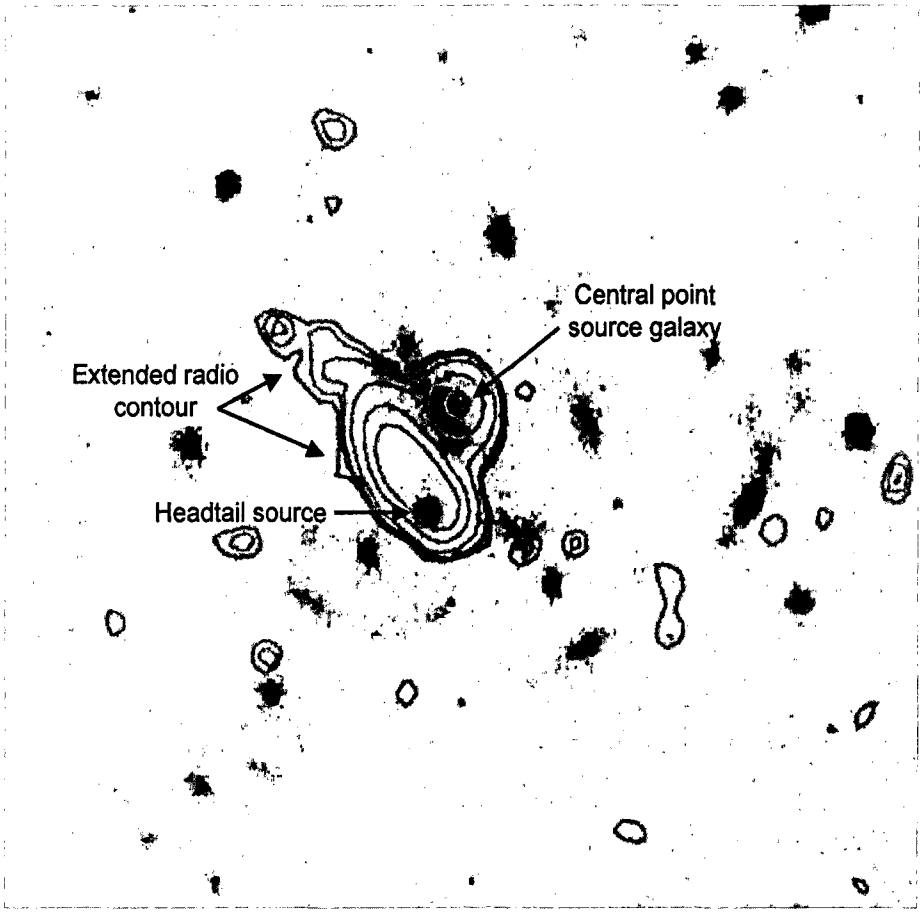

Figure 4.7: K-band optical image with radio contours. The top right bulge of the large radio contour belongs to the radio counterpart of the central point source galaxy of the cluster while the elongated section corresponds the the headtail source, whose optical counterpart in located in the bottom section of the contour.

determination to a confidence 1 redshift. The shape of the 1D spectra is consistent with that of an old elliptical galaxy (Kinney et al., 1996).

4.6 SCUBA Submillimeter Sources

Slits were placed on two optical counterparts to the 1.4 GHz radio detections of SCUBA 850 μm submillimeter sources. The information regarding the sources is summarized in Table 4.5. Careful inspection was done on each of the 2D spectra for both sources on each of the data sets but no continuum was visible. A program

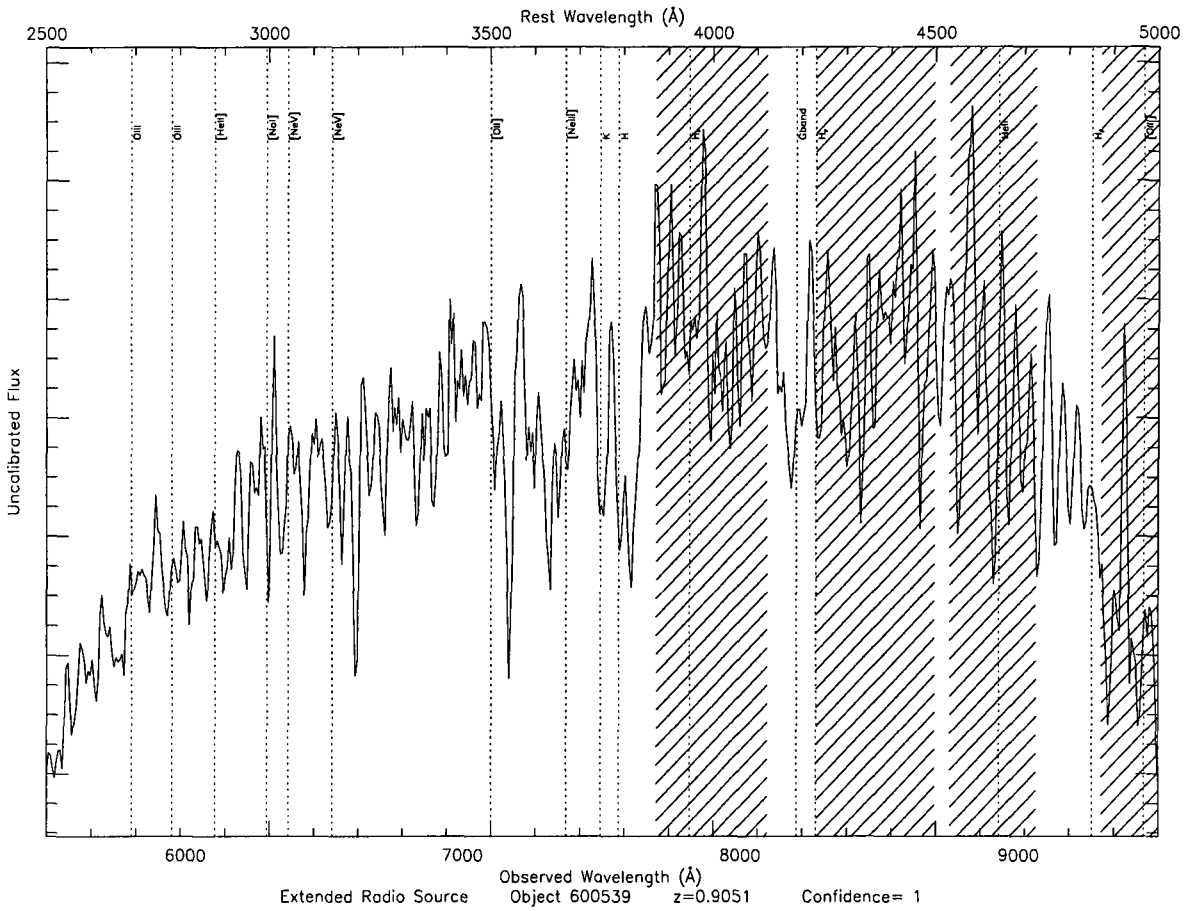

Figure 4.8: Plot of the 1D spectra of the extended radio source with common emission and absorption lines overlaid at the identified redshift.

was then written in IDL (Interactive Data Language) to extract apertures of varying widths from within the centers of the slits and coadd all of the 2D slices for each source. These coadded 2D slices were traced in IRAF in the same manner as described in Section 3.4.

Table 4.5: Summary of the observations of the two SCUBA 850 μm submillimeter sources.

Radio ID	RA	DEC	R_{mag}	Masks	Integration Time (s)
356	23:19:49.7	+00:37:59.2	89.57	P1Q1 P2Q2 P3Q3 P4Q4	9800
410	23:19:56.8	+00:37:22.3	53.06	P1Q1 P2Q2 P4Q4	7880

Unfortunately, no reasonable trace could be performed which resulted in any emission above the noise of the observations. The hope was that even if no continuum

could be readily identified, emission lines would be present which could be used to identify the redshifts of the SCUBA sources. The 2D and 1D coadded spectra for each SCUBA source were investigated at 7100 Å, the expected observed wavelength for [OII] 3727 Å for a source at $z \sim 0.905$, but no emission was detected even upon close examination.

The lack of redshift measurements does not mean that these submm sources can not be at the cluster redshift, simply that there is not enough emission in the optical to obtain accurate spectroscopy for these objects. This is not an unexpected problem. Simpson et al. (2004) outlined the difficulties in spectroscopic observations of submm sources, one of the main ones being that the optical counterparts to these dusty sources are often very faint and therefore it is extremely difficult to obtain sufficient S/N to identify emission lines. They suggest that very sensitive, near-infrared spectroscopy may be the key to identifying the redshifts of these sources.

Chapter 5

Summary and Future Work

5.1 The Spectroscopic Survey of the RCS2319+00 Supercluster

The VLT–VIMOS spectroscopic survey of the RCS2319+00 supercluster field yielded a total of 638 new visually identified galaxy redshifts from a sample of 1134 targets. Combining the VIMOS data with the IMACS data from Gilbank et al. (2008), results in a total of 1051 redshift identified galaxies in the supercluster field over the $\sim 30 \times 30$ arcminute area surveyed.

Using the combined data set, new mean spectroscopic redshifts were calculated from the central 1.2 Mpc regions around each of the three component clusters producing measurements of $z_{spec} = 0.9056$, 0.9041, and 0.9047 for clusters A, B, and C respectively. The 1.2 Mpc region surrounding cluster A contained 21 high confidence redshift identified galaxies within $0.85 \leq z \leq 0.95$; 12 from the VIMOS data and 9 from the IMACS data. These were used to calculate a new velocity dispersion of $\sigma_\nu = (1300 \pm 410)$ km s^{-1} for the cluster. This value was used to approximate a virial radius of $r_{200} = (1.9 \pm 0.6)$ Mpc and a virial mass of $M_{200} = (22.7 \pm 10.2)\ 10^{14}$ M$_\odot$ for cluster A. While subject to selection errors and overestimation of M_{200} by a factor of $< 50\%$, these results reiterate the dominance of cluster A in this supercluster field and are consistent with the red-sequence significance contours of each component cluster.

Using the new velocity dispersion for cluster A, a supercluster membership range of $\leq \pm 3000$ km s^{-1} relative to the mean spectroscopic redshift was established in velocity space. This translates to a supercluster membership range in redshift space

of $0.8857 \leq z \leq 0.9239$, within which 94 of the 1051 redshift identified galaxies reside; 49 from the VIMOS data and 45 from the IMACS data. The spatial distribution of cluster members in the combined data set shows evidence of underlying structure in the supercluster field, especially between component clusters A and B.

The 94 cluster galaxies include seven known radio sources, six of which were identified using the VIMOS spectroscopic data. While not a large sample, the properties of these radio galaxies can now be studied with knowledge of their position in redshift space in addition to their spatial position within the supercluster field and their relative distances to the component cluster centers.

Though no redshifts were identified for the two submm SCUBA sources in the VIMOS sample, their possible cluster membership has not yet been ruled out. Sensitive near-infrared spectroscopy of these sources may be able to probe the strong H_α emission line at 6563 Å, which is a strong tracer of star formation.

5.2 Future Work

The future work slated for the spectroscopic survey of the RCS2319+00 supercluster includes the expected addition of $\sim$ 80 redshift identifications to the catalogue from the cross-correlation program currently being run by Erica Ellingson. With the additional data it is hoped that additional cluster members will emerge and aid in refining the mean spectroscopic redshifts for each component cluster and the subsequent calculation of dynamical properties. The addition of even a few members within the central regions of the component clusters could greatly improve the measurement of cluster properties.

Further investigation of the possible secondary, higher redshift population in the central region of cluster A is necessary. Should the additional data from the correlation program not add any members which aid in filling the gap between the two

redshift peaks, Monte Carlo simulations of the probability of finding a secondary clump in a galaxy cluster distribution can be run. This secondary peak may simply be an effect of the small radius needed to define regions around each cluster center without overlap.

Ideally, more spectroscopy of the central regions of each cluster is needed to increase the known population of all three cluster centers to better distinguish between true cluster members and coincident, high redshift background galaxies and to improve the estimates of dynamical properties. While the data from the VIMOS spectroscopic survey contained in this thesis doubles the number of known cluster members in the RCS2319+00 supercluster field and refines the estimates for the spectroscopic redshifts of each component cluster, the 94 cluster members still represent a small population over this large structure.

The VLA radio map used to create the preliminary list of radio sources in the broader supercluster field (i.e. outside of the original 6 x 6 arcminute region around cluster A) is currently being analyzed in more detail by a collaborator. The new radio source list is expected to reach a deeper flux limit. Once it is available the new radio source list will again be cross referenced with the redshift catalogue to help pinpoint the radio population in redshift space. The redshift identified radio sources in the spectroscopic catalogue may then be stacked by shape (i.e. by galaxy type) to create templates of high redshift radio galaxy spectra in clusters. By stacking the spectra, better S/N can be achieved which may reveal additional spectroscopic features. Additional radio spectra would aid in this endeavor.

The most active evolutionary phases of starburst and AGN galaxies are likely dust enshrouded, making them difficult to detect at the optical wavelengths but luminous in the IR where the heated dust thermally reemits energy. A new catalogue of 24 μm sources from the MIPS camera (Multiband Imaging Photometer for Spitzer) and mid-

infrared sources from the IRAC instrument (Infrared Array Camera) on the Spitzer Space Telescope is being compiled by our group on a subset of 48 massive galaxy clusters in the RCS1 survey sample. This galaxy cluster sample, which includes cluster A of the RCS2319+00 supercluster, covers a broad redshift range of $0.3 < z < 1.1$. The flux depth of these data is lower than that of submm but comparable to radio source flux. Data for a secondary survey of the three component clusters in the RCS2319+00 is currently being taken by Spitzer and, once analyzed, is hoped to add a large number of infrared detected sources to the central regions of the three clusters.

The sources in this infrared catalogue belonging to the RCS2319+00 supercluster field will be cross referenced with the combined VIMOS–IMACS spectroscopic catalogue in the hopes of positively identifying some of these active galaxies as cluster members. Any redshift identifications of optical counterparts to infrared sources will aid in justifying a planned large scale spectroscopic survey of the infrared sources in the sample of 48 galaxy clusters, in which RCS2319+00 will be prominently featured. This large scale spectroscopic survey will build on the methods used in this thesis to produce a comprehensive catalogue of redshift identified infrared sources in galaxy clusters with the objective of increasing cluster membership in the important central regions around each cluster.

In summary, additional spectroscopic data on this supercluster is needed to aid in tracing the structure of the supercluster field in redshift space and to better understand the galaxy populations in the RCS2319+00 cluster field. With the addition of more redshift identified radio and infrared sources, studies on the spatial distribution of active starburst and AGN populations within the superstructure can be undertaken. Additional cluster members in the regions between the three cluster centers will aid in determining their dynamical properties and the way in which they are interacting within the larger supercluster.

Bibliography

Abell, G. O. *Astrophys. J., Suppl. Ser.*, 3:211, 1958.

Abell, G. O., Corwin, H. G., Jr., and Olowin, R. P. *Astrophys. J., Suppl. Ser.*, 70:1, 1989.

Baade, W. and Minkowski, R. *Astrophys. J.*, 119:215, 1954.

Bahcall, N. A. *Ann. Rev. Astron. Astrophys.*, 26:631, 1988.

Balogh, M. L., Morris, S. L., Yee, H. K. C., Carlberg, R. G., and Ellingson, E. *Astrophys. J., Lett.*, 488:L75, 1997.

Beers, T. C., Flynn, K., and Gebhardt, K. 100:32, 1990.

Bekki, K. and Couch, W. J. *Astrophys. J., Lett.*, 596:L13, 2003.

Best, P. N. *Mon. Not. R. Astron. Soc.*, 336:1293, 2002.

Best, P. N., Kauffman, G., Feckman, T. M., Brinchmann, J., Charlot, S., Ivezíc, u., and White, S. D. M. *Mon. Not. R. Astron. Soc.*, 362:25, 2005.

Binggeli, B. *Astron. Astrophys.*, 107:338, 1982.

Binney, J. and Tremaine, S. *Galactic dynamics.* Princeton University Press: Princeton, NJ, 1994.

Blindert, K. *Internal dynamics of galaxy clusters in the Red-Sequence Cluster Survey.* Ph.D. thesis, University of Toronto (Canada), 2006.

Bode, P. and Ostriker, J. P. *Astrophys. J., Suppl. Ser.*, 145:1, 2003.

Bodo, G., Ferrari, A., and Massaglia, S. *Mon. Not. R. Astron. Soc.*, 196:481, 1981.

Bower, R. G., Lucey, J. R., and Ellis, R. S. *Mon. Not. R. Astron. Soc.*, 254:601, 1992.

Burbidge, E. M., Galianni, P., Arp, H., Junkkarinen, V., Burbidge, G., and Zibetti, S. In *Bulletin of the American Astronomical Society*, volume 36, page 1396. 2004.

Carlberg, R. G., Yee, H. K. C., Ellingson, E., Abraham, R., Gravel, P., Morris, S., and Pritchet, C. J. *Astrophys. J.*, 462:32, 1996.

Carlberg, R. G., Yee, H. K. C., Ellingson, E., Morris, S. L., Abraham, R., Gravel, P., Pritchet, C. J., Smecker-Hane, T., Hartwick, F. D. A., Hesser, J. E., Hutchings, J. B., and Oke, J. B. *Astrophys. J., Lett.*, 485:L13, 1997.

Condon, J. J. *Ann. Rev. Astron. Astrophys.*, 30:575, 1992.

Danese, L., de Zotti, G., and di Tullio, G. *Astron. Astrophys.*, 82:322, 1980.

Dressler, A., Thompson, I. B., and Shectman, S. A. *Astrophys. J.*, 288:481, 1985.

Dubinski, J. *Astrophys. J.*, 502:141, 1998.

Ellingson, E., Lin, H., Yee, H. K. C., and Carlberg, R. G. *Astrophys. J.*, 547:609, 2001.

ESO VIMOS Pipeline Team. *Very Large Telescope VIMOS Pipeline User Manual: Issue 4.0.* ESO, 2008. D-85748 Garching bei München.

European Southern Observatory. ESO - Paranal Instrumentation: VIMOS, http://http://www.eso.org/sci/facilities/paranal/instruments/vimos/. 2008.

Evrard, A. E., MacFarland, T. J., Couchman, H. M. P., Colberg, J. M., Yoshida, N., White, S. D. M., Jenkins, A., Frenk, C. S., Pearce, F. R., Peacock, J. A., and

Thomas, P. A. *Astrophys. J.*, 573:7, 2002.

Fabian, A. C., Mushotzky, R. F., Nulsen, R. E. J., and Peterson, J. R. *Mon. Not. R. Astron. Soc.*, 321:L20, 2001.

Gilbank, D. G., Yee, H. K. C., Ellingson, E., Gladders, M. D., Barrientos, L. F., and Blindert, K. *Astrophys. J.*, 134:282, 2007.

Gilbank, D. G., Yee, H. K. C., Ellingson, E., Hicks, A. K., Gladders, M. D., Barrientos, L. F., and Keeney, B. *Astrophys. J., Lett.*, 677:L89, 2008.

Gisler, G. R. *Mon. Not. R. Astron. Soc.*, 183:633, 1978.

Giuffrida, G. and Marconi, G. *Very Large Telescope Paranal Science Operations VIMOS data reduction cookbook.* ESO, 2007. D-85748 Garching bei München.

Gladders, M. D., Hoekstra, H., Yee, H. K. C., Hall, P. B., and Barrientos, L. F. *Astrophys. J.*, 593:48, 2003.

Gladders, M. D. and Yee, H. K. C. *Astrophys. J.*, 120:2148, 2000.

Gladders, M. D. and Yee, H. K. C. *Astrophys. J., Suppl. Ser.*, 157:1, 2005.

Gladders, M. D., Yee, H. K. C., Majumdar, S., Barrientos, L. F., Hoekstra, H., Hall, P. B., and Infante, L. *Astrophys. J.*, 655:128, 2007.

Grandi, S. A. and Osterbrock, D. E. *Astrophys. J.*, 220:783, 1978.

Hicks, A. K., Ellingson, E., Bautz, M., Cain, B., Gilbank, D. G., Gladders, M. G., Hoekstra, H., Yee, H. K. C., and Garmire, G. *Astrophys. J.*, 680:1022, 2008.

Jenkins, F. A. and White, H. E. *Fundamentals of optics.* New York: McGraw-Hill, 3rd ed., 1957.

Jones, C., Forman, W., Vikhlinin, A., Markevitch, M., Machacek, M., and Churazov, E. In *Lecture Notes in Physics: A Pan-Chromatic View of Clusters of Galaxies and the Large-Scale Structure*, volume 740, pages 31–69. 2008.

Kauffmann, G., Colberg, J. M., Diaferio, A., and White, S. D. M. *Mon. Not. R. Astron. Soc.*, 307:529, 1999.

Kauffmann, G., Heckman, T. M., White, S. D. M., Charlot, S., Tremonti, C., Brinchmann, J., Bruzual, G., Peng, E. W., Seibert, M., Bernardi, M., Blanton, M., Brinkmann, J., Castander, F., Csábai, I., Fukugita, M., Ivezic, Z., Munn, J. A., Nichol, R. C., Padmanabhan, N., Thakar, A. R., Weinberg, D. H., and York, D. *Mon. Not. R. Astron. Soc.*, 341:33, 2003.

Kennicutt, R. C., Jr. *Ann. Rev. Astron. Astrophys.*, 36:189, 1998.

Kinney, A. L., Calzetti, D., Bohlin, R. C., McQuade, K., Storchi-Bergmann, T., and Schmitt, H. R. *Astrophys. J.*, 467:38, 1996.

Le Borgne, D., Abraham, R., Daniel, K., McCarthy, P. J., Glazebrook, K., Savaglio, S., Crampton, D., Juneau, S., Carlberg, R. G., Chen, H.-W., Marzke, R. O., Roth, K., Jørgensen, I., and Murowinski, R. *Astrophys. J.*, 642, 2006.

Le Févre, O., Saisse, M., Mancini, D., Brau-Nogue, S., Caputi, O., Castinel, L., D'Odorico, S., Garilli, B., Kissler-Patig, M., Lucuix, C., Mancini, G., Pauget, A., Sciarretta, G., Scodeggio, M., Tresse, L., and Vettolani, G. In *Proceedings of the SPIE: Instrument Design and Performance for Optical/Infrared Ground-based Telescopes. Iye, Masanori; Moorwood, Alan F. M. Eds.*, volume 4841, pages 1670–1681. 2003.

Le Févre, O., Saisse, M., Mancini, D., Vettolani, G. P., Maccagni, D., Picat, J. P., Mellier, Y., Mazure, A., Cuby, J. G., Delabre, B., Garilli, B., Hill, L., Prieto, E., Voet, C., Arnold, L., Brau-Nogue, S., Cascone, E., Conconi, P., Finger, G., Huster, G., Laloge, A., Lucuix, C., Mattaini, E., Schipani, P., Waultier, G., Zerbi, F. M., Avila, G., Beletic, J. W., D'Odorico, S., Moorwood, A. F., Monnet, G. J., and Reyes Moreno, J. In *Proceedings of the SPIE: Optical and IR Telescope Instrumentation and Detectors, Masanori Iye; Alan F. Moorwood; Eds.*, volume 4008, pages 546–557. 2000.

Le Fèvre, O. and the VIRMOS consortium. *VIMOS User's Manual.* ESO, 2004. D-85748 Garching bei München.

Ledlow, M. J. and Owen, F. N. *Astron. J.*, 109:853, 1995.

Lin, Y.-T. and Mohr, J. J. *Astrophys. J., Suppl. Ser.*, 170:71, 2007.

Lubin, L. M., Brunner, R., Metzger, M. R., Postman, M., and Oke, J. B. *Astrophys. J.*, 531:L5, 2000.

Lubin, L. M., Mulchaey, J. S., and Postman, M. *Astrophys. J.*, 601:L9, 2004.

McNamera, B. R., Nulsen, P. E. J., Wise, M. W., Rafferty, D. A., Carilli, C., Sarazin, C. L., and Blanton, E. L. *Nature*, 433:45, 2005.

Metcalfe, L., Fadda, D., and Biviano, A. *Space Sci. Rev.*, 119:425, 2005.

Miller, N. A. and Owen, F. N. *Astrophys. J., Suppl. Ser.*, 134:355, 2001.

Osterbrock, D. E. *Astrophys. J.*, 132:325, 1960.

Osterbrock, D. E., Koski, A. T., and Phillips, M. M. *Astrophys. J., Lett.*, 197:L41, 1975.

Osterbrock, D. E., Koski, A. T., and Phillips, M. M. *Astrophys. J., Lett.*, 206:898, 1976.

Peacock, J. A. *Cosmological Physics.* Cambridge University Press: Cambridge, UK, 1999.

Poggianti, B. M. and Barbaro, G. *Astron. Astrophys.*, 325:1025, 1997.

Poggianti, B. M., Smail, I., Dressler, A., Couch, W. J., Barger, A. J., Butcher, H., Ellis, R. S., and Oemler, A. J. *Astrophys. J.*, 518:576, 1999.

Ryden, B. *Introduction to cosmology.* Addison Wesley: San Francisco, CA, USA, 2003.

Sandage, A., Binggeli, B., and Tammann, G. A. *Astrophys. J.*, 90:1759, 1985.

Schade, D., Barrientos, L. F., and Lopez-Cruz, O. *Astrophys. J., Lett.*, 477:L17, 1997.

Simpson, C., Dunlop, J. S., Eales, S. A., Ivison, R. J., Scott, S. E., Lilly, S. J., and Webb, T. M. A. *Mon. Not. R. Astron. Soc.*, 353:179, 2004.

Smail, I., Morrison, G., Gray, M. E., Owen, F. N., Ivison, R. J., Kneib, J.-P., and Ellis, R. S. *Astrophys. J.*, 525:609, 1999.

Spergel, D. N., Bean, R., Doré, O., Nolta, M. R., Bennett, C. L., Dunkley, J., Hinshaw, G., Jarosik, N., Komatsu, E., Page, L., Peiris, H. V., Verde, L., Halpern, M., Hill, R. S., Kogut, A., Limon, M., Meyer, S. S., Odegard, N., Tucker, G. S., Weiland, J. L., Wollack, E., and Wright, E. L. *Astrophys. J., Suppl. Ser.*, 170, 2007.

Stoughton, C., Lupton, R. H., Bernardi, M., Blanton, M. R., Burles, S., Castander,

F. J., Connolly, A. J., Eisenstein, D. J., Frieman, J. A., Hennessy, G. S., Hindsley, R. B., Ivezić, Ž., Kent, S., Kunszt, P. Z., Lee, B. C., Meiksin, A., Munn, J. A., Newberg, H. J., Nichol, R. C., Nicinski, T., Pier, J. R., Richards, G. T., Richmond, M. W., Schlegel, D. J., Smith, J. A., Strauss, M. A., SubbaRao, M., Szalay, A. S., Thakar, A. R., Tucker, D. L., Vanden Berk, D. E., Yanny, B., Adelman, J. K., Anderson, J. E., Jr., Anderson, S. F., Annis, J., Bahcall, N. A., Bakken, J. A., Bartelmann, M., Bastian, S., Bauer, A., Berman, E., Böhringer, H., Boroski, W. N., Bracker, S., Briegel, C., Briggs, J. W., Brinkmann, J., Brunner, R., Carey, L., Carr, M. A., Chen, B., Christian, D., Colestock, P. L., Crocker, J. H., Csabai, I., Czarapata, P. C., Dalcanton, J., Davidsen, A. F., Davis, J. E., Dehnen, W., Dodelson, S., Doi, M., Dombeck, T., Donahue, M., Ellman, N., Elms, B. R., Evans, M. L., Eyer, L., Fan, X., Federwitz, G. R., Friedman, S., Fukugita, M., Gal, R., Gillespie, B., Glazebrook, K., Gray, J., Grebel, E. K., Greenawalt, B., Greene, G., Gunn, J. E., de Haas, E., Haiman, Z., Haldeman, M., Hall, P. B., Hamabe, M., Hansen, B., Harris, F. H., Harris, H., Harvanek, M., Hawley, S. L., Hayes, J. J. E., Heckman, T. M., Helmi, A., Henden, A., Hogan, C. J., Hogg, D. W., Holmgren, D. J., Holtzman, J., Huang, C.-H., Hull, C., Ichikawa, S.-I., Ichikawa, T., Johnston, D. E., Kauffmann, G., Kim, R. S. J., Kimball, T., Kinney, E., Klaene, M., Kleinman, S. J., Klypin, A., Knapp, G. R., Korienek, J., Krolik, J., Kron, R. G., Krzesiński, J., Lamb, D. Q., Leger, R. F., Limmongkol, S., Lindenmeyer, C., Long, D. C., Loomis, C., Loveday, J., MacKinnon, B., Mannery, E. J., Mantsch, P. M., Margon, B., McGehee, P., McKay, T. A., McLean, B., Menou, K., Merelli, A., Mo, H. J., Monet, D. G., Nakamura, O., Narayanan, V. K., Nash, T., Neilsen, E. H., Jr., Newman, P. R., Nitta, A., Odenkirchen, M., Okada, N., Okamura, S., Ostriker, J. P., Owen, R., Pauls, A. G., Peoples, J., Peterson, R. S., Petravick, D., Pope, A., Pordes, R., Postman, M., Prosapio, A., Quinn, T. R., Rechenmacher, R., Rivetta, C. H., Rix, H.-W., Rockosi, C. M., Rosner, R., Ruthmansdorfer, K., Sandford, D., Schneider, D. P., Scranton, R., Sekiguchi, M., Sergey, G., Sheth, R., Shimasaku, K., Smee, S., Snedden, S. A., Stebbins, A., Stubbs, C., Szapudi, I., Szkody, P., Szokoly, G. P., Tabachnik, S., Tsvetanov, Z., Uomoto, A., Vogeley, M. S., Voges, W., Waddell, P., Walterbos, R., Wang, S.-i., Watanabe, M., Weinberg, D. H., White, R. L., White, S. D. M., Wilhite, B., Wolfe, D., Yasuda, N., York, D. G., Zehavi, I., and Zheng, W. 123:485, 2002.

Sunyaev, R. A. and Zel'dovich, Y. B. *Astrophys. Space. Sci.*, 7:3, 1970.

Suto, Y. The Universe Traced by Clusters. In *Constructing the Universe with Clusters of Galaxies*. 2000.

Swinbank, A. M., Edge, A. C., Smail, I., Stott, J. P., Bremer, M., Sato, Y., van Breukelen, C., Jarvis, M., Waddington, I., Clewley, L., Bergeron, J., Cotter, G., Dye, S., Geach, J. E., Gonzalez-Solares, E., Hirst, P., Ivison, R. J., Rawlings, S., Simpson, C., Smith, G. P., Verma, A., and Yamada, T. *Mon. Not. R. Astron. Soc.*, 379:1343, 2007a.

Swinbank, A. M., Edge, A. C., Smail, I., Stott, J. P., Bremer, M., Sato, Y., van

Breukelen, C., Jarvis, M., Waddington, I., Clewley, L., Bergeron, J., Cotter, G., Dye, S., Geach, J. E., Gonzalez-Solares, E., Hirst, P., Ivison, R. J., Rawlings, S., Simpson, C., Smith, G. P., Verma, A., and Yamada, T. *Mon. Not. R. Astron. Soc.*, 379:1343, 2007b.

Swinbank, A. M., Smail, I., Chapman, S. C., Blain, A. W., Ivison, R. J., and Kell, W. C. *Astrophys. J.*, 617:64, 2004.

Tody, D. In R. J. Hanisch, R. J. V. Brissenden, and J. Barnes, editors, *Astronomical Data Analysis Software and Systems II*, volume 52 of *Astronomical Society of the Pacific Conference Series*, pages 173–183. 1993.

Valdes, F. *APEXTRACT Package Revisions Summary: IRAF Version 2.10.* IRAF Group – Central Computing Services: National Optical Astronomy Observatories, 1990a. Tuscon, Arizona.

Valdes, F. *The IRAF APEXTRACT Package.* IRAF Group – Central Computing Services: National Optical Astronomy Observatories, 1990b. Tuscon, Arizona.

Voit, G. M. *Rev. Mod. Phys.*, 77:207, 2005.

Walsh, J. R., Pirzkal, N., and Pasquali, A. In S. Arribas, A. Koekemoer, and B. Whitmore, editors, *The 2002 HST Calibration Workshop : Hubble after the Installation of the ACS and the NICMOS Cooling System*, page 90. 2002.

Webb, T. M. A., Yee, H. K. C., Ivison, R. J., Hoekstra, H., Gladders, M. D., Barrientos, L. F., and Hsieh, B. C. *Astrophys. J.*, 631:187, 2005.

Wray, J. J., Bahcall, N. A., Bode, P., Boettiger, C., and Hopkins, P. F. *Astrophys. J.*, 652:907, 2006.

Yan, R., Newman, J. A., Faber, S. M., Kondaris, N., Koo, D., and Davis, M. *Astrophys. J.*, 648:281, 2006.

Yee, H. K. C. In A. Diaferio, editor, *IAU Colloq. 195: Outskirts of Galaxy Clusters: Intense Life in the Suburbs*, pages 176–182. 2004.

Yee, H. K. C., Gladders, M. D., Gilbank, D. G., Majumdar, S., Hoekstra, H., Ellingson, E., and the RCS-2 Collaboration. *ArXiv Astrophysics e-prints*, astro-ph/0701839, 2007.

Zwicky, F. *Helv. Phys. Acta*, 6:110, 1933.

Zwicky, F., Herzog, E., Wild, P., Karpowicz, M., and Kowal, C. T. *Catalogue of Galaxies and of Clusters of Galaxies, Volumes I-VI.* Pasadena: California Institute of Technology, 1961-1968.

Appendix A
RCS2319+00 VLT–VIMOS Redshift Catalogue

A.1 Supercluster Members

Table A.1 - Spectroscopically confirmed RCS2319+00 supercluster members: $0.8857 \leq z \leq 0.9239$.

Object	RA	DEC	z	Confidence Level	Emission/Absorprion Lines Identified (Å)	R_{mag}
126	23:19:55.1	+00:40:25.8	0.9017	1	[OII]	23.40
545	23:20:03.3	+00:36:07.8	0.9101	1	[OII]	22.59
675	23:20:03.6	+00:34:55.5	0.9115	1	[OII]	23.66
600072	23:19:42.4	+00:36:47.5	0.9050	1	[OII]	23.76
600091	23:19:56.8	+00:36:47.3	0.8986	2	[OII]-HeI	22.15
600107	23:19:39.6	+00:36:55.9	0.9049	1	[OII]	23.69
600309	23:19:42.9	+00:37:36.2	0.8908	1	[OII]	22.58
600323	23:19:52.2	+00:37:35.6	0.9117	1	[OII]	22.65
600381	23:19:57.5	+00:37:46.9	0.9122	1	H&K-H_δ	22.35
600539	23:19:53.3	+00:38:16.6	0.9051	1	H&K	22.73
600714	23:19:37.8	+00:38:55.8	0.9042	1	[OII]	23.53
601071	23:19:40.4	+00:40:03.3	0.9096	2	[OII]	23.90
601168.1	23:19:37.5	+00:40:27.5	0.9023	1	[OII]-[OIII]	22.77
602360	23:19:43.2	+00:44:13.2	0.9096	2	[OII]	23.62
602654	23:19:56.1	+00:44:59.0	0.8980	2	[OII]	23.11
602656	23:19:47.0	+00:45:01.0	0.9013	1	[OII]-H&K	23.41
603030	23:19:58.0	+00:46:15.4	0.9002	1	[OII]	23.37
603813	23:19:56.5	+00:48:58.8	0.9013	1	[OII]	23.81
700681	23:20:01.2	+00:38:59.6	0.9039	2	[OII]	23.32
702065	23:20:01.9	+00:44:26.5	0.9056	2	[OII]-[NeIII]	23.46
702572	23:20:01.5	+00:46:14.6	0.8986	1	[OII]-H_β	22.71
703199	23:19:59.7	+00:48:28.8	0.9005	1	[OII]	22.22
800043	23:20:47.5	+00:36:26.6	0.9018	2	[OII]	23.56
907398	23:19:57.5	+00:36:27.4	0.8937	2	[OII]	23.72
907552	23:19:57.2	+00:35:38.0	0.8876	1	[OII]-[OIII]	22.06
907612	23:20:30.0	+00:42:47.5	0.9117	2	[OII]	23.38
907901	23:20:29.3	+00:44:41.9	0.9010	2	[OII]	22.48
908297	23:20:43.6	+00:46:49.1	0.8924	2	[OII]	21.18
909852	23:19:42.8	+00:32:06.8	0.9056	1	[OII]	21.60
9010070	23:20:07.0	+00:35:56.5	0.9021	1	[OII]-H_δ	23.29
9010153	23:20:05.8	+00:35:28.7	0.9093	1	[OII]	24.57
9010176	23:20:06.3	+00:35:23.0	0.9026	1	[OII]	25.09
9010283	23:20:03.6	+00:34:55.5	0.9101	1	[OII]	23.66
9010933	23:19:55.3	+00:27:37.6	0.9056	2	[OII]	23.34
9010995	23:19:44.5	+00:27:22.8	0.8991	2	[OII]	22.72
9012182	23:20:19.9	+00:34:45.4	0.8988	1	[OII]-H_β-[OIII]	22.93

A.2 Field Galaxies

Table A.2 - Spectroscopically confirmed field galaxies in the RCS2319+00 supercluster field.

Object	RA	DEC	z	Confidence Level	Emission/Absorprion Lines Identified (Å)	R_{mag}
2	23:19:53.3	+00:38:06.8	0.6896	3	[OII]	24.00
19	23:19:43.5	+00:41:28.2	0.6093	1	[OII]-H&K	21.44
126.1	23:19:55.1	+00:40:25.8	0.9699	2	[OII]	23.40
142	23:19:45.3	+00:40:13.4	0.9973	2	[OII]	23.39
197	23:20:04.3	+00:39:39.2	0.8795	2	[OII]	282.86
214	23:20:06.7	+00:39:26.8	0.9713	3	[OII]	24.47
292	23:19:53.3	+00:38:39.6	0.7002	1	[OII]-[OIII]	23.29
325	23:19:43.0	+00:38:14.2	0.5275	1	[OII]-H&K	21.23
479	23:20:00.0	+00:36:47.9	0.5978	1	[OII]-[OIII]	21.87
539	23:19:51.8	+00:36:10.3	0.9316	1	[OII]	24.37
542	23:19:51.9	+00:36:12.6	0.9458	3	[OII]	22.43
616	23:20:00.4	+00:35:30.0	0.5540	1	[OII]-[OIII]	171.62
644	23:19:41.3	+00:35:12.2	0.8124	1	[OII]-[OIII]	22.97
648	23:19:41.1	+00:35:08.8	0.8103	2	[OII]	22.43
600037	23:19:52.2	+00:36:38.3	0.8471	2	[OII]	23.81
600069	23:19:53.9	+00:36:43.6	0.6512	1	[OII]-[OIII]	22.14
600128	23:19:54.0	+00:36:55.8	0.4978	1	G_{band}-H_{γ}	23.58
600128	23:19:54.0	+00:36:55.8	0.5849	1	[OII]	23.58
600149	23:19:41.0	+00:37:04.5	1.0362	2	[OII]	22.94
600167	23:19:50.2	+00:37:04.8	0.9286	1	[OII]-H&K	23.29
600199	23:19:51.8	+00:37:10.2	0.6676	1	[OII]	22.26
600222	23:19:50.3	+00:37:15.0	0.5586	1	H_{β}-[OIII]	23.54
600226	23:19:39.0	+00:37:19.9	0.7631	2	[OII]	23.85
600308	23:19:48.8	+00:37:34.1	0.6759	1	[OII]-H_{β}-[OIII]	23.93
600409	23:19:38.8	+00:37:57.6	0.8406	1	[OIII]	23.27
600460	23:19:42.3	+00:38:06.3	0.6676	1	[OII]-[OIII]	23.81
600460.1	23:19:42.3	+00:38:06.3	0.6705	1	[OII]	23.81
600495	23:19:55.4	+00:38:08.1	0.9300	2	[OII]	23.22
600586	23:19:40.3	+00:38:28.4	0.7172	1	[OII]	22.49
600598	23:19:40.7	+00:38:30.9	0.5401	1	[OII]-[OIII]	23.29
600618	23:19:52.2	+00:38:31.3	0.9250	1	[OII]	22.79
600645	23:19:38.4	+00:38:39.5	0.8133	1	[OII]-[OIII]	23.84
600673	23:19:42.9	+00:38:43.6	0.9249	1	[OII]	23.17
600695	23:19:37.6	+00:38:50.8	0.5983	2	[OII]-H_{β}	23.86
600757	23:19:41.2	+00:39:03.0	0.4963	1	H_{β}-[OIII]	23.66
600793	23:19:56.3	+00:39:05.3	0.5484	1	[OII]-[OIII]	23.43
600804	23:19:47.7	+00:39:09.4	0.7650	2	[OII]	24.07
600840	23:19:44.6	+00:39:17.3	1.2275	2	[OII]	23.11
600840.1	23:19:44.6	+00:39:17.3	0.6456	2	[OII]	23.11
600844	23:19:56.7	+00:39:14.8	0.6307	2	[OIII]	23.77
600844.1	23:19:56.7	+00:39:14.8	0.3364	1	H_{β}-[OIII]	23.77
600867	23:19:40.8	+00:39:22.8	0.4420	1	H_{β}-[OIII]	22.58
600915	23:19:55.7	+00:39:27.5	0.6173	1	H_{β}-[OIII]	23.43
600925	23:19:37.8	+00:39:34.4	0.5916	2	[OII]	23.81
601025	23:19:52.3	+00:39:49.0	0.9973	1	[OII]	23.21
601090	23:19:56.1	+00:40:04.6	0.6058	1	[OII]-HeII	23.13
601141.1	23:19:54.8	+00:40:17.4	0.5276	1	H&K-G_{band}	23.20
601141	23:19:54.8	+00:40:17.4	0.7038	2	[OII]	23.20
601168	23:19:37.5	+00:40:27.5	0.7604	1	[OII]	22.77
601320	23:19:43.0	+00:40:50.9	0.9724	2	[OII]	22.67
601323	23:19:52.1	+00:40:49.3	0.7566	2	[OII]	22.41
601413	23:19:52.7	+00:41:07.7	0.6088	2	[OII]	23.94
601414	23:19:44.6	+00:41:09.8	0.6185	3	[OII]	24.05
601430	23:19:56.9	+00:41:09.1	0.9324	1	[OII]	23.28
601471	23:19:53.4	+00:41:17.7	0.9976	2	[OII]	23.63

Continued on next page ...

Table A.2 - Continued from previous page

Object	RA	DEC	z	Confidence Level	Emission/Absorprion Lines Identified (Å)	R_{mag}
601790	23:19:53.5	+00:42:22.5	1.1833	2	[OII]	22.99
601792	23:19:42.4	+00:42:25.9	0.9976	2	[OII]	24.04
601854	23:19:53.0	+00:42:37.6	1.0333	2	[OII]	23.81
602012	23:19:39.6	+00:43:10.7	0.4517	1	H_β-[OIII]	22.47
602105	23:19:57.9	+00:43:22.0	0.5734	1	[OII]-H_γ	22.71
602130	23:19:45.3	+00:43:30.7	0.8849	2	[OII]	22.78
602180	23:19:45.4	+00:43:41.1	0.7773	2	[OII]	23.40
602271	23:19:49.8	+00:43:55.4	1.0875	2	[OII]	22.96
602327	23:19:51.2	+00:44:05.6	0.7456	2	[OII]-H_γ	23.39
602364	23:19:38.7	+00:44:15.2	0.8328	3	[OII]-[OIII]	23.55
602372	23:19:52.4	+00:44:13.9	0.7105	3	[OII]	22.84
602428	23:19:42.7	+00:44:23.4	1.0515	2	[OII]	23.91
602506	23:19:42.1	+00:44:35.8	0.5321	1	[OII]-[OIII]	23.07
602581	23:19:51.7	+00:44:47.5	1.0553	2	[OII]	22.63
602660	23:19:56.3	+00:45:00.3	0.4088	1	H_γ-[OIII]	23.14
602686	23:19:42.2	+00:45:08.9	1.1173	3	[OII]	23.47
602714	23:19:51.6	+00:45:11.8	0.9965	2	[OII]	23.38
602735	23:19:54.6	+00:45:16.0	1.0451	2	[OII]	24.01
602768	23:19:41.6	+00:45:25.5	0.4514	1	H_β-[OIII]	23.99
602768.1	23:19:41.6	+00:45:25.5	0.3197	2	H_β-[OIII]	23.99
602782	23:19:52.8	+00:45:25.6	0.6351	2	[OIII]	23.20
602814	23:19:43.4	+00:45:34.3	0.9667	2	[OII]	23.79
602864	23:19:38.1	+00:45:44.5	0.8188	2	H&K	22.52
602906	23:19:41.2	+00:45:52.6	0.1857	1	[OIII]-H_α	23.84
603016	23:19:40.1	+00:46:15.5	0.8470	1	[OII]	23.64
603017	23:19:51.5	+00:46:13.6	0.5305	1	[OII]-[OIII]	23.29
603057	23:19:44.9	+00:46:24.9	0.6893	2	[OII]	23.42
603107	23:19:43.4	+00:46:35.5	0.8819	1	[OII]-H_β-[OIII]	22.79
603124	23:19:52.3	+00:46:38.0	0.7212	2	[OII]	21.99
603124	23:19:52.3	+00:46:38.0	0.7212	2	[OII]	21.99
603173	23:19:40.2	+00:46:50.4	0.8591	2	[OII]	23.63
603221	23:19:38.0	+00:47:02.3	0.2716	3	HeII-[OIII]	23.13
603230	23:19:48.9	+00:47:02.0	0.6372	2	[OII]	23.91
603247	23:19:38.8	+00:47:09.2	0.8468	1	[OII]-[OIII]	24.00
603313	23:19:45.9	+00:47:20.6	0.6651	2	[OII]	23.30
603515	23:19:53.7	+00:47:58.0	0.4344	1	H_β-[OIII]	23.61
603561	23:19:41.7	+00:48:09.3	0.5806	1	[OIII]	23.99
603565	23:19:52.2	+00:48:07.6	0.8471	3	[OII]	22.63
603658	23:19:44.5	+00:48:29.8	0.5863	3	[OII]	22.96
603686	23:19:55.9	+00:48:33.5	0.9536	3	[OII]	23.81
603704	23:19:55.4	+00:48:37.2	0.7591	1	[OII]	22.45
603753	23:19:52.2	+00:48:47.8	0.9662	1	[OII]	22.49
603838	23:19:39.6	+00:49:07.8	1.0931	2	[OII]	23.69
603844	23:19:38.5	+00:49:09.8	0.7540	1	[OII]	23.57
603866	23:19:54.6	+00:49:12.0	0.1372	1	[OIII]-H_α	24.08
603990	23:19:40.7	+00:49:40.0	0.7792	1	H&K-H_γ	23.42
604003	23:19:52.4	+00:49:41.7	0.3940	2	H_α	23.53
604060	23:19:52.9	+00:49:52.6	0.7541	1	[OII]	22.49
604075	23:19:41.4	+00:49:58.8	0.5441	2	[OII]	23.46
700016	23:20:02.1	+00:36:34.1	0.9343	1	[OII]	23.46
700017	23:20:19.9	+00:36:29.5	0.3487	3	[OIII]-H_β-[OIII]	23.39
700069	23:20:20.5	+00:36:41.9	1.0005	2	[OII]	23.41
700141	23:20:21.9	+00:36:54.9	0.7776	2	[OII]	23.89
700147	23:20:04.6	+00:37:00.9	0.6482	3	[OII]	23.24
700168	23:20:24.3	+00:37:01.1	0.8259	2	[OII]	23.69
700182	23:19:59.4	+00:37:11.2	0.8460	1	[OII]-[OIII]	23.32
700185	23:20:07.8	+00:37:09.5	0.5554	1	[OII]-[OIII]	22.36
700236	23:20:20.0	+00:37:17.7	0.5356	3	[OII]	23.93

Continued on next page ...

Table A.2 - Continued from previous page

Object	RA	DEC	z	Confidence Level	Emission/Absorprion Lines Identified (Å)	R_{mag}
700266	23:20:02.0	+00:37:28.8	0.8463	2	[OII]	23.00
700311	23:20:07.3	+00:37:35.1	1.0944	1	[OII]-[NeIII]-H_γ	23.40
700352	23:20:07.2	+00:37:43.7	0.8755	1	[OII]-H&K	23.04
700363	23:20:19.8	+00:37:43.2	0.7577	2	H&K-H_γ	22.82
700457	23:20:22.0	+00:38:01.3	0.7566	1	[OII]-[OIII]	23.20
700468.1	23:20:02.7	+00:38:08.5	0.9316	2	[NeV]-[OII]	22.90
700478	23:20:08.7	+00:38:08.2	0.5549	1	[OII]-H_β-[OII]	22.05
700513	23:20:09.0	+00:38:17.2	0.8095	1	[OII]-H_γ	23.24
700553	23:20:22.8	+00:38:24.1	0.3183	1	[OIII]-H_α	21.22
700553	23:20:22.8	+00:38:24.1	0.3183	1	[OIII]-H_α	21.22
700657	23:20:06.2	+00:38:51.9	0.8452	1	[OII]-[OIII]	23.17
700724	23:20:18.6	+00:39:03.7	1.1226	1	MgII-[OII]	23.91
700742	23:20:20.7	+00:39:06.8	1.1779	2	[OIII]	22.53
700866	23:20:18.2	+00:39:37.6	0.7752	1	[OII]-[OIII]	23.42
700916	23:20:03.9	+00:39:49.7	0.8114	1	[OII]-OIII	23.39
701091	23:20:04.6	+00:40:31.8	0.6060	2	[OII]	22.46
701249	23:20:03.1	+00:41:15.9	1.0059	2	[OII]	23.48
701514	23:20:24.6	+00:42:13.5	0.9337	2	[OII]	22.85
701633	23:20:07.3	+00:42:48.0	0.9353	2	[OII]	23.54
701689	23:20:19.4	+00:42:56.2	0.3613	1	H_β-[OIII]	23.33
701776	23:20:07.9	+00:43:22.0	0.4818	1	H_β-[OIII]	22.24
701856	23:20:25.1	+00:43:35.8	0.6126	2	[OII]	23.26
701882	23:20:08.3	+00:43:43.1	0.7114	2	[OIII]	23.40
701888	23:20:04.9	+00:43:45.5	0.5045	1	H_β-[OIII]	23.55
701971	23:20:23.7	+00:43:59.5	0.3470	1	H_β-[OIII]	22.96
701975	23:20:08.8	+00:44:03.8	0.7144	2	H_β-[OIII]	23.85
701997	23:20:01.5	+00:44:09.2	0.8666	2	[OII]	22.49
702058	23:20:19.1	+00:44:21.1	0.8218	1	[OII]-H_δ	23.15
702186	23:20:01.5	+00:44:50.4	0.6391	2	[OIII]	23.09
702231	23:20:25.1	+00:44:53.9	1.0142	2	[OII]	22.96
702284	23:20:20.6	+00:45:05.2	0.8015	2	[OIII]	23.53
702367	23:20:07.1	+00:45:23.2	0.7097	2	[OII]	23.49
702463	23:20:04.5	+00:45:46.2	1.0338	2	[OII]	23.97
702489	23:20:21.4	+00:45:50.3	0.5630	3	H&K	23.08
702504	23:20:08.5	+00:45:57.0	0.8672	3	[OII]	23.81
702535	23:20:07.8	+00:46:05.2	0.8039	1	[OII]-[OIII]	23.61
702596	23:20:24.9	+00:46:14.5	1.3051	2	[OII]	22.68
702668	23:20:07.3	+00:46:33.3	0.7900	3	[OII]	22.89
702726	23:20:06.5	+00:46:46.6	0.5597	2	[OII]	23.12
703104	23:20:23.7	+00:48:01.4	0.5871	1	[OII]-[OIII]	23.07
703123	23:20:01.4	+00:48:09.4	0.6235	2	[OIII]	23.07
703167	23:20:23.3	+00:48:16.0	1.0185	2	[OII]	24.01
703237	23:20:04.9	+00:48:36.9	0.7550	1	[OII]-H&K+	23.11
703278	23:20:03.1	+00:48:45.0	0.9404	2	[OII]	22.50
703354	23:20:06.0	+00:48:59.2	0.7550	2	[OII]	22.63
703442	23:20:04.2	+00:49:13.5	0.9925	2	[OII]	23.69
703498	23:20:00.0	+00:49:26.7	1.0140	3	[OII]	22.25
800057	23:20:35.6	+00:36:31.5	0.5222	2	H&K-G_{band}	22.22
800096	23:20:49.1	+00:36:37.3	0.8621	2	[OII]	23.05
800170	23:20:41.4	+00:36:52.1	0.5267	2	[OII]	23.66
800243	23:20:48.0	+00:37:04.3	0.7894	3	[OII]	23.69
800246	23:20:27.9	+00:37:08.6	0.5243	3	H&K	23.33
800271	23:20:44.1	+00:37:10.7	1.1207	2	[OII]	23.77
800306	23:20:30.3	+00:37:18.1	0.8833	3	[OII]	23.64
800310	23:20:42.9	+00:37:16.5	1.0260	2	[OII]	24.08
800318	23:20:39.9	+00:37:18.4	0.5315	1	[OII]-[OIII]	22.32
800345	23:20:30.2	+00:37:26.0	0.5462	1	[OII]-[OIII]	23.38
800357	23:20:43.4	+00:37:26.0	1.2589	2	[OII]	23.67

Continued on next page ...

Table A.2 - Continued from previous page

Object	RA	DEC	z	Confidence Level	Emission/Absorprion Lines Identified (Å)	R_{mag}
800410	23:20:35.0	+00:37:38.7	0.6136	1	[OII]-[OIII]	23.70
800523	23:20:32.3	+00:38:02.1	0.4448	2	H_δ-H_β-[OIII]	22.93
800536	23:20:48.4	+00:38:02.4	0.9911	2	[OII]-H_γ	23.89
800576	23:20:38.6	+00:38:11.8	1.1054	2	[OII]	24.09
800610	23:20:32.8	+00:38:20.6	1.1186	2	[OII]-HeI	23.50
800620	23:20:43.0	+00:38:20.5	0.7529	1	[OII]	24.01
800648.1	23:20:46.5	+00:38:25.2	0.8205	3	[OII]	23.75
800648	23:20:46.5	+00:38:25.2	0.7558	2	[OII]	23.75
800678	23:20:32.3	+00:38:35.9	0.7725	2	[OII]	21.68
800678	23:20:32.3	+00:38:35.9	0.7725	2	[OII]	21.68
800711	23:20:45.2	+00:38:39.1	0.7635	2	H&K-G_{band}-H_γ	22.43
800715	23:20:30.6	+00:38:42.7	0.8637	3	[OII]	22.62
800741	23:20:42.6	+00:38:44.7	0.4750	1	[OIII]	23.52
800764	23:20:35.6	+00:38:51.0	0.7666	2	[OII]	23.93
800831	23:20:38.3	+00:39:04.3	0.5922	1	[OII]-[OIII]	23.32
800856	23:20:48.5	+00:39:06.9	0.5847	1	[OII]-[OIII]	23.54
800930	23:20:43.5	+00:39:22.2	0.7757	1	[OII]-[OIII]	22.95
800937	23:20:29.4	+00:39:25.9	0.6079	2	[OII]	23.67
907018	23:20:45.0	+00:39:33.8	0.9732	2	[OII]	21.96
907051	23:20:34.3	+00:39:45.7	0.7703	2	[OII]-G-H_γ	22.18
907059	23:20:45.8	+00:39:45.4	0.5600	2	[OII]-[NeIII]	22.04
907064	23:20:49.2	+00:39:46.8	0.5841	2	[OII]	22.33
907105	23:20:41.8	+00:39:57.4	0.7760	3	H&K	22.29
907414	23:19:48.6	+00:36:23.5	0.5420	1	H&K	21.01
907453	23:19:39.0	+00:36:12.2	0.9697	3	[OII]	25.59
907455	23:19:38.6	+00:36:11.6	0.6413	1	[OII]-[OIII]	22.61
907467	23:19:56.8	+00:36:04.7	0.6625	2	[OIII]	23.28
907473	23:19:47.7	+00:36:02.5	0.6998	1	[OII]	24.65
907485	23:19:59.6	+00:35:59.0	0.6904	1	H_β-[OIII]	24.10
907502.1	23:19:37.5	+00:35:52.5	0.6812	1	[OII]-H_γ-[OIII]	24.04
907502	23:19:37.5	+00:35:52.5	0.5954	2	[OII]	24.04
907546	23:19:51.8	+00:35:40.4	0.6684	2	[OII]	23.24
907550	23:19:51.9	+00:35:39.1	0.6676	1	[OII]	23.27
907551	23:19:47.7	+00:35:38.8	0.6909	2	[OII]	25.13
907553.1	23:19:38.6	+00:35:38.3	0.9520	2	[OII]	24.25
907576	23:19:37.6	+00:35:31.4	0.7446	1	[OII]	22.56
907587	23:19:55.5	+00:35:28.6	0.8092	1	[OII]	22.41
907615	23:19:44.8	+00:35:22.8	0.8822	2	[OII]	23.26
907616	23:19:54.1	+00:35:22.1	0.8323	2	[OII]	22.01
907616	23:19:54.1	+00:35:22.1	0.6364	2	[OII]	22.01
907653	23:20:49.4	+00:42:57.4	0.1638	1	[OIII]-H_α	23.07
907660	23:19:59.3	+00:35:11.6	0.6179	2	[OIII]	23.23
907685	23:19:40.6	+00:35:04.1	0.5498	2	[OIII]	24.88
907688	23:19:53.3	+00:35:03.5	0.5315	1	[OII]-[NeIII]-[OIII]	23.08
907716	23:20:46.1	+00:43:25.9	0.5618	2	[OII]	22.69
907733	23:20:37.7	+00:43:36.1	0.1340	1	[OIII]-[FeVI]-H_α	23.27
907755	23:20:36.6	+00:43:45.5	0.1496	1	[OIII]-H_α-[SII]	19.47
907783	23:20:40.9	+00:43:56.5	0.4410	1	[OIII]	22.88
907813	23:20:34.6	+00:44:08.1	0.8285	3	[OII]	23.26
907827	23:20:45.4	+00:44:10.4	1.0684	3	[OII]	22.28
907864	23:20:43.6	+00:44:21.9	0.7537	2	[OII]	23.38
907908	23:20:45.1	+00:44:41.2	0.8520	2	H&K	22.98
907937	23:20:36.9	+00:44:50.2	0.5930	2	[OII]-G_{band}-H_γ	22.18
907966	23:20:31.6	+00:45:02.8	0.4950	2	H&K	20.94
907969	23:20:42.9	+00:45:01.5	0.8385	2	[OII]	23.28
908036	23:20:36.7	+00:45:29.4	0.5541	1	[OII]-H&K	21.07
908036.1	23:20:36.7	+00:45:29.4	0.7610	2	H&K	21.07
908040	23:20:46.6	+00:45:29.6	0.5970	1	[OII]-H_β-[OIII]	21.91

Continued on next page ...

Table A.2 - Continued from previous page

Object	RA	DEC	z	Confidence Level	Emission/Absorprion Lines Identified (Å)	R_{mag}
908077	23:20:36.4	+00:45:41.0	0.5541	1	[OII]-[OIII]	22.47
908101	23:20:48.8	+00:45:48.3	0.3156	1	H_β-[OIII]	22.09
908133	23:20:46.3	+00:45:59.4	0.9353	2	[OII]	23.23
908146	23:20:33.5	+00:46:05.3	0.4511	1	H_β-[OIII]	21.46
908217	23:20:47.7	+00:46:22.2	0.2191	1	[OIII]-H_α	21.62
908259	23:20:42.2	+00:46:37.1	0.6880	2	G_{band}-H_γ-[OIII]	23.34
908325	23:20:44.7	+00:46:57.8	0.2621	1	H_β-[OIII]	21.80
908328	23:20:33.4	+00:47:00.8	1.1486	3	[OII]	22.35
908376	23:20:38.4	+00:47:12.5	0.5957	1	[OII]-[OIII]	22.75
908466	23:20:33.7	+00:47:43.6	0.2870	1	[OII]-[OIII]	22.56
908492	23:20:38.1	+00:47:52.1	0.5892	2	[OII]	21.89
908532	23:20:39.6	+00:48:04.3	0.3337	1	H_β-[OIII]	20.76
908571	23:20:48.1	+00:48:14.0	0.8377	1	[OII]-[OIII]	22.56
908595	23:20:32.7	+00:48:23.7	0.5508	1	[OII]-[OIII]	22.63
908631	23:20:28.4	+00:48:37.3	0.6918	3	[OII]	20.11
908637	23:20:43.3	+00:48:35.8	0.4884	1	H_β-[OIII]	23.16
909845	23:19:58.7	+00:32:07.5	0.4900	1	G_{band}-H_γ	20.00
909852.1	23:19:42.8	+00:32:06.8	0.8634	2	[OII]	21.60
909943	23:19:53.2	+00:31:40.8	0.8116	2	[OII]	22.87
909973	23:20:08.2	+00:36:23.9	0.6128	3	[OII]	23.87
909988	23:19:38.8	+00:31:29.5	0.5380	3	[OII]	22.30
9010044	23:19:52.5	+00:31:11.4	0.3896	1	H_β-[OIII]-H_α	22.86
9010068	23:19:51.6	+00:31:05.8	0.6965	1	[OII]-NI	23.15
9010071	23:19:41.5	+00:31:05.5	0.3220	1	H_β-[OIII]-H_α	22.30
9010099	23:19:37.2	+00:30:58.1	0.4737	1	H_β-[OIII]	21.90
9010104	23:20:03.6	+00:35:47.7	0.5517	1	[OII]-[OIII]	22.65
9010109	23:20:01.5	+00:35:47.2	0.8135	2	[OII]	23.32
9010134	23:19:48.0	+00:30:49.5	0.3509	1	H_β-[OIII]	23.13
9010148	23:19:39.1	+00:30:47.2	1.0470	2	[OII]	23.21
9010163	23:19:53.4	+00:30:43.9	0.7059	1	[OII]-[OIII]	23.33
9010182	23:19:43.6	+00:30:37.8	0.8591	2	[OII]	22.47
9010186	23:19:52.7	+00:30:37.0	0.7075	2	[OII]	22.02
9010209	23:19:49.7	+00:30:31.6	0.9369	2	[OII]	22.77
9010225	23:20:06.8	+00:35:11.6	0.5881	2	[OII]	22.70
9010250	23:19:37.0	+00:30:23.7	0.6032	1	[OII]-[OIII]	21.91
9010253	23:19:48.8	+00:30:22.8	0.9525	3	[OII]	22.80
9010275	23:19:43.9	+00:30:15.6	0.6990	1	H&K-G_{band}	21.88
9010296	23:19:40.9	+00:30:11.3	0.5082	1	[OII]-[OIII]	20.85
9010315	23:19:40.7	+00:30:06.9	0.5095	1	[OII]-[OIII]	21.32
9010370	23:19:40.8	+00:29:54.6	0.5114	1	[OII]-[OII]	22.13
9010424	23:19:49.5	+00:29:40.7	0.9624	3	[OII]	23.01
9010454	23:19:58.1	+00:29:32.0	0.5154	1	[OII]-[OIII]	23.27
9010457	23:19:49.1	+00:29:31.7	1.0480	2	[OII]	21.06
9010482	23:19:51.6	+00:29:25.7	0.7462	1	[OII]-[OIII]	21.52
9010506	23:19:53.3	+00:29:20.5	1.0303	3	[OII]	23.04
9010554	23:19:40.1	+00:29:09.5	0.6995	1	[OII]-[OIII]	21.93
9010558	23:19:52.4	+00:29:08.4	0.6060	2	H&K-G_{band}	21.68
9010613	23:19:37.4	+00:28:57.7	0.6127	1	H_δ-[OIII]	23.45
9010646	23:19:42.4	+00:28:47.4	0.5110	2	H&K-G_{band}	20.97
9010647	23:19:55.8	+00:28:46.4	0.5280	1	[OII]-H_β-[OIII]	22.65
9010686	23:19:37.7	+00:28:40.0	0.6527	2	[OIII]	21.89
9010699	23:19:41.8	+00:28:35.9	0.5103	1	[OII]-[OIII]	22.85
9010730	23:19:56.8	+00:28:28.6	0.7556	1	[OII]-H&K	21.78
9010750	23:19:50.0	+00:28:23.6	0.3140	2	H_α-H_α	22.80
9010772	23:19:50.8	+00:28:14.3	0.5311	2	H&K-G_{band}	22.01
9010829	23:19:51.2	+00:28:02.4	0.5338	2	H&K-G_{band}	20.91
9010835	23:19:48.1	+00:28:00.9	0.5331	1	[OII]-H&K	20.63
9010985	23:19:42.6	+00:27:24.4	0.5090	3	H&K	21.04

Continued on next page ...

Table A.2 - Continued from previous page

Object	RA	DEC	z	Confidence Level	Emission/Absorprion Lines Identified (Å)	R_{mag}
9011024	23:19:40.9	+00:27:15.3	1.0040	3	H&K	22.54
9011054	23:19:48.2	+00:27:07.9	0.3924	1	H_β-[OIII]-H_α	22.35
9011064	23:19:37.6	+00:27:06.4	0.6665	2	[OII]	22.88
9011122	23:19:39.7	+00:26:53.2	0.9528	3	[OII]	23.25
9011148	23:19:52.2	+00:26:43.3	0.4224	1	[OIII]	22.57
9011166	23:19:52.8	+00:26:37.2	0.6089	1	H&K-H_γ	20.38
9011193	23:19:47.9	+00:26:29.9	0.5911	2	[OII]	22.24
9011194	23:19:58.8	+00:26:28.7	0.4021	2	H_α	19.62
9011213	23:19:50.6	+00:26:23.1	0.8787	2	[OII]	22.35
9011227	23:19:37.1	+00:26:21.4	0.8162	2	[OII]	22.82
9011245	23:19:39.7	+00:26:17.6	0.8138	1	[OII]-[FeII]	22.93
9011260	23:19:54.0	+00:26:13.8	0.6058	2	[OII]	22.91
9011266	23:19:43.8	+00:26:13.0	0.8642	2	[OII]	22.87
9011281	23:19:44.1	+00:26:08.5	0.3853	1	H_β-[OIII]	22.10
9011286	23:19:56.5	+00:26:06.3	1.0722	2	[OII]	22.50
9011318	23:19:54.8	+00:25:57.3	0.5106	1	[OII]-H_β-[OIII]	20.67
9011356	23:19:45.0	+00:25:45.5	0.6158	1	[OII]-[OIII]	22.87
9011356.1	23:19:45.0	+00:25:45.5	0.9286	1	[OII]-H_γ	22.87
9011390	23:19:41.5	+00:25:37.6	0.7030	2	[OII]	22.81
9011427	23:19:46.0	+00:25:25.4	0.5160	1	[OII]-[OIII]	21.78
9011437	23:19:57.0	+00:25:21.9	0.6068	2	H&K-G_{band}	20.71
9011495	23:19:37.6	+00:25:03.8	0.5149	1	H_γ-[OIII]	23.49
9011497	23:19:46.8	+00:25:02.6	0.5101	2	H&K-H_δ	21.18
9011555	23:19:41.1	+00:24:47.1	0.6225	3	[OII]	21.84
9011835	23:20:27.7	+00:36:22.2	0.6123	1	[OII]-H_β-[OIII]	20.86
9011861	23:20:19.4	+00:36:16.5	0.8269	1	[OII]-H_β-[OIII]	22.74
9011872	23:20:24.0	+00:36:13.6	0.4723	1	[OIII]-MgIb	22.37
9011964	23:20:19.1	+00:35:47.7	0.5291	2	[OII]	23.42
9011996	23:20:19.0	+00:35:35.3	0.2771	1	H_β-[OIII]	21.77
9012029	23:20:19.8	+00:35:23.3	0.2785	1	H_β-[OIII]	22.77
9012101	23:20:22.6	+00:35:05.0	0.4410	1	H_β-[OIII]	22.57
9012135	23:20:23.6	+00:34:55.6	0.5313	1	[OII]-[OIII]	23.05
9012225	23:20:20.8	+00:34:34.7	0.5330	2	H&K	22.47
9012267	23:20:26.7	+00:34:19.9	0.5262	1	[OII]-H&K	22.23
9012341	23:20:26.4	+00:33:59.2	0.8082	1	[OII]-[OIII]	22.65
9012353	23:20:19.7	+00:33:56.6	0.8116	2	[OII]	22.43
9012410	23:20:24.2	+00:33:36.8	0.5224	1	[OII]-H&K	22.66
9012608	23:20:03.4	+00:32:50.0	0.8138	2	[OII]	23.31
9012707	23:20:07.1	+00:32:17.3	0.3995	2	H_β-[OIII]	22.87
9012785	23:20:02.5	+00:31:55.4	0.6072	2	[OII]-[OIII]	23.05
9012824	23:20:02.5	+00:31:42.2	0.6158	1	[OII]-HeII-H_β	21.52
9012858	23:20:06.7	+00:31:30.3	0.5911	2	[OII]	22.70
9012957	23:20:07.5	+00:31:02.6	0.1060	1	[OIII]-H_α-[SII]	20.62
9013006	23:20:01.5	+00:30:48.5	0.3743	1	H_β-[OIII]	23.21
9013019	23:20:07.2	+00:30:43.4	0.5876	1	[OII]-H&K	23.36
9013046	23:20:04.8	+00:30:34.3	0.5895	1	[OII]-H_β-[OIII]	21.80
9013053	23:20:04.3	+00:30:32.6	0.5863	1	[OII]-[OIII]	22.34
9013059	23:20:27.7	+00:30:28.4	0.7489	3	H&K-G_{band}	22.32
9013098	23:20:20.8	+00:30:16.6	0.6008	1	[OII]-H_β-[OIII]	21.03
9013128	23:20:21.4	+00:30:05.6	0.5997	1	[OII]-[OIII]	21.91
9013162	23:20:06.7	+00:29:55.0	0.9300	2	[OII]	23.41
9013188	23:20:00.6	+00:29:47.6	0.6171	3	[OII]	23.35
9013190	23:20:07.3	+00:29:46.7	0.5627	1	[OII]-H_β	20.79
9013198	23:20:19.5	+00:29:43.0	0.5841	1	[OII]-[OIII]	21.98
9013234	23:20:21.0	+00:29:31.3	0.4930	1	[OII]-[OIII]	20.66
9013274	23:20:18.7	+00:29:21.2	0.9388	3	[OII]	23.13
9013283	23:20:03.6	+00:29:18.6	0.5280	3	[OII]	22.81
9013295	23:20:27.8	+00:29:12.9	0.6158	2	[OII]	23.45

Continued on next page ...

Table A.2 - Continued from previous page

Object	RA	DEC	z	Confidence Level	Emission/Absorprion Lines Identified (Å)	R_{mag}
9013320	23:20:07.1	+00:29:07.2	1.0115	3	[OII]	23.20
9013322	23:20:03.4	+00:29:07.1	0.8149	2	[OII]	22.69
9013331	23:20:23.6	+00:29:02.1	0.7607	1	[OII]-[OIII]	23.02
9013364	23:20:08.5	+00:28:54.6	1.0005	2	[OII]	22.62
9013383	23:20:20.2	+00:28:47.6	0.8512	2	[OIII]	23.32
9013414	23:20:21.4	+00:28:38.6	0.5435	1	H&K-H_β	21.05
9013428	23:20:00.5	+00:28:35.3	0.8680	2	H&K-G_{band}	22.07
9013487	23:20:22.5	+00:28:16.7	0.8425	1	[OII]-H&K	23.18
9013506	23:20:01.8	+00:28:13.8	0.6150	2	[OII]	22.63
9013549	23:20:20.9	+00:27:55.1	0.5425	1	[OII]-[OIII]	22.92
9013574	23:20:22.0	+00:27:46.6	0.8852	1	H_δ-[OIII]	21.94
9013611	23:20:17.7	+00:27:35.1	0.1900	3	H_α	21.02
9013618	23:20:06.7	+00:27:31.4	0.3136	1	H_β-[OIII]	21.84
9013684	23:20:18.8	+00:27:02.9	0.9455	2	[OII]	22.73
9013698	23:20:04.0	+00:27:01.6	0.8599	2	[OII]-H&K	21.57
9013753	23:20:03.1	+00:26:47.2	0.7467	2	[OII]	23.42
9013765	23:20:02.5	+00:26:41.6	0.7443	1	H_β-[OIII]	22.52
9013782	23:20:03.2	+00:26:36.5	0.8334	3	[OII]	22.33
9013788	23:20:21.0	+00:26:33.6	0.7438	1	[OII]-[OIII]	22.82
9013805	23:20:17.5	+00:26:25.3	0.5818	3	[OIII]	23.08
9013825	23:20:04.7	+00:26:19.3	0.3645	2	H_α	21.57
9013836	23:20:17.6	+00:26:15.3	0.7709	3	[OII]	23.40
9013893	23:20:07.3	+00:25:52.9	0.7821	1	[OII]-[OIII]	22.46
9013922	23:20:01.2	+00:25:44.7	0.9348	2	[OII]	23.43
9013929	23:20:26.8	+00:25:39.5	0.1854	1	H_β-[OIII]-H_α	22.83
9013997	23:20:06.6	+00:25:22.6	0.8704	1	[OII]-[NeIII]	23.00
9014030	23:20:02.9	+00:25:12.9	0.5098	2	[OII]	22.00
9014039	23:20:27.2	+00:25:05.2	0.5334	3	[OII]-[OIII]	22.34
9014121	23:20:05.4	+00:24:40.8	0.2800	1	[OIII]-H_α	23.19
9014151	23:20:06.7	+00:24:30.4	0.2808	1	[OIII]-H_α-[SII]	21.18
9014413	23:20:31.7	+00:36:13.7	0.5253	2	H&K-G_{band}	21.42
9014444	23:20:35.5	+00:36:01.6	0.8197	1	[OII]-H_β	23.39
9014462	23:20:33.6	+00:35:56.4	0.5942	3	[OIII]	23.24
9014493.1	23:20:42.3	+00:35:46.8	0.5123	1	G-H_γ-[OIII]	23.39
9014529	23:20:48.7	+00:35:33.8	0.5254	2	[OII]	23.33
9014551	23:20:42.3	+00:35:25.0	0.8047	2	[OII]	22.71
9014554	23:20:33.5	+00:35:24.5	0.8360	2	H&K	23.23
9014576	23:20:34.6	+00:35:17.5	0.5562	1	[OII]-H_β-[OIII]	21.93
9014600	23:20:44.3	+00:35:07.3	0.5476	1	[OII]-H_δ-[OIII]	23.22
9014616	23:20:35.0	+00:35:04.8	0.5250	2	H&K-G_{band}	22.11
9014681	23:20:32.2	+00:34:46.2	0.1881	1	H_β-[OIII]	21.41
9014689	23:20:42.0	+00:34:42.8	0.4404	1	[OII]-H_α	21.86
9014719	23:20:30.4	+00:34:34.5	0.7701	2	[OII]	23.46
9014723	23:20:30.3	+00:34:34.3	0.7682	1	[OII]-[OIII]	23.29
9014727.1	23:20:48.7	+00:34:30.1	0.6557	3	H&K	19.92
9014727	23:20:48.7	+00:34:30.1	0.5887	1	[OII]-H&K	19.92
9014732	23:20:39.8	+00:34:29.9	0.6131	1	[OII]-H&K	21.94
9014745	23:20:34.2	+00:34:25.4	0.4810	1	H_β-[OIII]	21.56
9014758	23:20:45.1	+00:34:20.1	0.3403	1	H_β-[OIII]	23.36
9014790	23:20:46.5	+00:34:08.8	0.4400	1	[OIII]-[FeVIII]	22.43
9014799	23:20:34.0	+00:34:08.6	0.7140	1	[OII]-[OIII]	23.38
9014829	23:20:42.8	+00:33:58.7	0.7695	2	[OIII]	23.18
9014863	23:20:44.6	+00:33:46.6	0.7156	1	[OII]-[OIII]	22.67
9014863	23:20:44.6	+00:33:46.6	0.7159	2	[OII]	22.67
9014865	23:20:31.3	+00:33:47.5	0.5264	1	[OII]-H&K	20.87
9014886	23:20:35.8	+00:33:37.7	0.8672	2	H&K	22.88
9014913	23:20:34.3	+00:33:26.7	1.2699	3	[OIII]	23.12
9014914	23:20:47.6	+00:33:24.6	0.6689	1	H_β-[OIII]	20.03

Continued on next page ...

Table A.2 - Continued from previous page

Object	RA	DEC	z	Confidence Level	Emission/Absorprion Lines Identified (Å)	R_{mag}
9014934	23:20:47.1	+00:33:13.6	0.9729	3	[OII]	23.12
9015309	23:20:46.4	+00:31:11.1	0.6949	1	[OII]-H_β-[OIII]	21.38
9015347	23:20:43.9	+00:31:01.6	0.6971	1	[OII]-H_β-[OIII]	22.52
9015444	23:20:37.6	+00:30:31.6	0.9547	2	[OII]	22.23
9015450	23:20:47.1	+00:30:28.9	0.9415	2	[OII]	23.07
9015479	23:20:32.6	+00:30:19.4	0.2206	1	H_β-[OIII]	22.71
9015517	23:20:46.0	+00:30:07.4	0.5820	3	H&K	21.49
9015549	23:20:31.3	+00:29:57.3	0.6020	2	G_{band}-H_γ-[OIII]	22.34
9015581	23:20:39.5	+00:29:43.5	1.1792	2	[OII]	23.47
9015617	23:20:47.1	+00:29:32.5	0.2957	1	[OIII]-H_α	22.38
9015675	23:20:37.8	+00:29:12.8	0.6448	1	[OII]-[OIII]	21.60
9015715	23:20:34.6	+00:29:00.0	1.0089	2	[OII]	23.45
9015742	23:20:30.9	+00:28:50.1	0.2010	1	[OIII]-H_α	23.40
9015763	23:20:32.3	+00:28:40.0	0.7185	2	[OII]	22.42
9015793	23:20:40.1	+00:28:28.5	1.0094	2	[OII]	23.20
9015832	23:20:45.1	+00:28:12.7	0.7330	1	[OII]-[OIII]	21.60
9015882	23:20:30.8	+00:27:57.8	1.1030	2	[OII]	23.13
9015899	23:20:48.8	+00:27:46.8	0.7496	1	[OII]-[OIII]	22.84
9015902	23:20:39.3	+00:27:47.5	1.0963	2	[OII]	23.32
9015955	23:20:30.5	+00:27:33.5	0.5358	1	[OII]-H&K	21.21
9015983	23:20:40.4	+00:27:23.3	1.0188	1	[OII]-H_δ	23.48
9016016	23:20:46.7	+00:27:14.0	0.2063	1	H_β-[OIII]	22.11
9016059	23:20:38.0	+00:26:58.2	0.5801	2	[OII]	23.21
9016123	23:20:47.6	+00:26:26.9	0.5527	2	[OII]	22.05
9016132	23:20:35.5	+00:26:26.1	0.6920	3	[OIII]	22.93
9016159	23:20:46.6	+00:26:14.6	0.7805	1	[OII]-H_δ-[OIII]	23.02
9016164	23:20:30.5	+00:26:14.8	0.3879	1	H_β-[OIII]	21.42
9016191	23:20:44.4	+00:26:06.0	0.2946	1	H_β-[OIII]	22.81
9016229	23:20:40.7	+00:25:53.5	0.5001	1	[OIII]	22.69
9016250	23:20:47.8	+00:25:46.0	0.8059	1	[OII]-[OIII]	22.41
9016260	23:20:36.5	+00:25:44.0	0.7413	2	[OII]	22.62
9016295	23:20:48.7	+00:25:32.1	0.6330	3	H&K	19.48
9016311	23:20:29.9	+00:25:30.6	0.4526	2	H&K-H_δ	21.64
9016337	23:20:46.6	+00:25:18.5	0.9536	2	[OII]	23.37
9016416	23:20:40.7	+00:24:57.5	0.7380	2	H&K-H_δ	21.55
9016423	23:20:29.6	+00:24:56.9	1.0333	2	[OII]	23.39
9016458	23:20:32.1	+00:24:47.4	0.5999	2	[OII]	21.58
9017287	23:19:09.9	+00:50:10.6	0.4727	1	H_β-[OIII]	22.31
9017327	23:19:02.4	+00:36:23.0	0.7142	2	[OII]	22.16
9017347	23:19:02.9	+00:36:46.2	0.7572	2	[OII]	23.27
9017369	23:19:05.6	+00:37:01.7	0.8594	2	[OII]	21.92
9017399.1	23:18:57.3	+00:37:47.0	0.5409	2	[OII]	21.77
9017405	23:18:57.4	+00:37:51.9	0.5439	3	[OII]	22.71
9017450	23:18:59.2	+00:38:28.7	0.5573	2	[OII]	21.73
9017468	23:18:58.2	+00:38:43.4	0.7574	2	[OII]	22.61
9017479	23:18:58.1	+00:39:02.3	0.7100	1	[OII]	22.94
9017482	23:18:59.7	+00:39:06.1	1.1454	1	[OII]-[FeII]	21.46
9017493	23:19:06.2	+00:39:16.4	0.9391	1	[OII]	21.50
9017501	23:18:59.8	+00:39:25.2	0.8390	2	[OII]	22.82
9017528	23:18:59.3	+00:39:52.9	0.7148	2	[OII]	22.86
9017547	23:18:59.7	+00:40:14.2	0.5621	2	[OII]	21.92
9017841	23:19:01.4	+00:44:37.1	0.7043	1	[OII]-[OIII]	23.38
9017851	23:19:03.9	+00:44:47.1	0.5272	2	H&K	21.54
9017915	23:19:02.2	+00:45:33.6	0.1873	2	H_α-[SII]	20.47
9017924	23:19:02.2	+00:45:51.2	0.3807	1	[OIII]	22.65
9017936	23:19:01.1	+00:46:00.5	0.3843	1	H_β-[OIII]-H_α	21.66
9017962	23:19:06.2	+00:46:22.1	0.7646	3	H&K-G_{band}-H_γ	22.44
9017972	23:19:02.3	+00:46:30.7	0.6410	2	[OII]-H_β	22.13

Continued on next page ...

Table A.2 - Continued from previous page

Object	RA	DEC	z	Confidence Level	Emission/Absorprion Lines Identified (Å)	R_{mag}
9018006	23:19:00.8	+00:47:06.4	0.6295	2	[OIII]-ArIV	23.48
9018115	23:19:04.3	+00:48:47.3	0.9581	1	[OII]-[NeIII]	22.75
9018123	23:19:03.5	+00:48:57.6	0.5989	1	[OII]-H&K	21.45
9018174.1	23:19:02.5	+00:49:51.6	0.3667	1	[OIII]	23.47
9018174	23:19:02.5	+00:49:51.6	0.4438	1	H_β-[OIII]	23.47
9018239.1	23:19:08.7	+00:36:35.7	0.7032	3	[OII]	23.04
9018243	23:19:27.5	+00:36:35.6	0.7145	3	[OII]-H&K	23.15
9018249	23:19:27.5	+00:36:37.1	0.7494	2	[OII]	21.72
9018269	23:19:13.3	+00:36:44.3	0.5978	1	[OII]-[OIII]	22.17
9018273	23:19:13.0	+00:36:46.2	0.5176	1	[OII]-[OIII]	22.98
9018304	23:19:14.6	+00:37:01.0	0.7727	2	[OII]	22.02
9018333	23:19:15.5	+00:37:10.9	0.5490	1	[OII]-G_{band}-H_γ	20.90
9018372	23:19:11.9	+00:37:26.6	0.7024	2	[OII]	22.84
9018443	23:19:10.6	+00:37:54.0	0.7518	1	[OII]	22.44
9018448	23:19:12.8	+00:37:54.8	0.0491	1	H_α	19.45
9018493	23:19:27.4	+00:38:16.0	0.8731	2	H&K	23.15
9018495	23:19:14.5	+00:38:17.5	1.0816	2	[OII]	22.69
9018521	23:19:08.8	+00:38:28.8	0.6563	2	[OII]	23.05
9018523	23:19:22.5	+00:38:30.6	0.8605	2	[OII]	22.88
9018553	23:19:21.5	+00:38:42.5	0.9697	2	[OII]	23.45
9018585	23:19:25.7	+00:38:53.2	0.7148	2	[OII]	22.26
9018621	23:19:23.0	+00:39:05.4	0.6568	2	[OII]	20.33
9018649	23:19:23.3	+00:39:13.8	0.5978	2	[OII]	22.26
9018719	23:19:21.1	+00:39:39.8	0.5428	1	H&K	22.30
9018751	23:19:09.8	+00:39:52.8	0.7553	2	[OII]	23.38
9018778	23:19:25.4	+00:40:02.4	0.7776	3	[OII]-HeII	23.46
9018782	23:19:10.8	+00:40:05.5	0.7561	2	[OII]	22.08
9018789	23:19:24.2	+00:40:06.9	0.5254	3	[OII]	20.62
9018797	23:19:11.1	+00:40:13.0	0.6219	2	H_β-[OIII]	22.89
9018800	23:19:27.0	+00:40:13.8	0.4460	1	H_β-[OIII]	21.80
9018803	23:19:20.3	+00:40:15.2	0.6020	2	G_{band}-H_γ-[OIII]	22.22
9018806	23:19:09.9	+00:40:16.0	0.1345	1	[OIII]-[FeVII]-H_α	20.11
9018824	23:19:09.6	+00:40:24.0	0.4566	2	[OIII]-[OIII]	22.56
9018826	23:19:19.5	+00:40:24.4	0.5200	3	[OII]	21.97
9018868	23:19:13.6	+00:40:41.7	0.6088	1	[OII]-H_β-[OIII]	20.84
9018898	23:19:16.8	+00:40:52.8	0.6287	3	[OII]	23.39
9018907	23:19:27.9	+00:40:54.4	0.4324	2	H_β-[OIII]	23.08
9018924	23:19:17.3	+00:41:00.8	1.0268	2	[OII]	20.39
9018943	23:19:27.2	+00:41:09.9	0.4270	2	[OIII]	22.88
9018954	23:19:18.1	+00:41:13.3	0.5586	3	[OII]	22.91
9018972	23:19:23.3	+00:41:21.2	0.3174	1	H_β-[OIII]	21.98
9018977	23:19:11.3	+00:41:23.7	0.9683	2	[OII]	23.02
9018984	23:19:20.6	+00:41:25.4	0.7322	3	[OII]	22.65
9019022	23:19:19.3	+00:41:43.2	1.0083	2	[OII]	23.07
9019379	23:19:08.8	+00:43:53.6	0.5782	1	[OII]	21.67
9019380	23:19:18.6	+00:43:53.3	0.4294	3	H_α	20.91
9019422.1	23:19:25.7	+00:44:04.8	0.1382	1	[OII]-H_α	23.44
9019429.1	23:19:16.8	+00:44:07.6	0.7019	2	?2nd	23.48
9019508	23:19:14.6	+00:44:36.2	0.2900	2	H_β-[OII]	21.48
9019520	23:19:25.1	+00:44:39.1	0.1382	1	[OIII]-H_α	20.44
9019537	23:19:13.0	+00:44:47.1	0.2636	1	H_β-[OIII]-H_α	19.88
9019566	23:19:28.1	+00:44:59.1	0.8065	2	[OII]	23.34
9019600	23:19:13.8	+00:45:10.9	0.7043	2	[OII]	21.50
9019611	23:19:24.6	+00:45:14.8	0.5037	1	H_β-[OIII]	23.13
9019627	23:19:23.6	+00:45:22.8	0.8122	2	[OII]	22.21
9019632	23:19:13.8	+00:45:24.7	0.7529	1	[OII]-H_δ	22.22
9019661	23:19:12.8	+00:45:34.7	0.7218	2	[OII]	23.03
9019706	23:19:22.0	+00:45:51.3	1.3523	2	[OII]	20.43

Continued on next page ...

Table A.2 - Continued from previous page

Object	RA	DEC	z	Confidence Level	Emission/Absorprion Lines Identified (Å)	R_{mag}
9019707	23:19:12.3	+00:45:52.1	0.2753	1	H_β-[OIII]-H_α	20.53
9019761	23:19:20.0	+00:46:11.6	0.6053	1	[OII]-[OIII]	21.96
9019787	23:19:25.8	+00:46:24.2	0.7529	1	[OII]-H&K	22.77
9019809	23:19:13.1	+00:46:34.3	0.5763	1	[OII]-[OIII]	22.95
9019812	23:19:28.4	+00:46:34.1	0.2688	1	[OIII]-H_α	20.15
9019835	23:19:25.1	+00:46:45.6	0.2630	1	[OIII]-MgIb	19.72
9019860	23:19:12.1	+00:46:56.8	0.7851	2	[OII]-[NeIII]	23.47
9019861.1	23:19:23.3	+00:46:56.5	0.5246	1	[OII]-[OIII]	20.96
9019883	23:19:13.6	+00:47:08.1	0.8685	1	[OII]	22.58
9019898	23:19:11.0	+00:47:17.6	1.1468	2	H_β-[OIII]	23.27
9019908	23:19:25.9	+00:47:21.5	1.0373	2	[OII]	23.49
9019929	23:19:08.4	+00:47:29.3	0.7521	1	[OII]	23.10
9019936	23:19:24.2	+00:47:29.7	0.8707	1	[OII]-NaI	22.73
9019993	23:19:23.5	+00:47:51.5	0.5824	2	H&K	20.11
9020035	23:19:07.6	+00:48:12.3	1.0274	2	[OII]	19.64
9020043	23:19:24.2	+00:48:12.4	0.9514	2	[OII]	23.03
9020083	23:19:23.2	+00:48:27.3	0.8678	1	H&K	23.15
9020113	23:19:25.6	+00:48:37.6	0.6219	1	[OII]-[OIII]	20.08
9020138	23:19:13.7	+00:48:46.1	0.8852	2	[OII]	22.83
9020197	23:19:08.0	+00:49:10.7	0.8723	1	[OII]	23.13
9020214	23:19:13.5	+00:49:19.1	0.6118	2	[OII]	22.23
9020249	23:19:28.4	+00:49:33.2	0.2808	1	H_β-[OIII]-H_α	21.19
9020298	23:19:00.7	+00:36:03.4	0.3881	1	[OII]-H_α	20.55
9020342	23:18:59.4	+00:35:33.4	0.8124	3	[OII]	23.27
9020406	23:19:06.7	+00:34:54.4	0.8135	2	[OII]	23.48
9020597	23:19:02.2	+00:32:31.5	0.7043	2	[OII]	21.49
9020697	23:19:01.1	+00:31:19.9	1.0789	1	[NeV]-[OII]	22.25
9020867	23:19:02.0	+00:29:18.7	0.8798	2	[OII]	21.73
9020935	23:18:57.5	+00:28:32.0	0.8717	3	[OII]	22.57
9020966	23:19:03.0	+00:28:04.3	0.5833	1	[OII]-[OIII]	22.53
9020977	23:19:03.4	+00:27:54.9	0.1418	1	[OIII]-H_α	21.35
9020980	23:19:02.9	+00:27:46.5	0.9458	2	[OII]	22.90
9020996	23:18:56.8	+00:27:35.5	0.6187	1	[OII]-H_β-[OII]	22.73
9021006	23:19:02.3	+00:27:26.0	0.8048	2	[OII]-[OIII]	22.43
9021088	23:19:04.6	+00:26:27.9	0.6533	3	[OII]	22.33
9021103	23:19:03.1	+00:26:18.8	0.7566	2	[OII]-HeI	23.10
9021378	23:19:27.1	+00:35:50.8	0.5267	1	[OII]	22.77
9021394	23:19:22.0	+00:35:46.2	0.6839	2	[OII]	23.30
9021453	23:19:28.2	+00:35:24.9	0.5396	1	[OII]-[OIII]	23.36
9021495	23:19:17.6	+00:35:12.0	0.6119	1	[OII]-[OIII]	22.96
9021498	23:19:08.6	+00:35:13.0	0.7126	1	[OII]-[OIII]	22.05
9021543	23:19:19.4	+00:34:53.3	0.2790	1	H_β-[OIII]	20.14
9021896	23:19:16.3	+00:32:40.5	0.5863	2	H_δ-G-H_γ	21.34
9021926.1	23:19:11.9	+00:32:31.5	0.5476	3	[OIII]	22.89
9021950	23:19:20.1	+00:32:20.7	0.2772	3	H_β-[OIII]	21.78
9021977	23:19:25.2	+00:32:10.1	0.8640	2	[OIII]	22.81
9022053	23:19:27.0	+00:31:39.7	0.6790	2	[OIII]	19.79
9022064	23:19:15.1	+00:31:40.6	1.0182	1	OIII-[OII]	22.29
9022207	23:19:27.4	+00:30:49.5	1.0223	3	[OII]	22.21
9022259	23:19:20.6	+00:30:34.3	1.1248	3	[OII]	23.42
9022324	23:19:25.7	+00:30:03.1	0.5874	2	H&K-G_{band}	21.45
9022327	23:19:13.2	+00:30:04.4	1.0800	3	[OII]	22.68
9022345	23:19:26.7	+00:29:54.6	1.0716	2	[OII]	23.50
9022367	23:19:13.0	+00:29:46.1	1.0207	2	[OII]	22.84
9022397	23:19:27.2	+00:29:28.0	0.8480	2	H_γ-[OIII]	23.23
9022402	23:19:13.1	+00:29:29.8	0.1879	2	[OIII]	20.79
9022416	23:19:25.8	+00:29:19.7	1.0706	2	[OII]	23.46
9022487	23:19:11.2	+00:28:52.5	0.5485	2	H&K-G_{band}	20.18

Continued on next page ...

Table A.2 - Continued from previous page

Object	RA	DEC	z	Confidence Level	Emission/Absorprion Lines Identified (Å)	R_{mag}
9022527	23:19:13.2	+00:28:39.6	0.4921	2	[OIII]	22.00
9022546	23:19:09.8	+00:28:30.9	0.4467	2	H_β-[OIII]	23.18
9022657	23:19:12.7	+00:27:43.1	1.0306	2	[OII]	22.39
9022685	23:19:08.9	+00:27:35.0	0.7054	1	[OII]-[OIII]	21.55
9022704	23:19:11.9	+00:27:26.2	0.4194	3	H_β-[OII]	22.83
9022776	23:19:24.3	+00:26:54.3	0.8664	2	[OII]	22.49
9022783.1	23:19:10.9	+00:26:54.4	0.7670	1	H_β-[OIII]	22.07
9022783	23:19:10.9	+00:26:54.4	0.5466	1	[OII]-[OIII]	22.07
9022890	23:19:14.4	+00:26:15.2	1.1079	2	[OII]	22.49

Appendix B
Spectra of Cluster Member

Following are the plots of the 1D spectra for the galaxies in the VLT–VIMOS spectroscopic survey identified as being consistent with the supercluster structure at $0.8857 \leq z \leq 0.9239$. Source identification numbers are given in the bottom left–hand corner of each plot along with the calculated redshift of the source.

The bottom x–axis of each plot shows the observed wavelength while the top axis shows the rest frame wavelength at the object's redshift. All fluxes, which are uncalibrated, have been normalized for ease of viewing. Common emission and absorption lines have been overplotted and labeled at the redshift of the object. The hatched areas represent regions in the spectrum where CCD fringing contamination tends to be the most prominent.

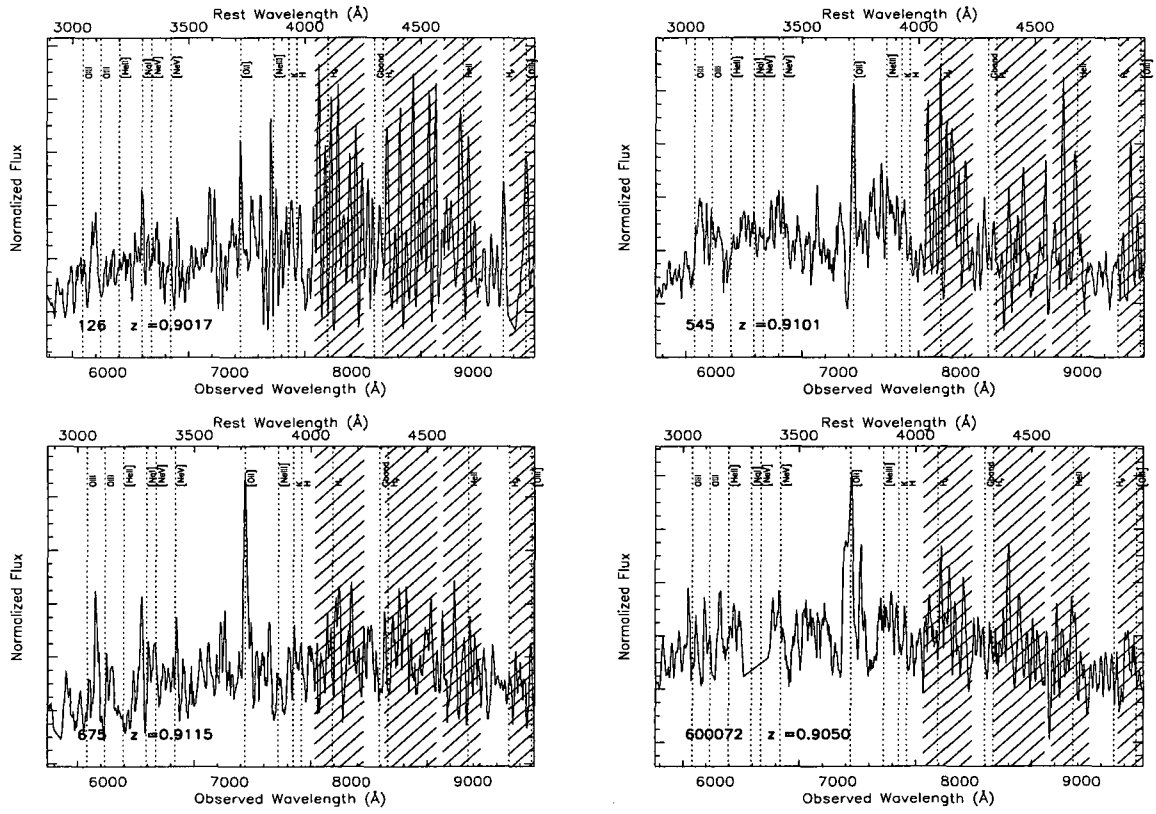

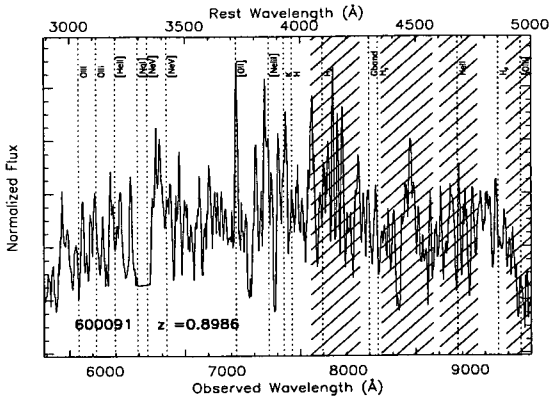
Rest Wavelength (Å)
3000
3500
4000
4500
5000
Normalized Flux
600091 z =0.8986
6000
7000
8000
9000
Observed Wavelength (Å)

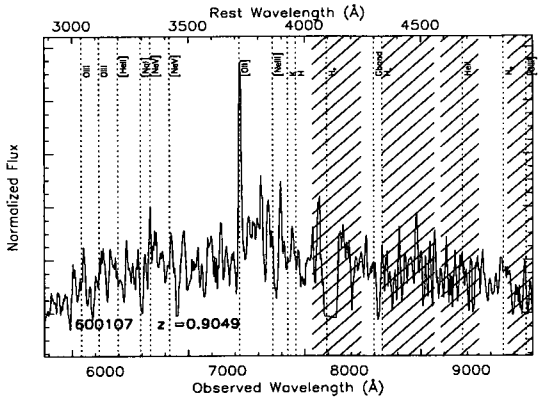
Rest Wavelength (Å)
3000
3500
4000
4500
Normalized Flux
600107 z =0.9049
6000
7000
8000
9000
Observed Wavelength (Å)

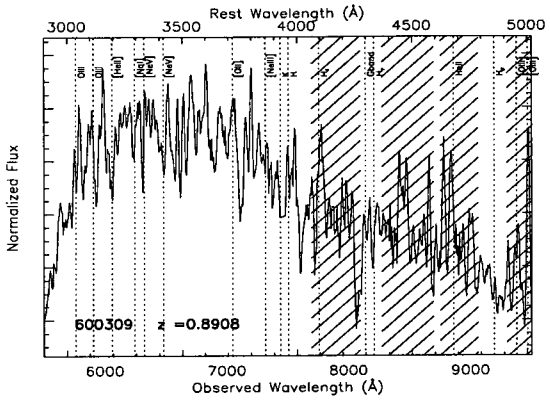
Rest Wavelength (Å)
3000
3500
4000
4500
5000
Normalized Flux
600309 z =0.8908
6000
7000
8000
9000
Observed Wavelength (Å)

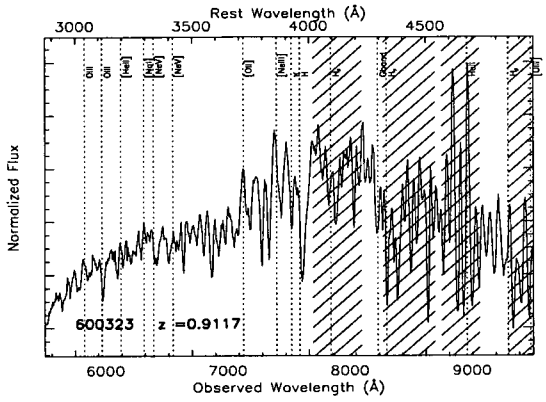
Rest Wavelength (Å)
3000
3500
4000
4500
Normalized Flux
600323 z =0.9117
6000
7000
8000
9000
Observed Wavelength (Å)

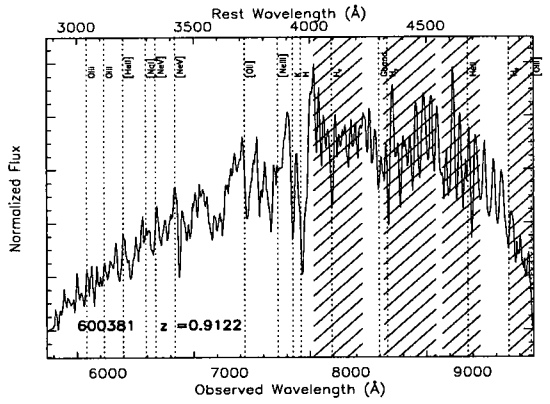
Rest Wavelength (Å)
3000
3500
4000
4500
Normalized Flux
600381 z =0.9122
6000
7000
8000
9000
Observed Wavelength (Å)

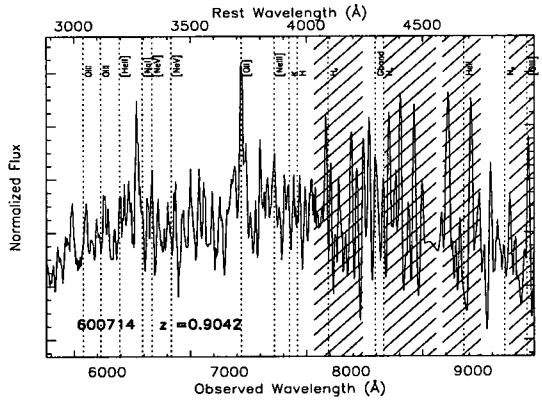
Rest Wavelength (Å)
3000
3500
4000
4500
Normalized Flux
600714 z =0.9042
6000
7000
8000
9000
Observed Wavelength (Å)

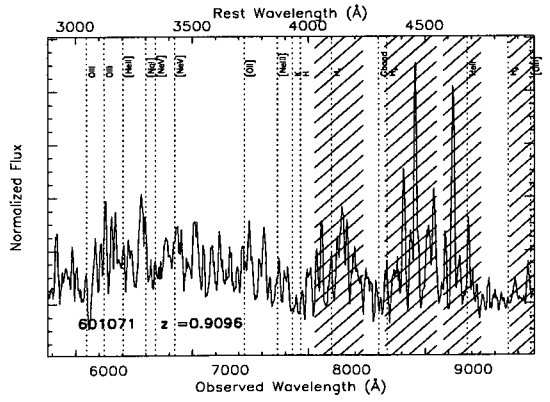
Rest Wavelength (Å)
3000
3500
4000
4500
Normalized Flux
601071 z =0.9096
6000
7000
8000
9000
Observed Wavelength (Å)

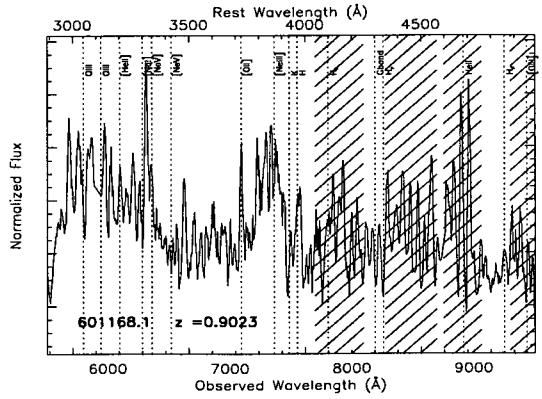
Rest Wavelength (Å)
3000
3500
4000
4500
Normalized Flux
601168.1 z =0.9023
6000
7000
8000
9000
Observed Wavelength (Å)

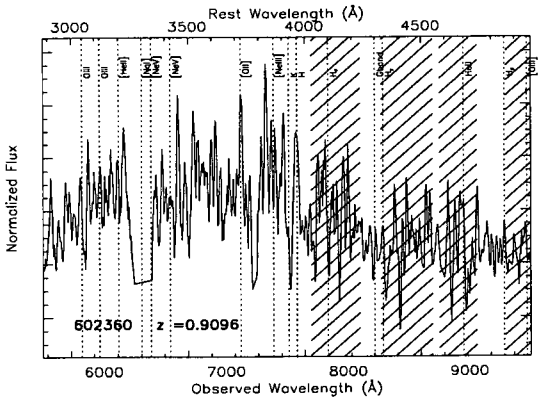
Rest Wavelength (Å)
3000
3500
4000
4500
Normalized Flux
602360 z =0.9096
6000
7000
8000
9000
Observed Wavelength (Å)

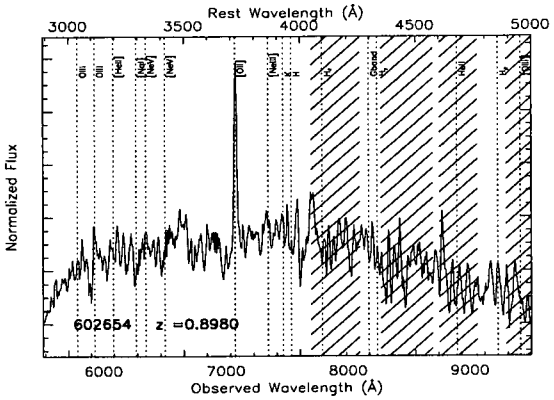
Rest Wavelength (Å)
3000
3500
4000
4500
5000
Normalized Flux
602654 z =0.8980
6000
7000
8000
9000
Observed Wavelength (Å)

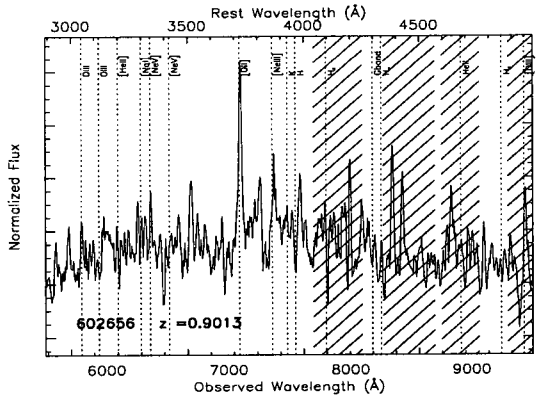
Rest Wavelength (Å)
3000
3500
4000
4500
Normalized Flux
602656 z =0.9013
6000
7000
8000
9000
Observed Wavelength (Å)

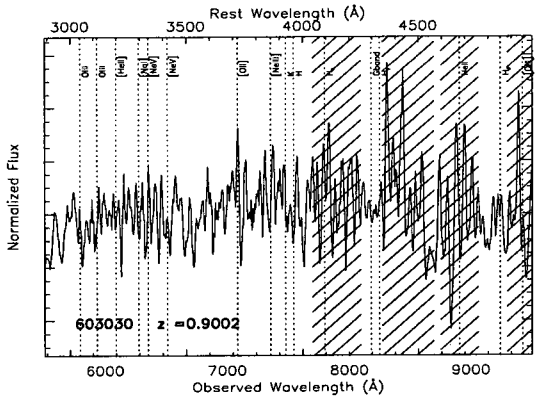
Rest Wavelength (Å)
3000
3500
4000
4500
Normalized Flux
603030 z =0.9002
6000
7000
8000
9000
Observed Wavelength (Å)

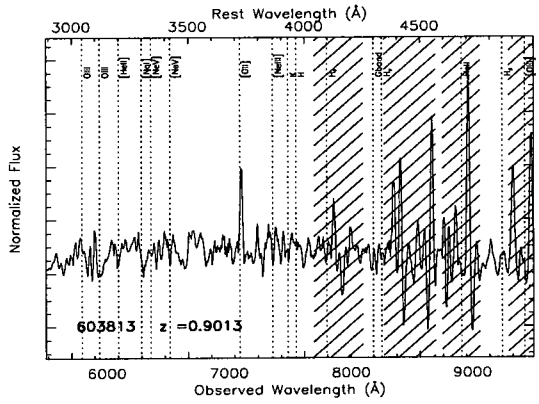
Rest Wavelength (Å)
3000
3500
4000
4500
Normalized Flux
603813 z =0.9013
6000
7000
8000
9000
Observed Wavelength (Å)

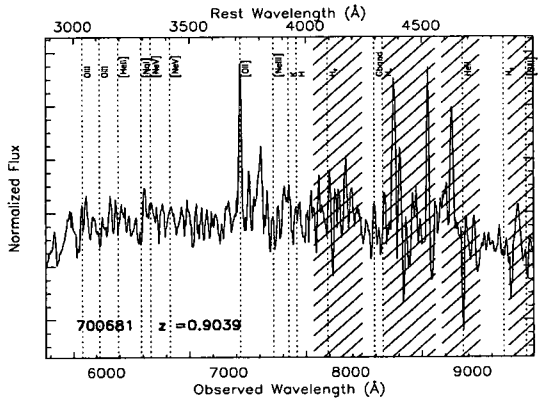
Rest Wavelength (Å)
3000
3500
4000
4500
Normalized Flux
700681 z =0.9039
6000
7000
8000
9000
Observed Wavelength (Å)

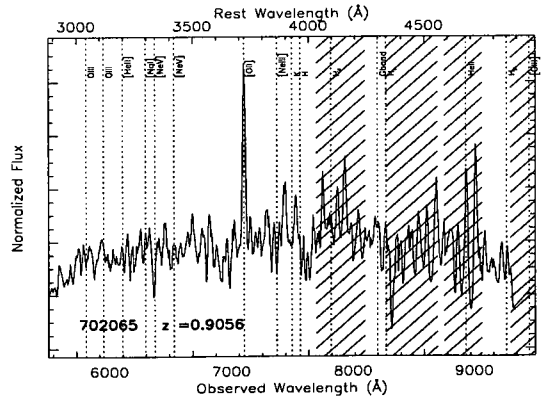
Rest Wavelength (Å)
3000
3500
4000
4500
Normalized Flux
702065 z =0.9056
6000
7000
8000
9000
Observed Wavelength (Å)

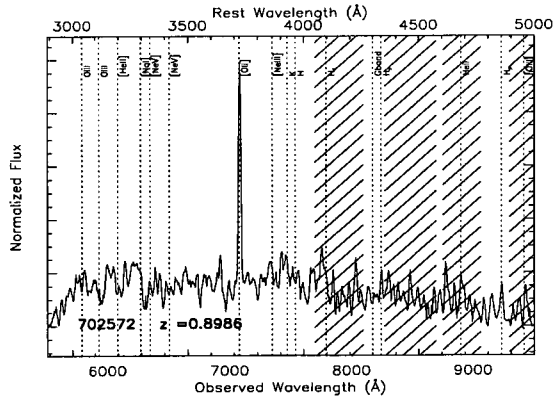
Rest Wavelength (Å)
3000
3500
4000
4500
5000
Normalized Flux
702572 z =0.8986
6000
7000
8000
9000
Observed Wavelength (Å)

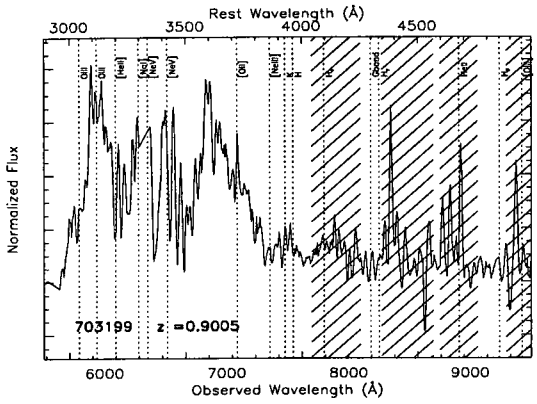
Rest Wavelength (Å)
3000
3500
4000
4500
OII
OII
[HeII]
[NeV]
[NeV]
[OII]
[NeIII]
Hε
Hδ
Hγ
Hβ
[OIII]
Normalized Flux
703199 z =0.9005
6000
7000
8000
9000
Observed Wavelength (Å)

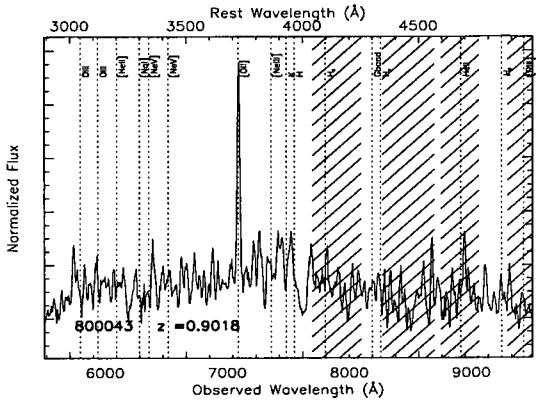
Rest Wavelength (Å)
3000
3500
4000
4500
OII
OII
[HeII]
[NeV]
[NeV]
[OII]
[NeIII]
Hε
Hδ
Hγ
Hβ
[OIII]
Normalized Flux
800043 z =0.9018
6000
7000
8000
9000
Observed Wavelength (Å)

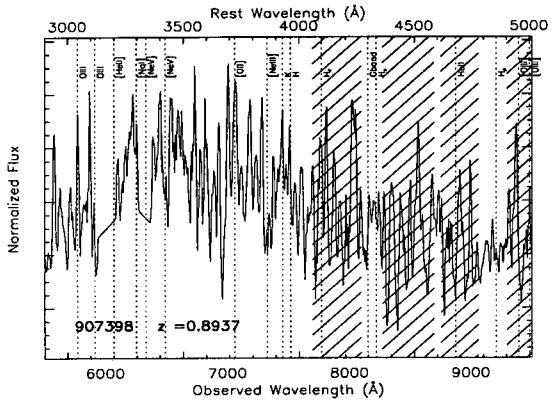
Rest Wavelength (Å)
3000
3500
4000
4500
5000
OII
OII
[HeII]
[NeV]
[NeV]
[OII]
[NeIII]
Hε
Hδ
Hγ
Hβ
[OIII]
Normalized Flux
907398 z =0.8937
6000
7000
8000
9000
Observed Wavelength (Å)

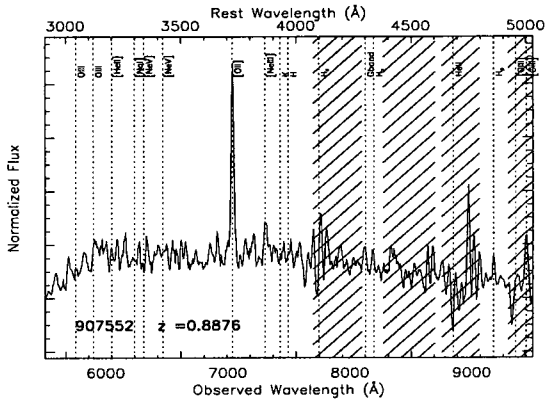
Rest Wavelength (Å)
3000
3500
4000
4500
5000
OII
OII
[HeII]
[NeV]
[NeV]
[OII]
[NeIII]
Hε
Hδ
Hγ
Hβ
[OIII]
Normalized Flux
907552 z =0.8876
6000
7000
8000
9000
Observed Wavelength (Å)

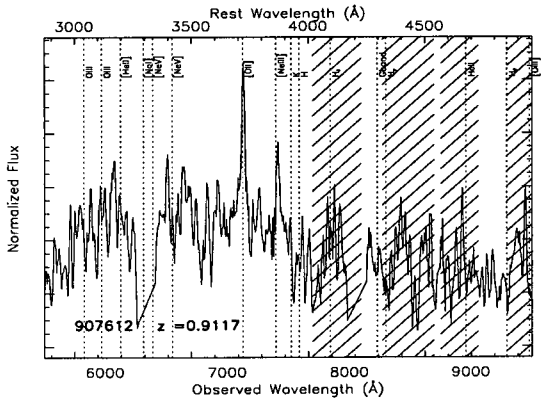
Rest Wavelength (Å)
3000
3500
4000
4500
OII
OII
[HeII]
[NeV]
[NeV]
[OII]
[NeIII]
Hε
Hδ
Hγ
Hβ
[OIII]
Normalized Flux
907612 z =0.9117
6000
7000
8000
9000
Observed Wavelength (Å)

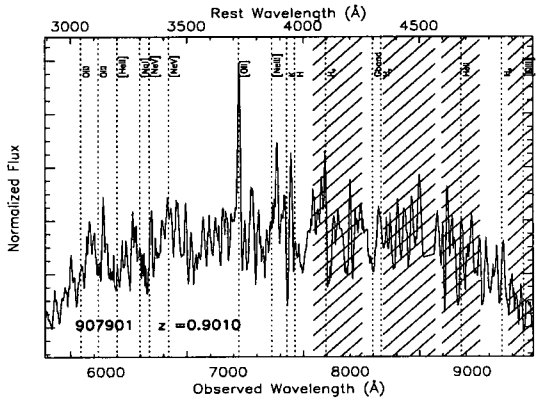
Rest Wavelength (Å)
3000
3500
4000
4500
OII
OII
[HeII]
[NeV]
[NeV]
[OII]
[NeIII]
Hε
Hδ
Hγ
Hβ
[OIII]
Normalized Flux
907901 z =0.9010
6000
7000
8000
9000
Observed Wavelength (Å)

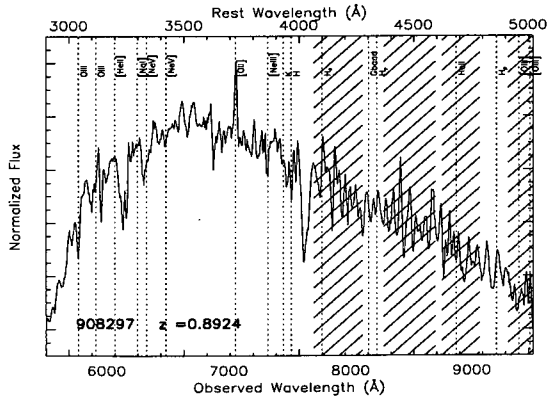
Rest Wavelength (Å)
3000
3500
4000
4500
5000
OII
OII
[HeII]
[NeV]
[NeV]
[OII]
[NeIII]
Hε
Hδ
Hγ
Hβ
[OIII]
Normalized Flux
908297 z =0.8924
6000
7000
8000
9000
Observed Wavelength (Å)

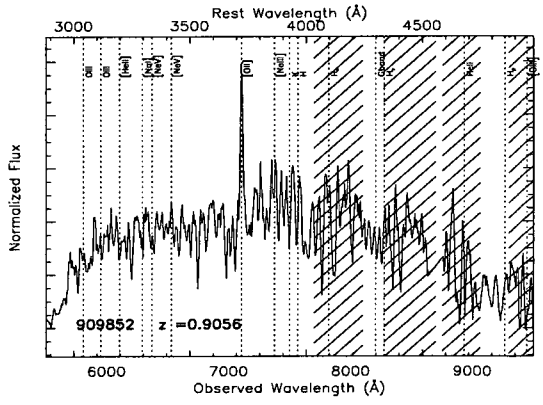
Rest Wavelength (Å)
3000
3500
4000
4500
OII
OII
[HeII]
[NeV]
[NeV]
[OII]
[NeIII]
Hε
Hδ
Hγ
Hβ
[OIII]
Normalized Flux
909852 z =0.9056
6000
7000
8000
9000
Observed Wavelength (Å)

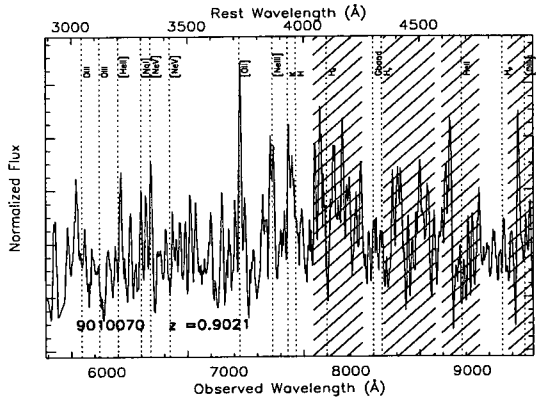
Rest Wavelength (Å)
3000
3500
4000
4500
Normalized Flux
9010070 z =0.9021
6000
7000
8000
9000
Observed Wavelength (Å)

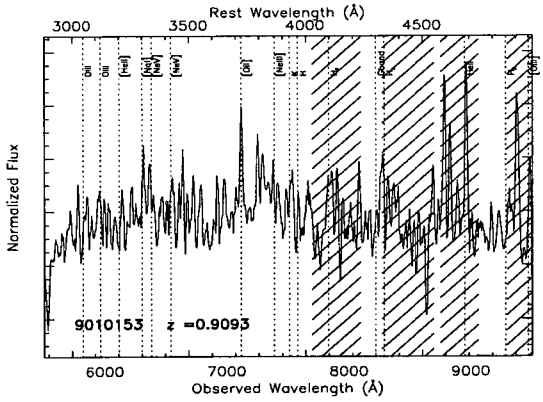
Rest Wavelength (Å)
3000
3500
4000
4500
Normalized Flux
9010153 z =0.9093
6000
7000
8000
9000
Observed Wavelength (Å)

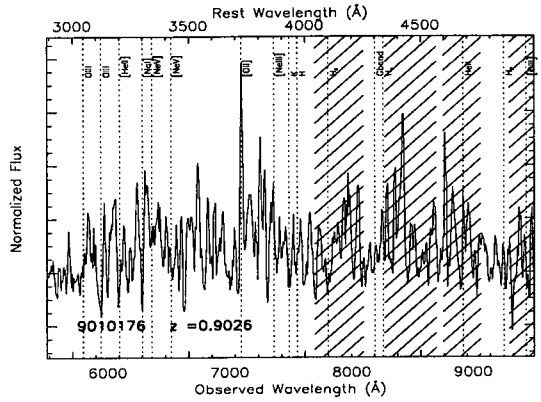
Rest Wavelength (Å)
3000
3500
4000
4500
Normalized Flux
9010176 z =0.9026
6000
7000
8000
9000
Observed Wavelength (Å)

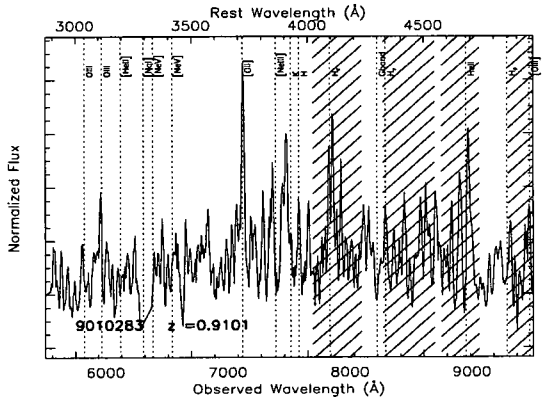
Rest Wavelength (Å)
3000
3500
4000
4500
Normalized Flux
9010283 z =0.9101
6000
7000
8000
9000
Observed Wavelength (Å)

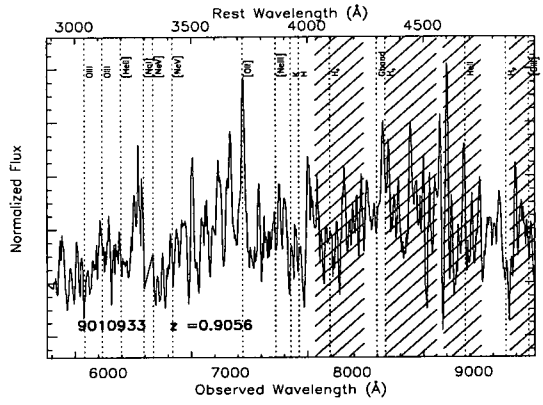
Rest Wavelength (Å)
3000
3500
4000
4500
Normalized Flux
9010933 z =0.9056
6000
7000
8000
9000
Observed Wavelength (Å)

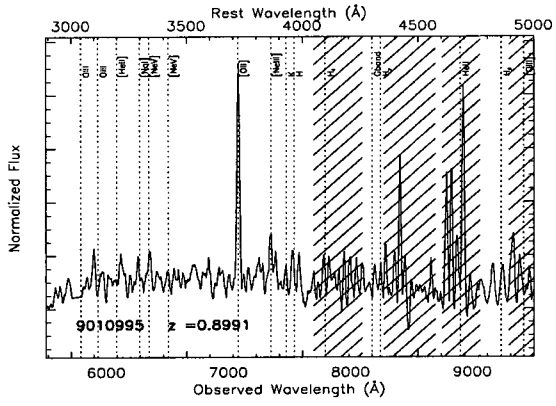
Rest Wavelength (Å)
3000
3500
4000
4500
5000
Normalized Flux
9010995 z =0.8991
6000
7000
8000
9000
Observed Wavelength (Å)

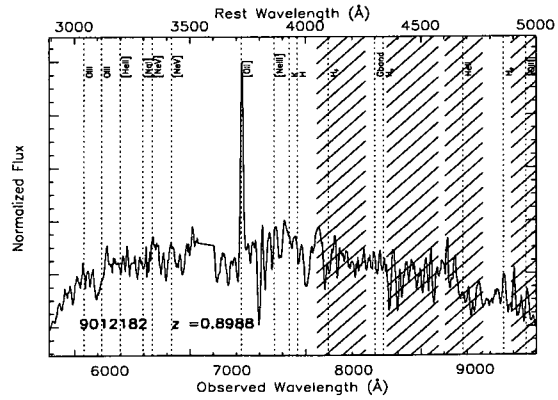
Rest Wavelength (Å)
3000
3500
4000
4500
5000
Normalized Flux
9012182 z =0.8988
6000
7000
8000
9000
Observed Wavelength (Å)

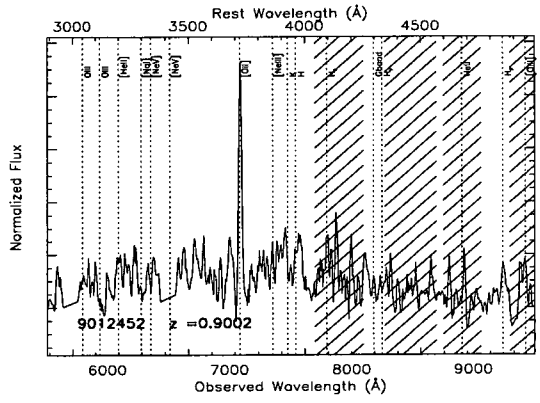
Rest Wavelength (Å)
3000
3500
4000
4500
Normalized Flux
9012452 z =0.9002
6000
7000
8000
9000
Observed Wavelength (Å)

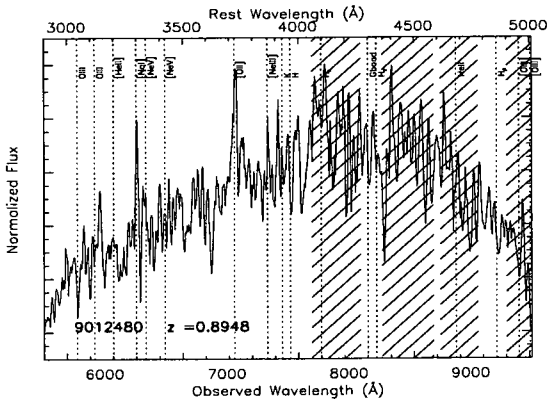
Rest Wavelength (Å)
3000
3500
4000
4500
5000
Normalized Flux
9012480 z =0.8948
6000
7000
8000
9000
Observed Wavelength (Å)

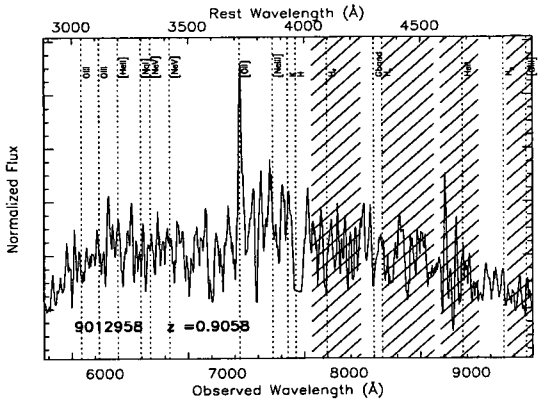
Rest Wavelength (Å)
3000
3500
4000
4500
Normalized Flux
9012958 z =0.9058
6000
7000
8000
9000
Observed Wavelength (Å)

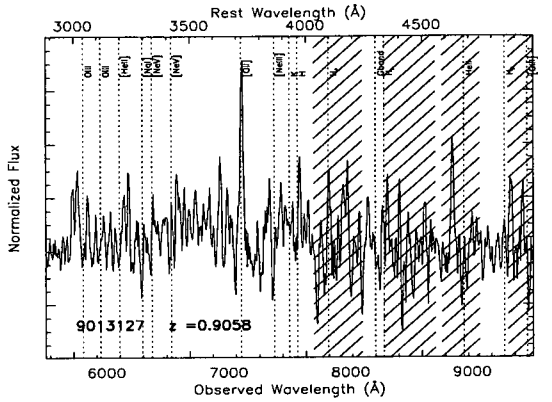
Rest Wavelength (Å)
3000
3500
4000
4500
Normalized Flux
9013127 z =0.9058
6000
7000
8000
9000
Observed Wavelength (Å)

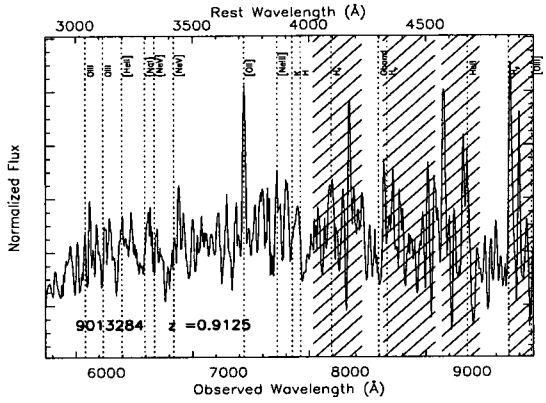
Rest Wavelength (Å)
3000
3500
4000
4500
Normalized Flux
9013284 z =0.9125
6000
7000
8000
9000
Observed Wavelength (Å)

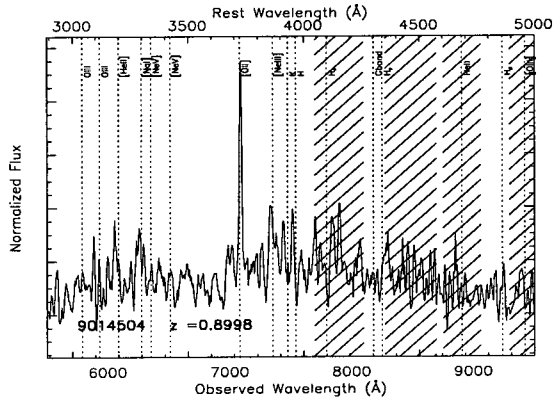
Rest Wavelength (Å)
3000
3500
4000
4500
5000
Normalized Flux
9014504 z =0.8998
6000
7000
8000
9000
Observed Wavelength (Å)

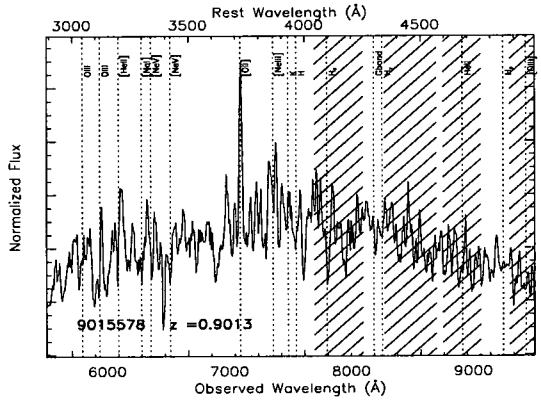
Rest Wavelength (Å)
3000
3500
4000
4500
Normalized Flux
9015578 z =0.9013
6000
7000
8000
9000
Observed Wavelength (Å)

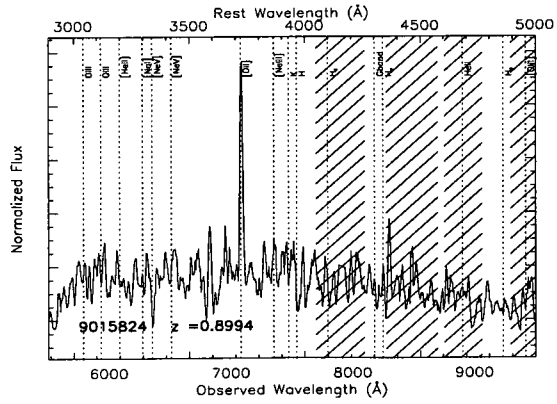
Rest Wavelength (Å)
3000
3500
4000
4500
5000
Normalized Flux
9015824 z =0.8994
6000
7000
8000
9000
Observed Wavelength (Å)

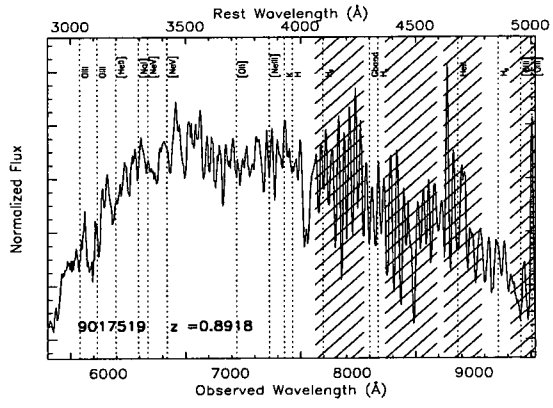
Rest Wavelength (Å)
3000
3500
4000
4500
5000
Normalized Flux
9017519 z =0.8918
6000
7000
8000
9000
Observed Wavelength (Å)

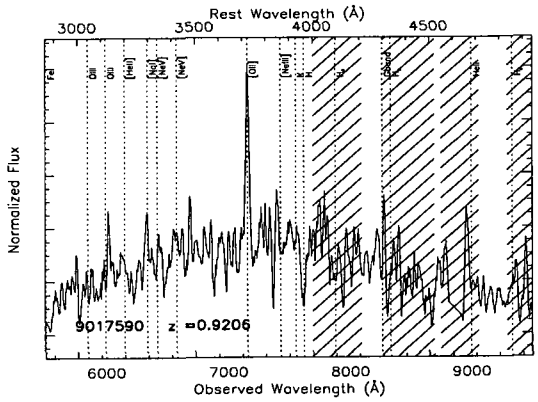
Rest Wavelength (Å)
3000
3500
4000
4500
Normalized Flux
9017590 z =0.9206
6000
7000
8000
9000
Observed Wavelength (Å)

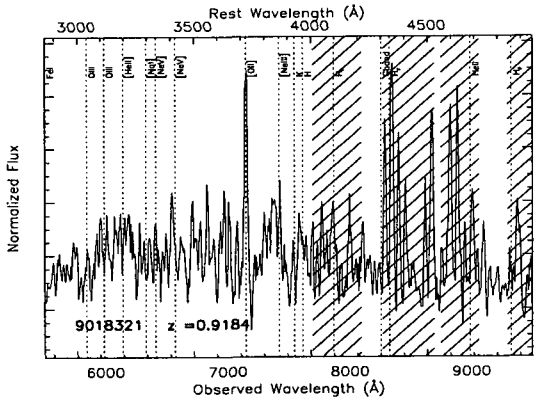
Rest Wavelength (Å)
3000
3500
4000
4500
Normalized Flux
9018321 z =0.9184
6000
7000
8000
9000
Observed Wavelength (Å)

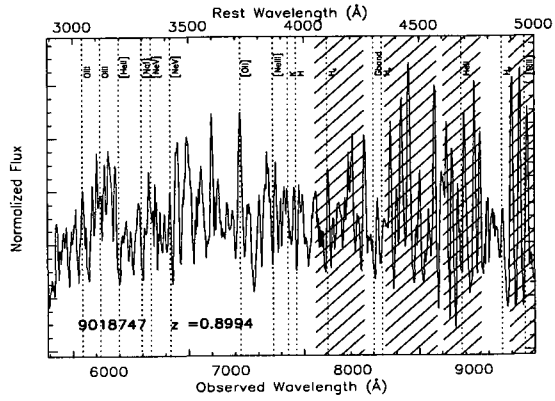
Rest Wavelength (Å)
3000
3500
4000
4500
5000
Normalized Flux
9018747 z =0.8994
6000
7000
8000
9000
Observed Wavelength (Å)

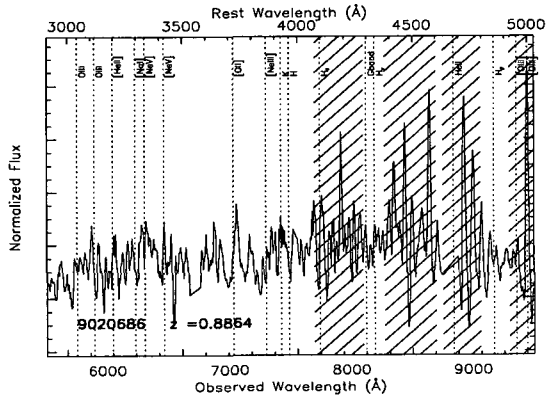
Rest Wavelength (Å)
3000
3500
4000
4500
5000
Normalized Flux
9020686 z =0.8854
6000
7000
8000
9000
Observed Wavelength (Å)

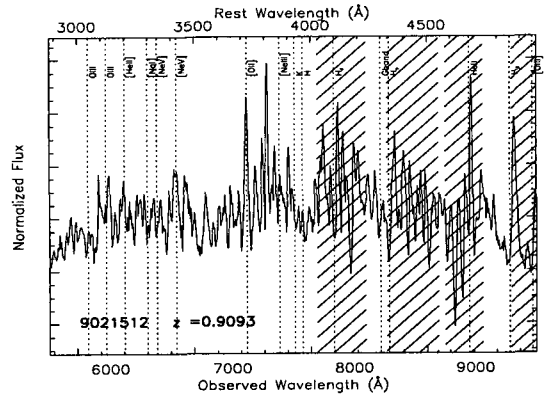
Rest Wavelength (Å)
3000
3500
4000
4500
Normalized Flux
9021512 z =0.9093
6000
7000
8000
9000
Observed Wavelength (Å)

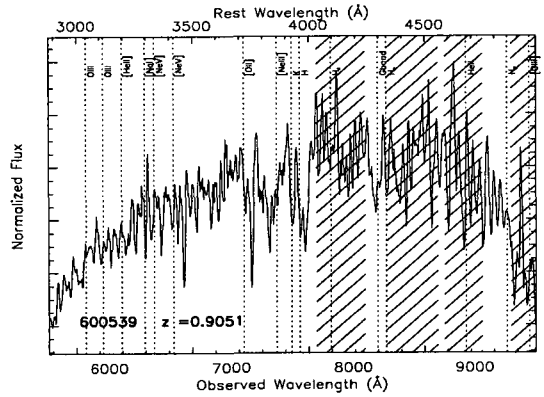
Rest Wavelength (Å)
3000
3500
4000
4500
Normalized Flux
600539 z =0.9051
6000
7000
8000
9000
Observed Wavelength (Å)

Appendix C
Spectra of Radio Galaxies

The following are plots of the 1D spectra for the redshift identified radio galaxies from the VLT–VIMOS spectroscopic survey. The properties of the plots are consistent with those for the cluster members in Appendix B. The only added information on the radio spectra is the addition of an asterisk in front if the identification number of those radio galaxies with redshifts consistent with the RCS2319+00 supercluster.

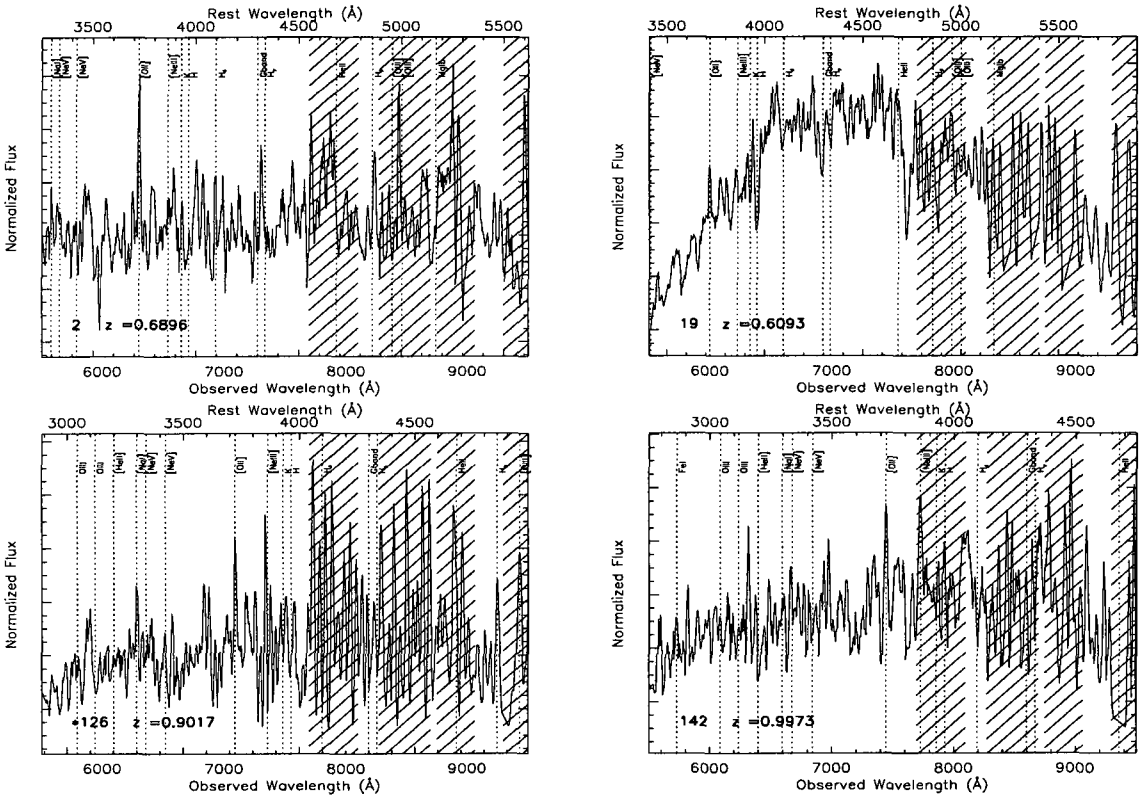

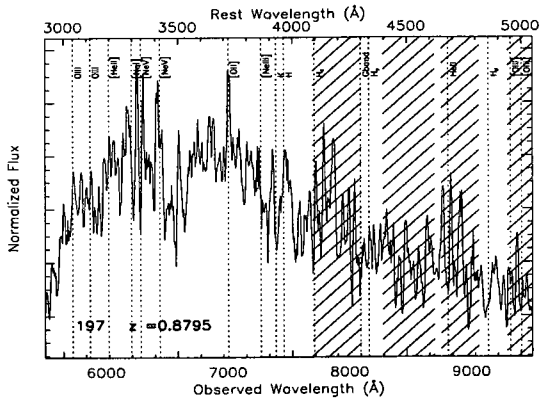
Rest Wavelength (Å)
3000
3500
4000
4500
5000
Normalized Flux
197 z =0.8795
6000
7000
8000
9000
Observed Wavelength (Å)

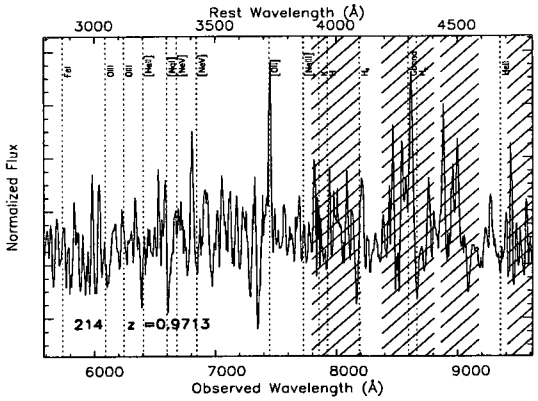
Rest Wavelength (Å)
3000
3500
4000
4500
Normalized Flux
214 z =0.9713
6000
7000
8000
9000
Observed Wavelength (Å)

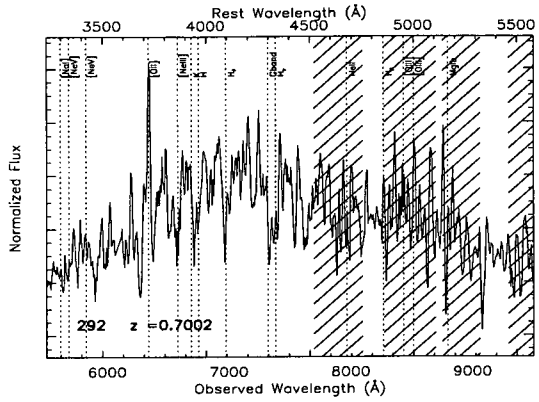
Rest Wavelength (Å)
3500
4000
4500
5000
5500
Normalized Flux
292 z =0.7002
6000
7000
8000
9000
Observed Wavelength (Å)

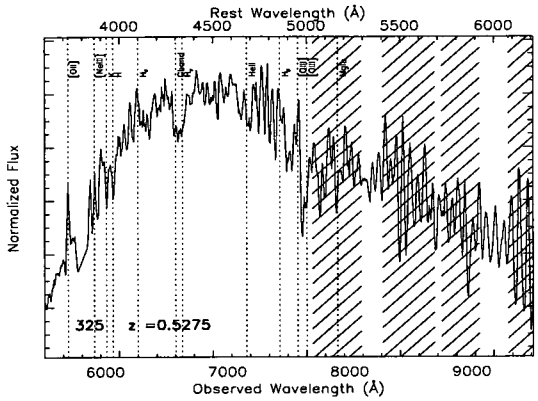
Rest Wavelength (Å)
4000
4500
5000
5500
6000
Normalized Flux
325 z =0.5275
6000
7000
8000
9000
Observed Wavelength (Å)

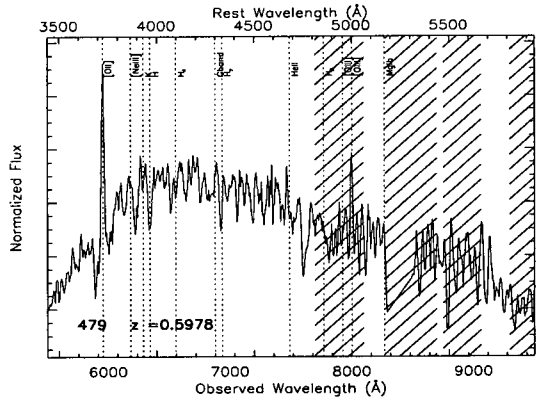
Rest Wavelength (Å)
3500
4000
4500
5000
5500
Normalized Flux
479 z =0.5978
6000
7000
8000
9000
Observed Wavelength (Å)

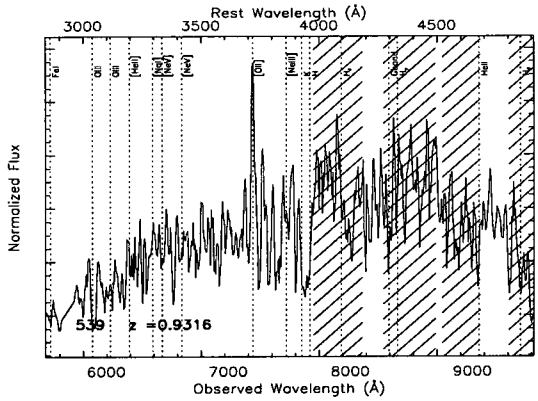
Rest Wavelength (Å)
3000
3500
4000
4500
Normalized Flux
539 z =0.9316
6000
7000
8000
9000
Observed Wavelength (Å)

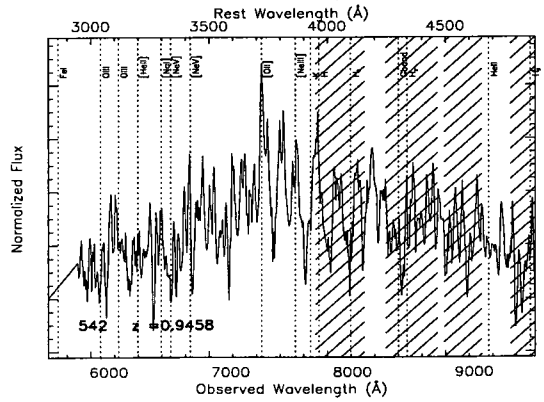
Rest Wavelength (Å)
3000
3500
4000
4500
Normalized Flux
542 z =0.9458
6000
7000
8000
9000
Observed Wavelength (Å)

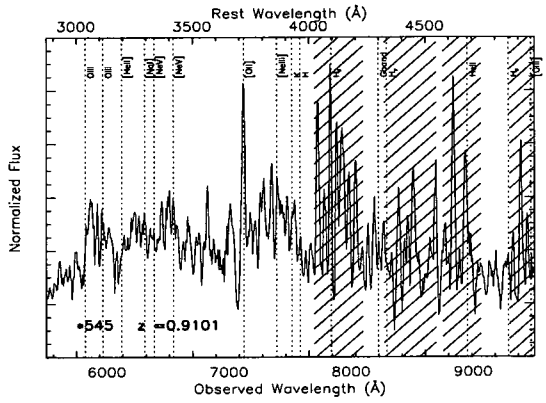
Rest Wavelength (Å)
3000
3500
4000
4500
Normalized Flux
545 z =0.9101
6000
7000
8000
9000
Observed Wavelength (Å)

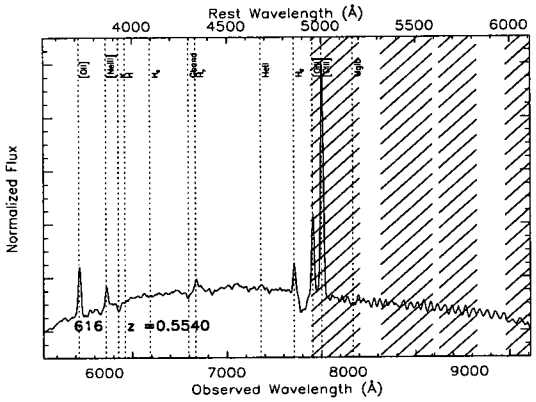
Rest Wavelength (Å)
Normalized Flux
616 z =0.5540
Observed Wavelength (Å)

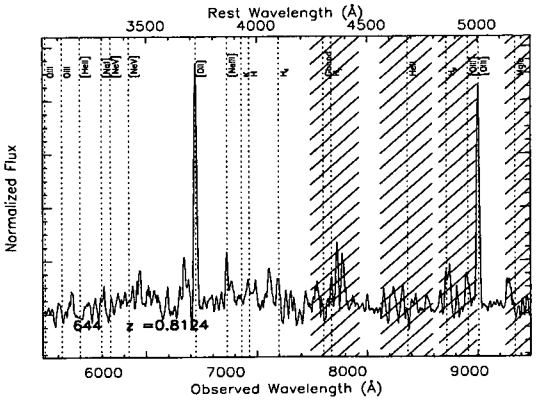
Rest Wavelength (Å)
Normalized Flux
644 z =0.8124
Observed Wavelength (Å)

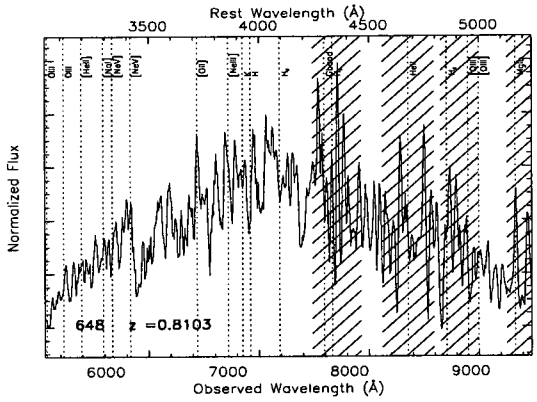
Rest Wavelength (Å)
Normalized Flux
648 z =0.8103
Observed Wavelength (Å)

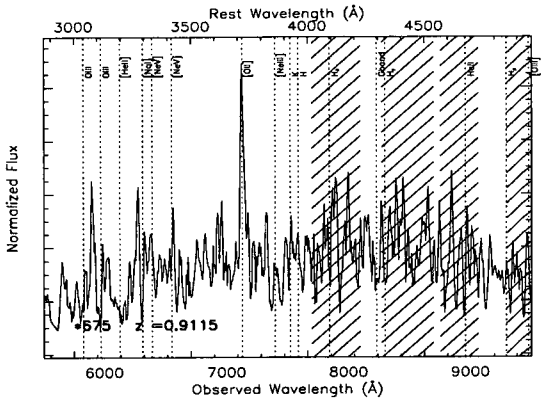
Rest Wavelength (Å)
Normalized Flux
575 z =0.9115
Observed Wavelength (Å)

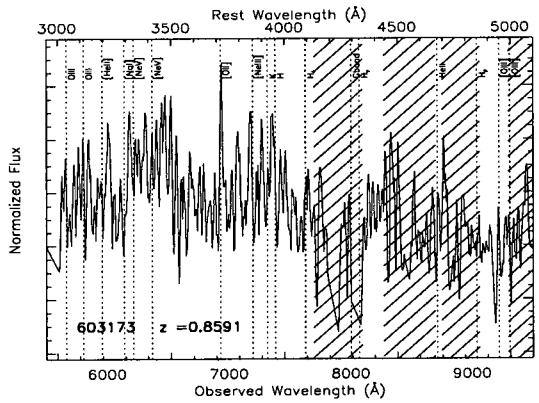
Rest Wavelength (Å)
Normalized Flux
603173 z =0.8591
Observed Wavelength (Å)

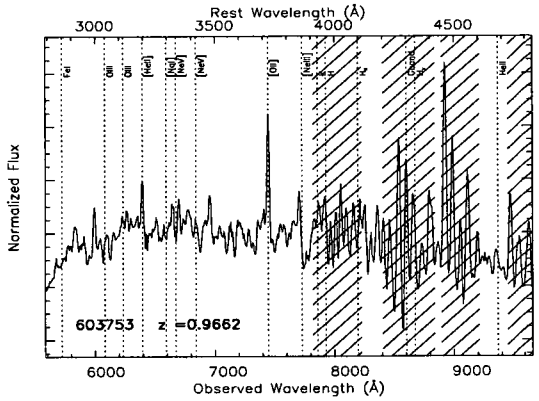
Rest Wavelength (Å)
Normalized Flux
603753 z =0.9662
Observed Wavelength (Å)

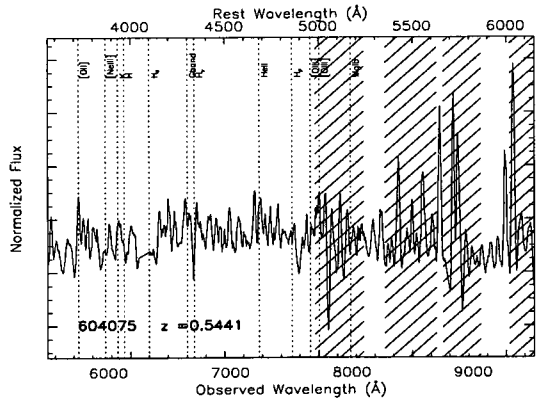
Rest Wavelength (Å)
Normalized Flux
604075 z =0.5441
Observed Wavelength (Å)

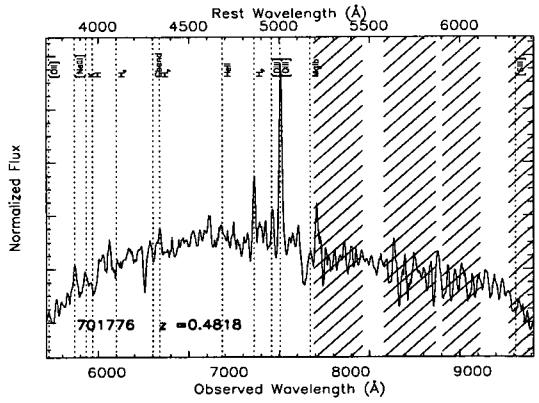
Rest Wavelength (Å)
Normalized Flux
701776 z =0.4818
Observed Wavelength (Å)

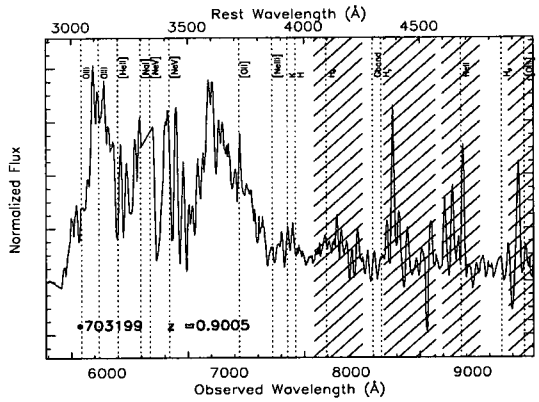
Rest Wavelength (Å)
Normalized Flux
•703199 z =0.9005
Observed Wavelength (Å)

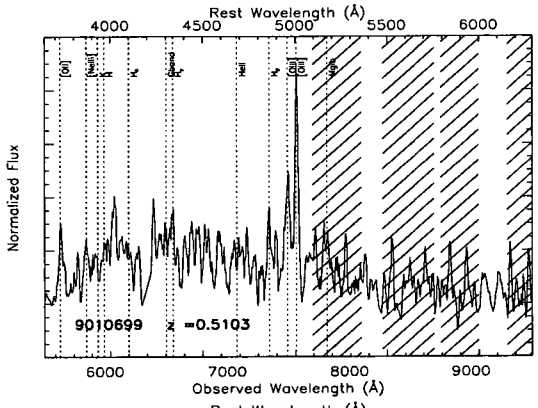
Rest Wavelength (Å)
Normalized Flux
9010699 z =0.5103
Observed Wavelength (Å)

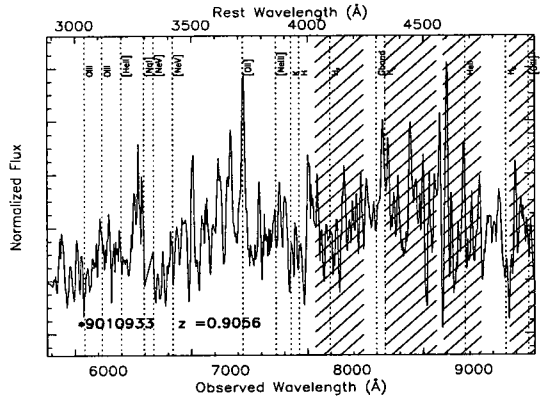
Rest Wavelength (Å)
Normalized Flux
•9010933 z =0.9056
Observed Wavelength (Å)

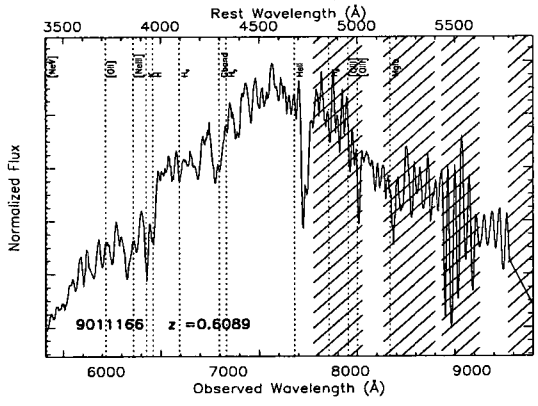
Rest Wavelength (Å)
Normalized Flux
9011166 z =0.6089
Observed Wavelength (Å)

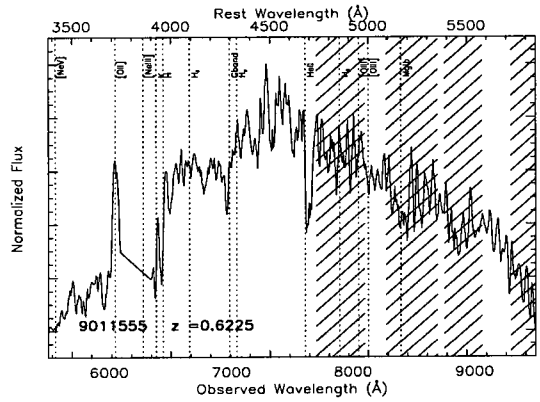
Rest Wavelength (Å)
Normalized Flux
9011555 z =0.6225
Observed Wavelength (Å)

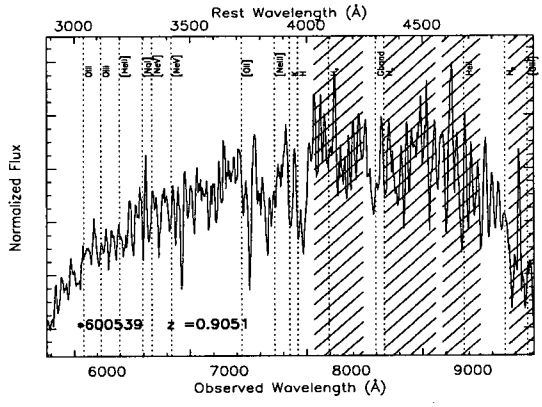
Rest Wavelength (Å)
Normalized Flux
•600539 z =0.9051
Observed Wavelength (Å)

Appendix D

IRAF *apall* Parameters Used in 1D Spectroscopy Reduction

Parameters used in the IRAF *apall* task to reduce the two dimensional spectra to one dimentional spectra.

```
                                I R A F
                     Image Reduction and Analysis Facility
PACKAGE = apextract
TASK = apall

input   =                 p1q1  List of input images
(output =                     ) List of output spectra
(apertur=                     ) Apertures
(format =            multispec) Extracted spectra format
(referen=                     ) List of aperture reference images
(profile=                     ) List of aperture profile images

(interac=                   yes) Run task interactively?
(find   =                    no) Find apertures?
(recente=                    no) Recenter apertures?
(resize =                    no) Resize apertures?
(edit   =                   yes) Edit apertures?
(trace  =                   yes) Trace apertures?
(fittrac=                   yes) Fit the traced points interactively?
(extract=                   yes) Extract spectra?
(extras =                   yes) Extract sky, sigma, etc.?
(review =                   yes) Review extractions?

(line   =                INDEF) Dispersion line
(nsum   =                   50) Number of dispersion lines to sum or median

                                # DEFAULT APERTURE PARAMETERS

(lower  =                  -1.) Lower aperture limit relative to center
(upper  =                   1.) Upper aperture limit relative to center
(apidtab=                     ) Aperture ID table (optional)

                                # DEFAULT BACKGROUND PARAMETERS

(b_funct=             chebyshev) Background function
(b_order=                    2) Background function order
(b_sampl=          -10:-6,6:10) Background sample regions
(b_naver=                    1) Background average or median
(b_niter=                    2) Background rejection iterations
(b_low_r=                   3.) Background lower rejection sigma
(b_high_=                   2.) Background upper rejection sigma
(b_grow =                   1.) Background rejection growing radius
```

```
                                # APERTURE CENTERING PARAMETERS

(width  =                   5.) Profile centering width
(radius =                  10.) Profile centering radius
(thresho=                   0.) Detection threshold for profile centering

                                # AUTOMATIC FINDING AND ORDERING PARAMETERS

nfind   =                     1  Number of apertures to be found automatically
(minsep =                   5.) Minimum separation between spectra
(maxsep =                1000.) Maximum separation between spectra
(order  =          increasing) Order of apertures

                                # RECENTERING PARAMETERS

(aprecen=                     ) Apertures for recentering calculation
(npeaks =                INDEF) Select brightest peaks
(shift  =                  yes) Use average shift instead of recentering?

                                # RESIZING PARAMETERS

(llimit =                INDEF) Lower aperture limit relative to center
(ulimit =                INDEF) Upper aperture limit relative to center
(ylevel =                  0.1) Fraction of peak or intensity for automatic width
(peak   =                  yes) Is ylevel a fraction of the peak?
(bkg    =                  yes) Subtract background in automatic width?
(r_grow =                   0.) Grow limits by this factor
(avglimi=                   no) Average limits over all apertures?

                                # TRACING PARAMETERS

(t_nsum =                   10) Number of dispersion lines to sum
(t_step =                   10) Tracing step
(t_nlost=                    3) Number of consecutive times profile is lost before quitting
(t_funct=            legendre) Trace fitting function
(t_order=                    2) Trace fitting function order
(t_sampl=                    *) Trace sample regions
(t_naver=                    1) Trace average or median
(t_niter=                    2) Trace rejection iterations
(t_low_r=                   3.) Trace lower rejection sigma
(t_high_=                   3.) Trace upper rejection sigma
(t_grow =                   0.) Trace rejection growing radius

                                # EXTRACTION PARAMETERS

(backgro=                  fit) Background to subtract
(skybox =                    1) Box car smoothing length for sky
(weights=             variance) Extraction weights (none|variance)
(pfit   =                fit1d) Profile fitting type (fit1d|fit2d)
(clean  =                  yes) Detect and replace bad pixels?
(saturat=                INDEF) Saturation level
(readnoi=                  3.6) Read out noise sigma (photons)
```

```
(gain    =                 1.96) Photon gain (photons/data number)
(lsigma =                    4.) Lower rejection threshold
(usigma =                    4.) Upper rejection threshold
(nsubaps=                     1) Number of subapertures per aperture
(mode    =                   ql)
```